Abstract

A SOLUTION METHOD DETERMINING THE EFFECT OF SPIN UPON GRAVITATIONAL EFFECTS IN THE SURROUNDINGS OF A BLACK HOLE.

By

Shawn Culbreth

December 2017

Dissertation Director: Orville Day

Using the theory of General Relativity and quasi-normal modes (QNMs) from the Teukolsky equation as a source of quasi-periodic oscillations (QPOs) from black holes provides information about black hole mass and spin. This is related to standing wave resonance phenomena of gravitons and photons trapped in a gravitational potential well surrounding the black hole and provides evidence for the existence of standing wave gravitons in a high gravitational environment, which are observable by the QPO frequencies as infalling electrons interact with these resonance states.

We calculate the QNM angular frequency as a function of spin parameter and create regression equations to relate these frequencies back to spin parameter. The QNM frequencies are what can be experimentally measured, and therefore are preferred as the independent variables. We then compare these equations to QPO data collected from the supermassive black hole Sgr A* and stellar mass black hole GRS1915+105 to calculate the spin parameter for each. The spin parameter of Sgr A* is calculated to be 0.431 ± 0.075 and the spin parameter for GRS1915+105 is calculated to be -0.9875 ± 0.0005. This indicates GRS1915+105 has a retrograde spin.

Due to the precise measurement of the QPOs from GRS1915+105, we are

able to calculate the mass of the black hole to be 10.09 $M_\odot$ using the necessity for consistency of mass and spin between the graviton and photon resonances.

A solution method determining the effect of spin upon gravitational effects in the surroundings of a black hole.

A Dissertation Presented to the Faculty of the Department of Physics

In Partial Fullfillment of the Requirements for the Degree of

Ph.D. in Biomedical Physics

by

Shawn Culbreth

December 2017

A SOLUTION METHOD DETERMINING THE EFFECT OF SPIN UPON GRAVITATIONAL EFFECTS IN THE SURROUNDINGS OF A BLACK HOLE

by

Shawn Culbreth

APPROVED BY:

DIRECTOR OF
DISSERTATION: ____
Orville Day, Ph.D.

COMMITTEE MEMBER: ____
Michael Dingfelder, Ph.D.

COMMITTEE MEMBER: ____
Gregory Lapicki, Ph.D.

COMMITTEE MEMBER: ____
Andrew Sargent, Ph.D.

COMMITTEE MEMBER: ____
Mark Sprague, Ph.D.

CHAIR OF THE DEPARTMENT
OF PHYSICS: ____
Jefferson Shinpaugh, Ph.D.

DEAN OF THE
GRADUATE SCHOOL: ____
Paul J. Gemperline, Ph.D.

ACKNOWLEDGEMENTS

I would like to thank my parents and family for their continued support throughout my academic career.

I would like to thank my advisor, Dr. Orville Day, for working with me and pointing me in the right directions, for being patient with me and working hard to help me understand the equations, concepts, and ideas that led to this work.

I would like to thank Stephanie Winkler, Maneesh Jeyakumar, and Austin Osenga for helping me in the early research stages of this work.

I would like to thank the staff and faculty of the East Carolina University Department of Physics for their help and the use of their facilities.

I would like to thank my committee members for their help and input on this Dissertation.

Contents

List of Tables

List of Figures

1 Introduction

Chi-kwan Chan, from the Harvard-Smithsonian Center for Astrophysics states, "Quasi-periodic oscillations (QPOs) are strong coherent features in the power density spectra that are found in different low mass x-ray binaries. Their frequencies... correspond to accretion flows very close to the central objects. Understanding the origin of QPOs will, therefore, lead to precise measurements of black hole spins as well as direct tests of Einstein's equivalence principle. Although several models have been proposed in the last decade to explain some aspects of the observations, the origin of QPOs is still a matter of debate" [1].

According to Chan, understanding the nature of the QPOs is the gateway to understanding the nature of the black hole spin. The work presented in this dissertation provides a new understanding for the QPOs and provides an explanation for their existence within the observed signal from a black hole. This new model for the QPO shows that they are a consequence of the Quasi-Normal Modes (QNMs) of standing wave graviton and photon resonance states orbiting in the near event horizon region (below the Innermost Stable Circular Orbit, ISCO) as described by the solutions to the Teukolsky equation.

Not only does this method provide a calculation for the spin of a black hole based on these resonance frequencies, it also tests the theory of general relativity (GR) in a near black hole environment and provides observational evidence for the nature and existence of standing wave gravitons, which have yet to be observed in this form. The measurement of a graviton or gravitational wave, is a well sought after experiment which has been gaining popularity and evidence since the two previous proofs of gravitational wave existence, the Hulse and Taylor pulsar binary experiment [2], and the

Laser Interferometer Gravitational-Wave Observatory (LIGO) interferometer experiment which observed gravitational waves from a black hole merger [3] and a neutron star merger. Measuring a graviton standing wave would provide an additional proof of this type of wave and will show they are not limited to traveling waves.

The resonance states of graviton and photon standing waves relate to a well observed phenomenon known as the 3:2 ratio for the x-ray spectrum of stellar mass black hole binaries. The 3:2 ratio phenomenon, up to the work presented in this dissertation, has not been adequately explained by a harmonic interpretation due to the lack of a fundamental frequency observation [4], but the resonance states presented in this work provide an explanation for this phenomenon using the nature of photons and gravitons in the near event horizon environment of a black hole.

The work in this dissertation provides two accurate spin calculations, one for the supermassive black hole Sgr A*, which resides in the center of the Milky Way galaxy, and one for the stellar mass black hole GRS1915+105. Both of these calculations provide results within the limits for previously accepted value of the spin parameters for these black holes. A calculation for the mass of GRS1915+105, based on the method, is also given to be within the expected values for the mass. These two spin measurements show the ability for this method to accurately provide a spin parameter value for both a supermassive black hole and a stellar mass black hole. The mass calculation for GRS1915+105 also provides a possible new calculation method for the mass of a black hole based on the accuracy of the measurements of the QPOs.

2 Background

2.1 Units in General Relativity

General relativistic (GR) equations, especially those pertaining to black holes, are often scaled to be unitless. This is done by setting specific constants, such as the speed of light (c) and the gravitational constant (G), to 1. Converting then from a value in this unitless system to one usable in the real world becomes crucial to understand the significance of that result, but this simplifies the mathematics significantly. Black Holes are often scaled by mass as well. This is viable since black holes only differ by two factors, mass and spin. Outside of mass and spin, all black holes are the same. This means that if the mathematics is scaled by mass and spin, it is universal for all black holes. A simple conversion for time can be seen in equation 1, where $\tau(\mathrm{s})$ is a time in units of seconds and t is unitless. Notice that if G, c, and M are all set to 1, this unitless value represents a time in this unit system.

$$\tau(\mathrm{s}) = t * GM/c^3 \tag{1}$$

Performing a unit analysis on the GM/c^3 term shows that if G is in units of $\frac{\mathrm{Nm}^2}{\mathrm{kg}^2}$, c is in m/s and M is in kg, this creates a unit of seconds, making the unitless t a value in seconds, $\tau(\mathrm{s})$, with this conversion factor. A conversion factor of $\frac{GM}{c^2}$ is used for unitless length. Table 1 shows many of the commonly used unit conversion factors in general relativity.

Table 1: The typical unit conversions for distance (meters), time (seconds), energy (joules), and angular momentum (joule seconds) units to unitless quantities. This is commonly used in GR to represent these quantities as mass scaled pure numbers to apply them to all black holes.

Quantity	SI Unit	Unitless Conversion Factor
Distance	m	$\frac{GM}{c^2}$
Time	s	$\frac{GM}{c^3}$
Angular Momentum	Js	$\frac{GM^2}{c}$
Energy	J	Mc^2
Frequency	Hz	$\frac{c^3}{GM}$

2.2 Black Holes

2.2.1 Collapse Creation Model

Introductory texts to astrophysics, such as *Introduction to Modern Astrophysics* by Carroll and Ostlie [5], explain current black hole creation methods for stellar mass black holes. Stellar mass black holes are created when the largest supergiant stars explode in a supernova. This occurs because the core of the supergiant has depleted its fusable materials and is left with an iron core. Iron is not energy-efficient to fuse or undergo fission and so it does not provide energy to the star in order to continue to create enough radiation to stabilize against gravitational collapse. In smaller, non-supergiant stars, iron is not the final stage and so the resulting explosion is only known as a nova. This is because the star is not massive enough to create enough heat when collapsing to ignite another element's fusion reaction within the star. Figure 1 shows the life of a star, from nebula birth to final remnant left over from this collapse. Note that only the largest of the supergiants are able to become black holes.

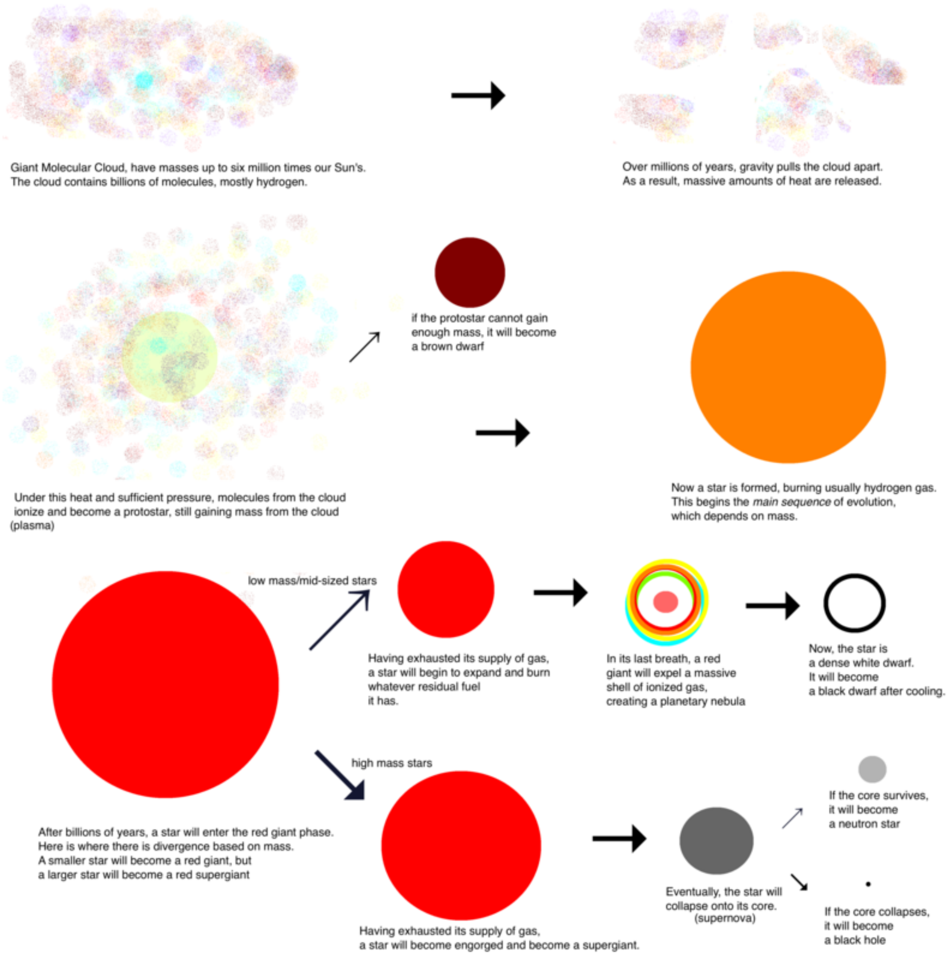

Figure 1: The life cycle and evolution for various sized stars and their progression toward their final remnant. (Image Credit: User:BedrockPerson for Public Domain use in June 2017 for Wikipedia.)

Whether the core is iron or an other element the star is incapable of fusing, the star then begins to collapse without stabilizing and expanding out again. If the star is large enough, the total collapse of the star exerts enough pressure within the star to overcome proton-electron degeneracy, creating a core of neutrons. This is shown in

Figure 2, which shows the differences between the structure of a white dwarf, neutron star, and black hole. Since neutrons are fermions, they follow the Pauli Exclusion Principle and are unable to enter the same state, causing an outward degeneracy pressure which can balance the gravitational pressure from the collapsing remnant, creating a stable neutron sphere. In the case of a neutron star, the outer shell of the star explodes from the stable neutron sphere, leaving the core behind. For a black hole to be created, the pressure inward due to gravity must exceed neutron degeneracy pressure outward, due to the Pauli Exclusion Principle, forcing the neutrons into the same state and smaller volume [5]. This creates a singularity known as a black hole.

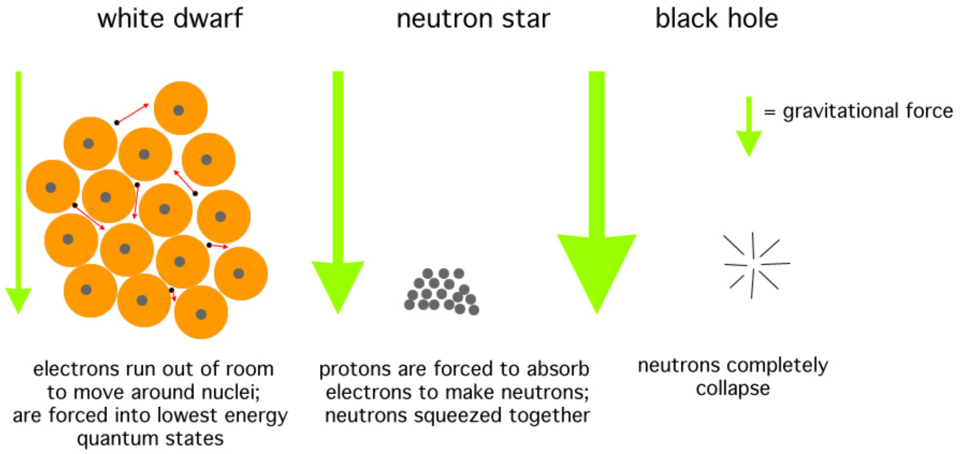

Figure 2: The remnants of a stellar collapse. White dwarfs are created by smaller stars and while the electrons are forced into their lowest state, the pressure is not enough to overcome quantum degeneracy so the atoms remain in tact. Neutron stars are created when electron degeneracy is overcome. Black holes are created when neutron degeneracy is overcome, creating a singularity. (Image taken from http://keywordsuggest.org/gallery/508491.html)

This degeneracy pressure can only be overcome if enough mass is contained within a small volume, defined by the Schwarzschild radius (section 2.2.3) for a non-spinning black hole [5].

2.2.2 Other Methods of Black Hole Creation

A black hole can also be created in a similar manner to the last stages of the collapse creation method, when a neutron star is able to gain enough mass to overcome degeneracy [5]. If the neutron star is able to increase its mass to a critical level, then it will evolve into a black hole. This is usually only seen in neutron star binary systems, where the neutron star is in a binary with a main sequence or giant star. The gravitational pull from the neutron star is large enough to distort the Roche lobe system of the binary and strip mass from the companion star, accreting it onto itself. This increases the overall mass of the neutron star and it is able to collapse farther.

A Roche lobe is a sphere of gravitational influence that has been altered by another body to become a teardrop shape for each body. If a mass extends outside of the Roche lobe, it will transfer to the companion star through a point known as the Lagrangian point in the mass transfer or accretion stream. It is possible, with a large enough companion, for a white dwarf to accrete enough mass to evolve into a neutron star and then eventually, with enough mass, into a black hole using this same process.

It is important to note that the mass transfer stream, and thus the direction of the accreting material is dependent on the rotation of the binary, not on the spin of the individual binary components.

2.2.3 The Schwarzschild Radius

The Schwarzschild radius (r_s) is the radius at which light can no longer escape from a non-spinning black hole, and it defines the size of the black hole for a non-spinning black hole [5]. The entire mass of the black hole must fit within r_s for it to be able to overcome neutron degeneracy when spin is zero. This radius is determined by and directly proportional to the mass. In a unitless mass scaled system r_s is at 2 (the meaning of this can be seen in equation 2).

This is determined by the escape velocity equation, equation 3, with the velocity, v equal to the speed of light c. Solving for the radius then gives equation 2, which is the definition of the Schwarzschild radius [6].

$$r_s = \frac{2GM}{c^2}(\text{in meters}) = 2(\text{unitless}) \tag{2}$$

$$\frac{1}{2}mv^2 = \frac{GMm}{r} \tag{3}$$

Notice that these equations are non-relativistic. This is because the event horizon is defined from the point of view of an outside observer and this Newtonian approach is accurate given the constraint of being in the Schwarzschild metric (section 3) which also indicates a zero spin. The Schwarzschild radius is the definition for the event horizon for a black hole in the Schwarzschild Metric (zero spin), which is explained in section 3, and does not hold true for other metrics.

The Schwarzschild radius provides a simple tool for understanding and calculating the event horizon for a simple non-spinning black hole, since it combines commonly known equations, such as escape velocity, with relativistic ideas in an easy to understand manner. The event horizon placement for a spinning black hole is explained in sections 2.2.6 and 3.3.

2.2.4 Types of Black Holes

Black holes have three basic size categories based on their mass, stellar mass, intermediate mass, and supermassive [5].

The most common black hole is one created by a stellar collapse and is the stellar mass black hole, which has about 3-15 times the mass of the sun, or solar masses ($M_\odot$) [5]. This mass means that the stellar mass black hole had to be formed by a collapsing star significantly larger than the sun. If the remnant is 3-15 times the mass of the sun, the original star must have been more massive than that. In physical size, stellar mass black holes are very small. The Schwarzschild radius for these black holes is only on the order of meters.

Intermediate mass black holes have a mass of about $100 - 10^5$ $M_\odot$ but are debated on whether or not they exist [5]. They are only observed as ultraluminous x-ray sources in the centers of globular clusters and very small galaxies. This is because the most massive stars are around 100 $M_\odot$ and the black holes must be smaller than their parent star due to the collapse and expulsion of an outer envelope. Globular clusters are old stellar groups that exist in the halo of galaxies. Their centers are likely intermediate black holes that have formed from initial stars and over time have built up their mass by absorbing other stars from the cluster.

Supermassive black holes are the largest at 10^5 to 10^9 $M_\odot$ [5]. They usually exist at the centers of large galaxies, such as the Milky Way. Sgr A*, the black hole at the center of the Milky Way Galaxy, has a mass determined to be near 4.0×10^6 M$\odot$. This is discussed further in section 7.1.

Supermassive black holes at the centers of large galaxies are believed to aid in the creation and stability of those galaxies, but little is truly known about their role in this. Quasi-stellar radio sources (QSRs or Quasars) are believed to be actively accreting black holes (they are actively taking in material) that emit massive amounts of radiation during the early stages of galactic formation [5]. This indicates that the supermassive black holes are present and growing during these early stages.

Supermassive black holes can be ejected from their host galaxy or absorbed by another supermassive black hole during galactic mergers [5]. The largest supermassive black holes are often found in the center of large galactic clusters, as those centers are usually where many galactic mergers take place and the black hole is able to grow significantly by consuming other black holes. If a supermassive black hole is ejected, it is no longer visible unless it passes in front of an object. Black holes do not emit light themselves and so the only way to observe one is when it interacts with other material. This can be a gravitational influence, as can be seen by a binary companion being pulled by a black hole, through gravitational lensing, or when it absorbs material. When a spinning black hole absorbs material, some of the nearby charged particles are able to follow magnetic field lines and get ejected from a jet at the magnetic pole of a black hole. This is generally what happens in the case of actively accreting QSRs, which can have jets lightyears (ly) long [5].

2.2.5 How Black Hole Spin is Initiated and Changed

Thinking about a black hole as a singularity, it may be difficult to also think of it as a spinning body, but looking at the collapse creation model, it is reasonable to believe a black hole would spin. The collapse of a star causes the body to spin due to the conservation of angular momentum (equation 4), where I is the rotational inertia and ω is the angular frequency.

$$I_0 \times \omega_0 = I_f \times \omega_f \tag{4}$$

This is exemplified by how a figure skater increases his/her rate of spin by retracting his/her arms. The skater decreases the distance from his/her axis of rotation to a mass in the system (his/her arm) and as that distance decreases, the inertia of the system (I) decreases and the angular frequency (ω) of the system increases to conserve momentum. Similarly an already spinning star that begins to collapse will rapidly increase its spin as infalling material gets closer to the axis of rotation. This leaves a rapidly spinning core once the star has fully collapsed. An infall of material is critical to both black hole creation methods (section 2.2.1 and 2.2.2).

This phenomenon is observed with neutron stars which have a magnetic pole misaligned with their axis of rotation and in the direction of Earth. This particular type of neutron star is called a pulsar. The if the magnetic pole faces the direction of earth, scientists are able to observe x-ray radiation coming from the neutron star. If the pole is not aligned with the axes of rotation, the pulsar spin acts as a lighthouse, where the x-rays are visible at some points in time and not in others. This allows scientists to calculate a rate of spin. Through observation it is determined that pulsars are generally rapidly spinning, which is a consequence of the spin induced by conservation of angular momentum during their formation [5].

If other remnants, such as pulsars, are able to spin rapidly, it makes sense that this same principle can apply to black holes. Black hole spin is rapidly increased during their formation.

Black holes can increase and decrease their spin over time by adhering to the conservation of angular momentum. As material falls into a black hole, that black hole's spin increases similarly to how the spin increased during the collapse of its parent star [5]. This indicates that black holes that are part of a binary system will increase in spin more rapidly than those outside of a binary. Black holes decrease their spin in the same way, by expelling material known through processes named the Penrose Process, Blandford Znajek Process, or Hawking radiation. All are related to quantum effects near the event horizon which can cause the statistically probably emission of particles from the near event horizon region, causing a black hole to lose mass and spin. Over an extremely long period of time, if a black hole does not intake material, it can slow, shrink, and eventually vanish from existence through these processes, which is known as black hole evaporation [5].

2.2.6 Prograde and Retrograde Spin

It is possible for a black hole to have an initial spin from collapsing and then acquire an accretion disk that orbits in the same or opposite directions [5]. When the orbiting material rotates in the same direction as the spin, the black hole has what is called prograde spin. When the black hole is rotating in the opposite direction as the material surrounding it, it has retrograde spin.

When thinking about retrograde spin and the method by which infalling material can change spin, it is logical to think that the spin would slow over time, but with black holes this is not the case. This is due to an effect known as frame-dragging [5]. The black hole pulls the space around it to conform to its motion in an effect called frame-dragging. Infalling material for a retrograde spinning black hole will change the direction of the space around it such that a particle with contrary angular velocity of the spin will turn around and have a complimentary angular velocity to the black hole. Figure 3 shows what happens as a particle falls into a spinning black hole and experiences the effects of frame-dragging.

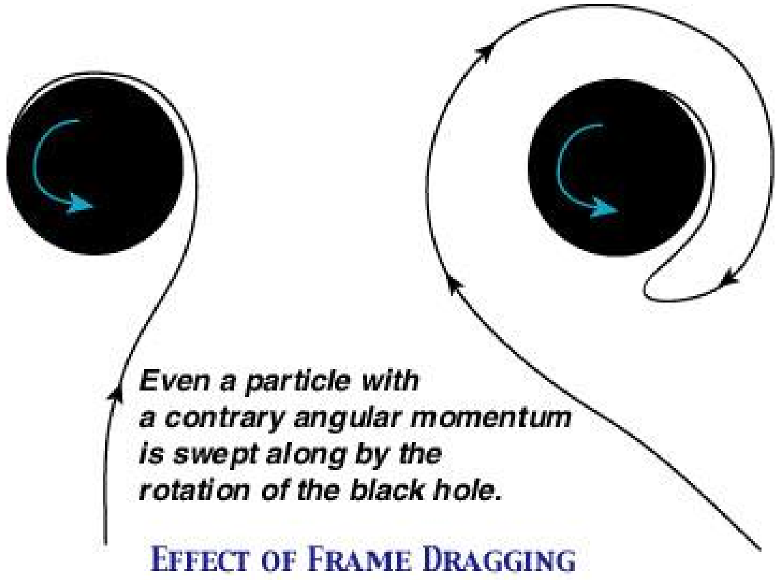

Figure 3: The left image depicts the path of a particle falling into a prograde spinning black hole. The right image shows the path of a particle falling into a retrograde spinning black hole. In both cases, when the particle reaches the black hole it is moving in the same direction as the spin and so will increase the spin of the black hole. (Image credit: Dwight Vincent of University of Winnipeg)

In figure 3, notice how the retrograde case forces material farther outward from the black hole before it spins inward. This changes the geometry of how material can enter the black hole and shifts the event horizon and the Innermost Stable Circular Orbit (ISCO) to a farther location from the center than that of an equal mass non-spinning black hole [5]. Conversely, the frame-dragging from a prograde spinning black hole will add to the motion of the infalling material and shift the event horizon and ISCO closer to the black hole center as compared with an equal mass non-spinning black hole, as seen in figure 4.

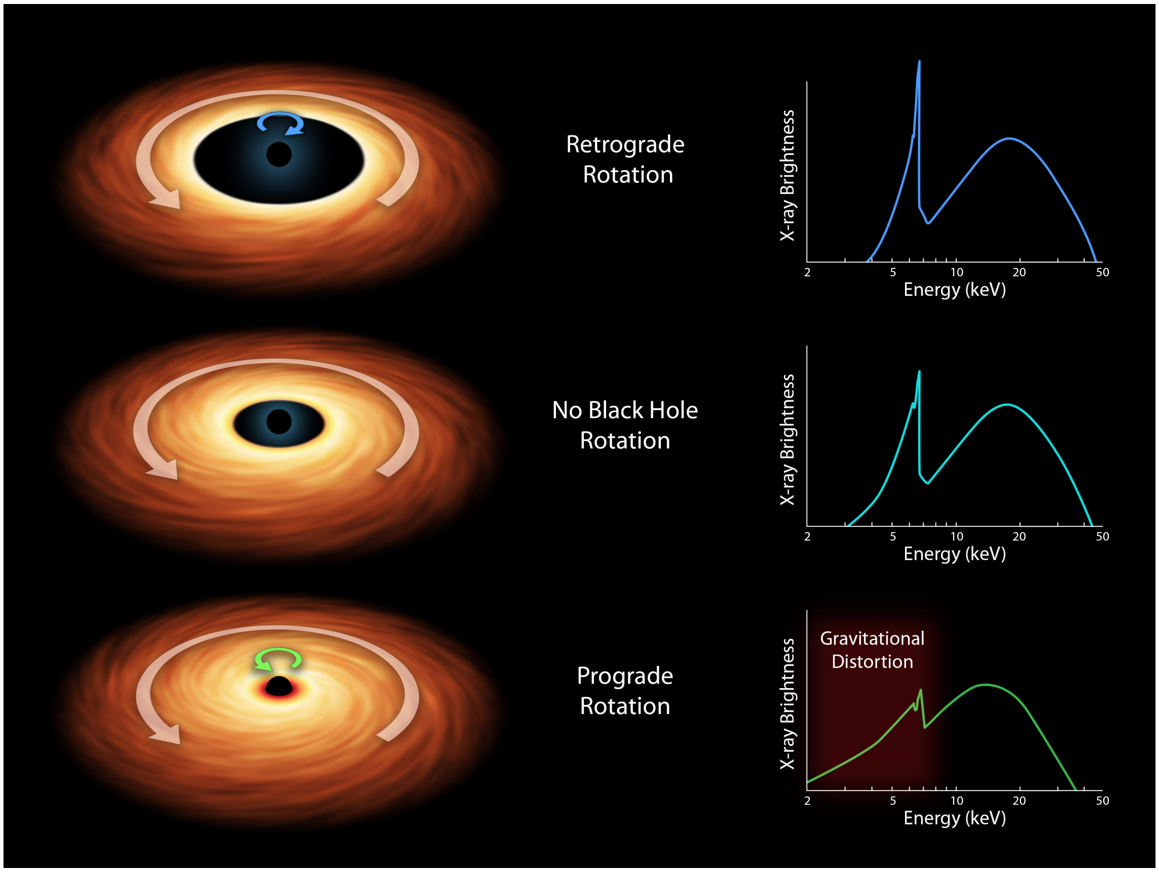

Figure 4: The difference in particle distribution for retrograde, non spinning, and prograde black holes. Retrograde spin causes the ISCO and event horizon to be pushed farther from the center of the black hole compared to a non-spinning case, as shown by the size of the black disk, and prograde spin causes the ISCO and event horizon to be pulled closer. (Image Credit: NASA/JPL-Caltech)

The separation of particles near the black hole is something of importance when determining if a black hole is spinning and by how much in the Teukolsky equation (section 3.3.2). To understand the idea of particle separation, think of a constant number of particles occupying the space, giving a certain density, around the edge of the event horizon. If the event horizon is pushed farther from the center, the surface area of the event horizon is increased, the density decreases, and the separation of particles increases as compared to a non-spinning case. For a prograde spinning black hole, the distance to the event horizon is decreased indicating a higher density and less separation between particles.

2.3 Radiation of Electrons Near a Black Hole

Radiation near a black hole is dependant on the intake of material and distance the material is from the black hole. Once material is close to the black hole, its structure breaks down and it forms an elementary particle plasma. This is due to the gravitational distortion as well as the temperature of the region, which can be near 10^{10} K. The sun, by comparison, is only 2×10^6 K at the corona, making it about ten-thousand times cooler than the near event horizon region [5].

The near event horizon regions are dominated by synchrotron emission, since the magnetic field in this region is exceptionally strong [7], where regions beyond $r = 50$ are dominated by bremsstrahlung cooling. The intake of material is also important in the emission type. Black holes which intake more material will have more compton effects present. The electrons near the event horizon and therefore in the region of interest, emit via synchrotron radiation. Since the emission based on the square of the magnetic field and so as they move closer to the black hole and the magnetic field increases, their synchrotron emission also increases. The effect is enhanced as the electrons move toward the poles in the near event horizon region, since that is where the magnetic field lines are most condensed. This work is not concerned with the bremsstrahlung regions since they are significantly farther from the black hole than the region of interest, but it is important to know how emission changes as observation moves farther from the black hole.

Electrons in the near black hole environment also emit radiation with an intensity that is proportional to the number of electrons squared, rather than the number of electrons. This is known as the emission measure, which is observed with other large radiating bodies, such as the sun [7]. This is a superradiance effect that is based on the overlap of electron radiation, which causes the emission to be influenced by and dependant on a group of electrons rather than a single electron. This happens when the wavelength being emitted is longer than 10^{-4} times the distance between electrons [8]. The radiation emitted from an electron bunch or group is then coherent, in the same phase and direction, since the entire group influences each electron's emission. Naryan and Yi [7] give the frequency ranges at which this coherent radiation occurs in the emission measure. The emission measure dominates in the lower frequency domain since that is where electron spacing becomes comparable to the frequency of emission and creates emission by bunches. The emission increases drastically in the coherent region. This is because the electrons are emitting based on their number squared rather than their number.

2.4 Calculations of Black Hole Mass

2.4.1 Stellar Mass Black Holes

Stellar mass black holes in binary systems can have their mass calculated by comparing them to their companion star, as the mass of any orbital system can be calculated by how the orbits of the two stars are influenced by their companion [5].

In a black hole binary system, the companion star is studied in the same way it would be for the calculation of any binary system. The spectrum of the companion star is compared as it moves around the black hole to show a red shift then blue shift, as shown in figure 5.

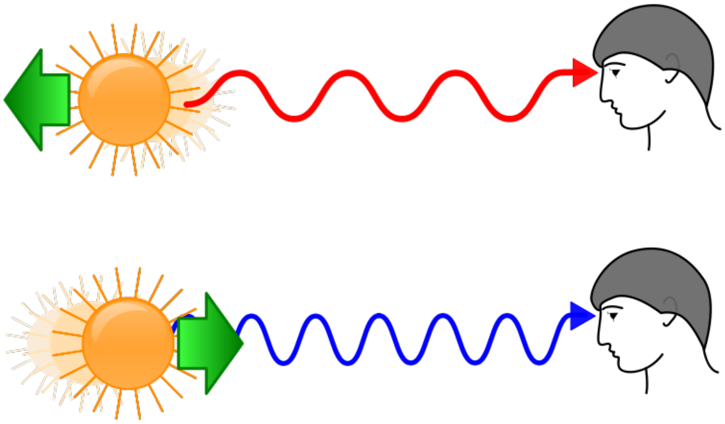

Figure 5: The orbits of binary systems are calculated using the red shift and blue shift of the spectra from the two bodies as they orbit one another. At certain points in the orbit one of the stars will be approaching earth and be blueshifted and the companion will be moving away from earth creating a redshift. The first star will then be redshifted and the second will be blueshifted at another point in the orbit. Comparing the spectrum at these points within the orbit shows the speeds of the orbiting bodies and their periods. (Image Credit: Aleš Tošovskỳ for public domain use)

As the objects orbit one another, the deviation from the expected spectrum frequency value is calculated for varying positions in the orbit. When the black hole is moving away from earth's point of view and the stellar companion is moving toward earth the blueshift of the black hole will be less extreme than the redshift of the companion, as the black hole is typically more massive and will have a smaller orbit than the companion. Focusing on the stellar companion gives the extremes of the shifts and is also likely to have a prominent hydrogen spectrum signal, which is a well known spectrum and can be studied as an expected spectrum for comparison when studying the shifts. A value for the expected spectrum that is higher frequncy than expected for a blueshift, as depicted in figure 5. While the stellar companion moves away from earth's point of view, the frequency is lower than expecteed, as depicted in figure 5. If the stellar companion is moving perpendicular to the earth's direction, the spectrum will give the expected value. This creates a range of spectra for the stellar companion, which can indicate the orbital velocity based on the amount of shift (equation 5) and period based on how long in time these shifts are apart. In equation 5, K represents the directional speed of the star as it approaches or moves away from earth, c is the speed of light, λ is the expected wavelength and $\Delta\lambda$ is the maximum deviation from the expected frequency in red or blue shift.

$$c\frac{\Delta\lambda}{\lambda} = K \tag{5}$$

The K must be related to an incident angle, since this calculation of K assumes a perfectly parallel orbit within the plane of view of earth, which is often not the case. It must also be changed to the angular speed (K_B) of the star to indicate how quickly the star orbits rather than its tangential speed (K). Equation 6 is used in the calculation of this K_B, which is the angular speed when also considering an incident angle. In equation 6, a_B is the semi major axis for the star (this is calculated using $a_A M_A = a_B M_B$), θ_i is the incident angle and T is the period of oscillation of the star. The incident angle can be observed by the alteration of the position of the orbit along the y-axis as the binary rotates. This K_B value is used to calculate the mass function of the black hole, $f(M_A)$, which can be related to the mass as shown in equation 7 if the mass of the companion star is known. Calculations for companion star mass often relate to spectral analysis of the star, which relates to mass and distance of separation via a comparison to known stars by a color luminosity or Hertzsprung-Russell (H-R) diagram. [5]

$$K_B = \frac{2\pi a_B \sin\theta_i}{T} \tag{6}$$

$$f(M_A) \equiv \frac{M_A^3 \sin^3\theta_i}{(M_B + M_A)^2} = \frac{K_B^3 T}{2\pi G} \tag{7}$$

Calculating the mass of a black hole in a binary system is the simplest way to calculate the mass of a black hole and is the primary way of calculating the mass of a black hole. Since it is impossible to see a black hole outside of its gravitational effects, it is impossible to relate a black hole mass in a similar way to the mass of stars on the H-R diagram, though calculating the event horizon radius of a black hole could give an estimate for the mass since all black holes are identical aside from a scaling based on mass and spin, but a way to measure this event horizon would be needed as well as an accurate calculation of the spin. Since the spin is complex to calculate, it is easier to calculate the mass as related to an orbiting object than it is to use the idea that all black holes are identical when scaled as a method for calculating mass.

2.4.2 Supermassive Black Hole Sgr A*

The calculation of the mass Sgr A* is completed using a combination of orbits of nearby stars in a similar manner to how the mass is measured for a stellar mass black hole in a binary system (section 2.4.1), though the difficulty is greatly increased by the amount of orbiting stars and the inability to see exact positions of those orbiting stars [9].

Several groups have been using adaptive optics and other image analysis techniques to find the positions of stars orbiting Sgr A* at the center of the galaxy and the inclination of their orbits and track them over the course of several decades to attempt to map orbital paths and calculate the effect of the central mass on those orbits. [9]

This is a complicated and time consuming method, but several publications explain the modern methods used and give constraints on the mass of the supermassive black hole Sgr A*. Two of the most recent publications from these groups give an explanation of the process of calculating the black hole mass and an estimate of the constraints on the parameters of the orbiting stars.

Bohele et al.[10] and Gillissen et al.[11] give estimates for the mass of $(4.02 \pm 0.16 \pm 0.04) \times 10^6 \mathrm{M}_\odot$ and $(4.28 \pm 0.10 \pm 0.21) \times 10^6 \mathrm{M}_\odot$ respectively. These estimates both exist within a reasonable range for the purposes of this paper, though the estimate by Bohele et al will be used primarily since it is the most constrained value.

2.5 Previous Calculations of Black Hole Spin

2.5.1 Stellar Mass Black Hole Spin

The spin parameter (a^*) is a mass weighted unitless measure of the angular momentum of a black hole. There are several currently standard ways to measure the spin parameter of a stellar mass black hole in a binary, as presented by McClintock et al. [12]. These methods include continuum fitting, high-frequency QPOs, the Iron Potassium (Fe K) line, and polarimetry. McClintock et al. also state that their own method, based upon the radiation of the disk which is included in their work.

The continuum fitting method is limited by its requirements for precise measurements of the black hole mass, inclination angle, and distance, according to McClintock et al. [12] which can all be difficult measurements to measure accurately. This method is therefore relatively uncertain but can provide limits on the spin. This is still considered the best current method by McClintock et al., despite its inaccuracies and measurement difficulties. This is due to an inability for the other methods to provide a meaningful result [12].

The high-frequency QPO method as listed by McClintock et al. is the Abramowicz & Kluźniak hotspot method[13], which is based on high density hotspot measurements as the primary source of the QPOs. This hotspot model has been since discredited as it does not accurately explain the existance of similar QPO measurements across different black holes[4]. The Abramowicz & Kluźniak hotspot model is based on the existence of hotspot regions in the disk region of the black hole, which will be randomly generated and change as the hotspots fall toward the event horizon. This indicates that they should not be consistent across black holes, as the random generation will be different for each black hole. McClintock et al. [12] also mention the inaccuracy of the Abramowicz & Kluźniak hotspot QPO method as it does not put useful constraints on the spin parameter due to its inaccuracy.

The Fe K line method is based on the broadening of iron spectral lines and is powerful in that it does not require a measurement for the mass, though knowledge of the inclination angle decreases the error in the estimate. This model still produces a large amount of uncertainty based upon the placement of the continuum, the model of the flourescing sources, and the ionization state of the disk [12] . This line is also not omnipresent across black holes, making it unable to be used for many black holes.

Polarimetry is a useful method when the polarization features of the black hole disk radiation is visible because it is highly affected by GR effects. This would provide useful information about the spin, but like the Fe K line measurements, these polarization features are not visible in all black holes [12].

The method presented by McClintock et al. [12] gives the spin based on the fitting of the thermal disk without QPO signal. They fitted 22 disk spectra using a thin disk model and obtained a spin parameter based on the luminosity of the disk when compared to the Eddington luminosity. They state that this method assumes a zero torque near the ISCO and an optically thin disk. They give an estimate for the spin parameter of GRS1915+105, one of the more commonly studied stellar mass black holes, to be $|a^*| > 0.98$ given this method [12]. The method appears to only utilize the luminosity of the disk which is shown to be due to a rapidly spinning black hole, but does not specify whether it is prograde or retrograde spin. This is likely due to the non-inclusion of the torque near the ISCO, which will be different in the two cases. This method does show the black hole GRS1915+105 to be spinning near maximum.

2.5.2 Spin of Sgr A*

The main estimates for the spin of Sgr A* come from the analysis of high frequency QPOs as given by the Abramowicz & Kluźniak hotspot model [13]. These models give varying estimates for the black hole spin from 0.65 ± 0.05 (Dokuchaev [14]) to 0.56 (Iwata et al. [15]). This method bears similarity to the Abramowicz & Kluźniak hotspot model for measuring a stellar mass black hole spin and provides the same inherent error due to the lack of understanding about where the QPOs originate and inability to choose correct QPO frequencies.

Kato et al. [16] measured a spin parameter of 0.44 by combining certain high frequency and radio frequency QPOs with disk seismology, and compared it to other observable supermassive black holes. This method puts more constraints on the spin by comparing it to other black holes and gives a lower spin value for Sgr A* than many of the other spin measurements from the hotspot model.

Without fully knowing the cause of the QPO phenomenon around a black hole, it is not possible to validate if the Abramowicz & Kluźniak hotspot model is accurate. This introduces a large issue in the accuracy of the hotspot model, as an improper understanding of the QPOs can drastically change the calculation of the spin.

2.6 Continued Fraction Mathematical Solution Method

The continued fraction solution method is a rapidly converging, series-like method that utilizes a fraction where the denominator contains a number plus or minus the next iteration of the series, as illustrated by equation 8 [17].

$$y = a_0 + \cfrac{a_1}{b_1 + \frac{a_2}{b_2 + \frac{a_3}{b_3 + \dots}}} \tag{8}$$

In a simple continued fraction, the terms a_n are 1. These kind of continued fractions can be used to approximate rational numbers, by dividing and using the remainder to form the next term, such as in equation 9 [17].

$$\frac{45}{16} = 2 + \frac{13}{16} = 2 + \frac{1}{\frac{16}{13}} = 2 + \frac{1}{1 + \frac{3}{13}} = 2 + \frac{1}{1 + \frac{1}{\frac{13}{3}}} = 2 + \frac{1}{1 + \frac{1}{4 + \frac{1}{3}}} \tag{9}$$

General continued fractions have other values of a_n and are used to approximate rational numbers and to solve linear equations [17]. An example of a quadratic equation solution is shown in equation 10.

$$\begin{aligned} Ax^2 + Bx + C &= 0 \\ x(Ax + B) + C &= 0 \\ x &= \frac{-C}{B + Ax} \\ x &= \frac{-C}{B - \frac{AC}{B+Ax}} \\ x &= \frac{-C}{B - \frac{AC}{B - \frac{AC}{B+...}}} \end{aligned} \tag{10}$$

Continued fractions are often written in a linear form. This form is presented for the final solution for the quadratic equation in equation 11 [17]. The linear form implies that the fraction term following the previous term (except the first) is to be inserted after the last mathematical operator symbol (+ or -) in the denomenator of the previous term.

$$x = \frac{-C}{B-}\frac{AC}{B-}\frac{AC}{B-}... \tag{11}$$

This linear form is more convenient due to the complexity given by the continuously small elements. This presents the fraction elements in an easy to see way and gives an understanding of the idea of terms in a continued fraction.

3 The Schwarzschild and Kerr Metrics

3.1 Metrics

A metric is used to describe mathematically the distance between two points, and is commonly used in GR to describe how space time changes that distance [5]. A metric can be represented mathematically as a combination of squares of changes in coordinates, similar to how the Pythagorean theorem, which is effectively a metric in a 2-dimensional cartesian system. The cartesian and spherical coordinate system metrics are given in equations 12 and 13.

$$ds^2 = dx^2 + dy^2 + dz^2 \tag{12}$$

$$ds^2 = dr^2 + r^2 d\theta^2 + \sin^2\theta d\phi^2 \tag{13}$$

These metrics are used to represent a displacement in a geometry and describe how an object moves within that coordinate system [5]. In GR, the constant speed of light adds the ability for time to become a factor in the metric, since when scaled by that speed it becomes a distance measurement. The standard GR metric is shown in equation 14.

$$c^2 d\tau^2 = -c^2 dt^2 + dx^2 + dy^2 + dz^2 \tag{14}$$

This metric can be converted into other coordinate systems, such as spherical coordinates, by changing the standard cartesian coordinates. The major difference in the GR metric is that the ds is replaced by a $cd\tau$, which is the distance related to the proper time (τ) [5]. The proper time is the time experienced in the reference frame of the object, while the time t is the time of an infinitely far stationary clock.

3.2 The Schwarzschild Metric

The Schwarzschild metric is the metric describing the space around a non-spinning, non-charged, spherically symmetric black hole that exists in a vacuum as measured from far away [18]. This is the simplest approximation of an extremely massive object and is used as a simple solution when attempting to calculate phenomena near black holes even though it is not usually the real-world case.

The reduced circumference, a common distance measurement when looking from afar, is given by the circumference divided by 2π. In a standard geometry system, this gives the exact radius, but in the Schewarzschild metric, geometry and distance cannot be measured the same way they are on earth and this definition helps with the understanding of where something is in relation to the black hole [18].

The reduced circumference model must be used since the volume inside a black hole creates a singularity in space-time and so it is impossible to measure a true radius to the center of the space [18]. Think of this like a funnel, as pictured in figure 6. Measuring the radius of a funnel as you move toward the center of the funnel (dr) cannot be done if you are restricted to only touching the surface of the funnel, since you are on an inclined surface and would measure ds rather than dr. The idea that this funnel is a declined ramp means the distance moved will not be equal to the amount of radius changed. Using the reduced circumference, you could measure the circle around your position on the funnel and then calculate how far you are away from the center using the reduced circumference. Figure 6 also shows how space is changed as something moves a distance *ds* toward a Schwarzschild black hole. The flat plane at the top of the figure shows how the space looks to an outside observer. The distance *ds* translates into an observed distance of only *dr*, which is significantly smaller when close to the black hole. The difference in the outer and inner edges of the *dr* ring can be compared to show how far one has moved in the *dr* plane, even though the total movement was *ds*. Reduced circumference gives a frame of reference for distance that is capable of being measured but moving a certain distance closer to the black hole will not reduce the reduced circumference by that same amount in the near black hole environment. This idea is foreign to someone on Earth, where space-time does not bend in such a drastic way.

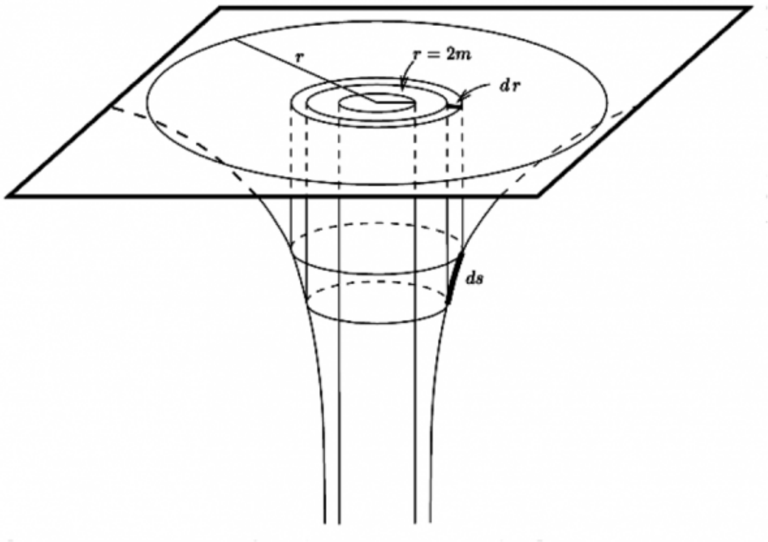

Figure 6: The flat plane where r and *dr* are located is what the radius appears to be to an outside observer, but *ds* is the true distance moved. Notice that *dr* is significantly shorter than *ds*. The reduced circumference of *dr* in this case would give the measurement of r rather than the true distance to the center, which would be infinite since as *dr* moves closer to the black hole, *ds* increases significantly. The circle at $r = 2m$ is the location of the event horizon. Image credit: Dwight Vincent of University of Winnipeg.

This idea of reduced circumference is crucial when trying to measure distances near a black hole and is introduced into the Schwarzschild metric.

This idea of space becoming more warped as one approaches the black hole gives rise to strange effects, such as the idea that an object entering the black hole, as seen from an outside observer, can never truly enter the black hole, the object can only get closer and closer to it [18].

The Schwarzschild metric is represented mathematically by equation 15.

$$c^2 d\tau^2 = \left(1 - \frac{r_s}{r}\right) c^2 dt^2 - \left(1 - \frac{r_s}{r}\right)^{-1} dr^2 - r^2 \left(d\theta^2 + sin^2\theta d\phi^2\right) \tag{15}$$

The Schwarzschild metric is similar to a standard GR metric (equation 14). τ in equation 15 represents the proper time, as it does in the standard GR metric, r, θ, and ϕ are defined the same as the spherical coordinates in a 3 dimensional system, though r is defined as the reduced circumference rather than a true radius, t represents the time as measured from infinitely far away, and r_s is the Schwarzschild radius described in section 2.2.3.

This metric, at $r >> r_s$ does not differ from the standard GR space-time metric in spherical coordinates [18]. While standing on the radius of Earth, which has a Schwarzschild radius of roughly 9mm and a radius of roughly 6370km, the schwarzschild metric does not change how an object moves in any significant way, but near r_s, the correction terms to the standard space-time metric (equation 14) become more significant.

3.3 The Kerr Metric

The Kerr metric is used to describe the space-time surrounding a spinning, non-charged black hole with angular momentum, J, and mass, M [19]. The Kerr metric equations are given as corrections to the Schwarzschild metric and are therefore in terms of the Schwarzschild radius, r_s (equation 2). Typically the Kerr metric is used in spherical coordinates, as shown in equation 16. θ and ϕ are angular coordinates similar to the spherical cooridinate system, r is the reduced circumference, t is the time coordinate, c is the speed of light, τ is the proper time, ρ and Δ are given by equations 17 and 18 respectively and α is a spin term given by equation 19 where J is the angular momentum.

$$\begin{aligned} c^2 d\tau^2 = (1 - \frac{r_s r}{\rho^2}) c^2 dt^2 - \frac{\rho^2}{\Delta} dr^2 - \rho^2 d\theta^2 - (r^2 + \alpha^2 + \frac{r_s r \alpha^2}{\rho^2} \sin^2\theta) \sin^2\theta d\phi^2 \\ + \frac{2 r_s r \alpha \sin^2\theta}{\rho^2} c dt d\phi \end{aligned} \tag{16}$$

$$\rho^2 = \Sigma = r^2 + \alpha^2 \cos^2\theta \tag{17}$$

$$\Delta = r^2 - r_s r + \alpha^2 \tag{18}$$

$$\alpha = \frac{J}{Mc} \tag{19}$$

$$a = \frac{\alpha c^2}{G} = \frac{Jc}{GM} \tag{20}$$

The spin paramter, a, is given by equation 20 and the unitless mass scaled spin parameter, a^* is the spin parameter divided by the mass ($a^* = \frac{a}{M}$). The spin parameter relates to what amount of the mass energy is due to spin [19]. The percentage spin parameter is obtained when $2M$ is set to 1 rather than M. The spin parameter is dependent on the moment of intertia, and therefore the mass distribution of the black hole. Notice that in the standard unitless GR system (section 2.1), $\alpha = a = a^*$. This is not only valid for a black hole, but also for other spinning objects. The Earth, for example, has an a^* of roughly 734 and a sphere of Earth's mass but uniform density has an a^* of 889. The Earth has a lower a^* because the mass is more concentrated at the center than on the outer edge.

A black hole is unique in that the mass is concentrated at the center and so its rotational inertia is brought to an extreme. The absolute value of a^* for a black hole can only range from 0 to 1, which relates to a non-spinning black hole or one spinning such that the event horizon spins at the speed of light [19]. This value range is calculated for the extremes of not spinning to spinning at the speed of light (recall $c = 1$ in this unitless system). It is not uncommon for the system to be altered such that this value instead represents the percentage of the mass energy due to spin, which ranges from 0-0.5. The maximal spin, when $a^* = 1$ in the typical system, relates to the spin contributing 50% of the total mass energy.

In the Kerr metric (equation 16), the $dtd\phi$ term represents a spherical asymmetry and corresponds to a rotation of the angular direction ϕ in time [19]. This, along with the α dependence for various terms, is the major separation from the Schwarzschild metric. Reducing the spin term in equation 16 to 0 gives the Schwarzschild metric (equation 15), as the term containing $dtd\phi$ as well as the correction terms go to zero.

This is an important check as a Kerr black hole without spin is no different from a Schwarzschild black hole.

3.3.1 The Boyer-Lyndquist Formalism

The Boyer-Lindquist formalism is a coordinate system that is used for the metric of a Schwarzschild black hole, that can express the metric of a Kerr black hole [20]. In this system the constants G and c are set to 1 and M, a, and r are set to units of length using the conversions covered in section 2.1. The Kerr metric in the Boyer-Lindquist formalism is given in equation 21, where all terms are the same as those defined for the Kerr metric in 3.3. The Σ term is given to be ρ^2 as shown in equation 17. This equation is set in units of length, and s is a length variable rather than the spin quantum number.

$$\begin{aligned} ds^2 = -\left(1 - \frac{2Mr}{\Sigma}\right) dt^2 - \frac{4Mra\sin^2\theta}{\Sigma} dt d\phi + \frac{\Sigma}{\Delta} dr^2 + \Sigma d\theta^2 \\ + \left(r^2 + a^2 + \frac{2Mra^2\sin^2\theta}{\Sigma}\right)\sin^2\theta d\phi^2 \end{aligned} \tag{21}$$

The Boyer-Lindquist coordinate system is commonly used for equations in the Kerr metric since the Hamiltonian for a test particle in motion in the Boyer-Lindquist system is separable.

3.3.2 The Teukolsky Equation

Saul Teukolsky, in 1972, applied a gravitational perturbation to the Kerr metric in the Boyer-Lindquist coordinate system [21]. This gravitational perturbation is described by the Newman-Penrose quantity and the Weyl tensor. He was able to show that a perturbation of several different fields are detectable by a single master equation, which was named the Teukolsky equation, shown in equation 22.

$$\begin{gathered}\left[\frac{(r^2+a^2)^2}{\Delta} - a^2\sin^2\theta\right]\frac{\delta_s^2\psi}{\delta t^2} + \frac{4Mar}{\Delta}\frac{\delta_s^2\psi}{\delta t\delta\phi} + \left(\frac{a^2}{\Delta} - \frac{1}{\sin\theta}\right)\frac{\delta_s^2\psi}{\delta\phi^2} \\ -\Delta\frac{\delta}{\delta r}\left(\Delta^{s+1}\frac{\delta_s\psi}{\delta r}\right) - \frac{1}{\sin\theta}\frac{\delta}{\delta\theta}\left(\sin\theta\frac{d_s\psi}{\delta\theta}\right) - 2s\left[\frac{a(r-M)}{\Delta} + \frac{i\cos\theta}{\sin^2\theta}\right]\frac{\delta_s\psi}{\delta\phi} \\ -2s\left[\frac{M(r^2-a^2)}{\Delta} - r - ia\cos\theta\right]\frac{\delta_s\psi}{\delta t} + (s^2\cot\theta - s)_s\psi = 4\pi\Sigma T\end{gathered} \tag{22}$$

In the Teukolsky equation, the variable s is different from the one in the Boyer-Lindquist coordinate system, in that instead of representing a length it represents the spin quantum number of the particle ($s = 0$ for a scalar field, $s = \pm 1$ for electromagnetic particles, and $s = \pm 2$ for graviton particles). T represents a source term, which is 0 in a vacuum. ${}_s\psi$ is a wave function given by equation 23 for a particle of spin quantum number s and magnetic quantum number m in a vacuum [21].

$${}_s\psi(t, r, \theta, \phi) = e^{-i\omega t}e^{im\phi}S(\theta)R(r) \tag{23}$$

Detailed explanations for the solutions and solution methods to the Teukolsky are presented in section 6.

3.4 Differences Between Schwarzschild and Kerr Black Holes

Introducing a spin term into the Schwarzschild metric changes the near event horizon significantly due to the introduction of frame dragging as discussed in section

2.2.6 and seen in figure 3. The changing of space time changes the shortest distance between points such that infalling material, including photons, spins in the direction of the black hole [6]. This effect significantly alters the way the movement of a particle in the Schwarzschild metric versus the Kerr metric.

The introduction of spin also alters the potential energy of the region surrounding the black hole. Potential energy cuves will be discussed in detail in section 4.1 for Schwarzschild black holes and section 5 for Kerr black holes, but it is important to understand that the potential energy curves of a Kerr black hole are different from those of a Schwarzschild black hole. Prograde spin will cause the material to orbit closer to the black hole and retrograde spin will cause material to orbit farther from the black hole when compared to the Schwarzschild case, as seen in figure 4 in section 2.2.6. This also changes the event horizon, pulling it closer toward the black hole for prograde spin and farther from the black hole for retrograde spin. The effect on the event horizon effectively changes the physical size of the black hole.

Mathematically, the Kerr metric is significantly more complex than the Schwarzschild metric and is not spherically symmetric. This means that solution methods for the Schwarzschild metric that reduce the equation due to symmetry will not be valid in the Kerr metric [19].

4 Theory and Previous Work

4.1 Resonance Cavities Surrounding a Schwarzschild Black Hole

In the Schwarzschild metric, the idea of reduced circumference (section 3.2) changes how an outside observer has to look at material falling into a black hole. Since moving closer to the black hole reduces the reduced circumference to that black hole by a smaller amount per unit length traveled as a particle moves toward the black hole, the particle is never able to reach the black hole as seen from an outside observer. This creates an effective potential energy barrier, meaning that the potential energy of the system behaves as normal (decreases as a body moves closer) for a gravitational body only to a certain point before encountering the barrier [22]. The change from decreasing to increasing for a particle must mean there is a point at which there is a potential well for that particle near the black hole.

Equation 24 shows the square of the effective gravitational potential of the region near a Schwarzschild black hole for a massless particle with angular momentum quantum number L and spin quantum number s [23].

$$V_{L,s}^2 = \left(1 - \frac{2}{r}\right)\left(\frac{L(L+1)}{r^2} + \frac{2(1-s^2)}{r^3}\right) \tag{24}$$

This equation is represented graphically for both $s = 1$ and $s = 2$ particles with $L = 1$ and $L = 2$ respectively in figure 7. The potential squared curve looks like a potential hump, or scattering potential but since this is a square equation, a scattering potential is not the only solution possible [22].

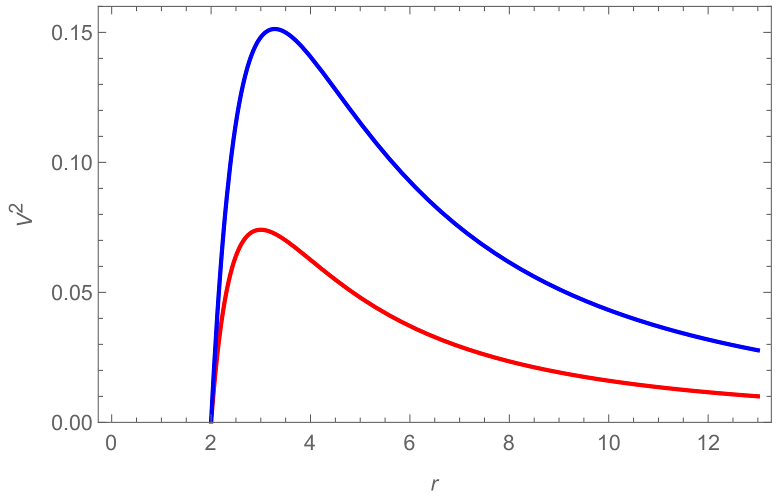

Figure 7: Potential energy squared of a Schwarzschild black hole for graviton particles (blue) of L=2 and photons (red) at L=1. r is in the standard GR unitless system, and the event horizon is therefore at $r = 2$. [22]

There are two possibilities for the solution for the potential given this potential squared equation. These solutions are given in equation 25 [6]. The first solution is a positive root equation which leads to a potential hump, or scattering potential. This scattering potential is often used to calculate the frequency of massless particles which are expelled from the near black hole region, as they have come into the region of this potential and have been forced back out due to the potential barrier created. The second is a negative root equation, which creates a potential well. The potential well, with $V = -\sqrt{V^2}$, creates a region surrounding the black hole in which an oscillation can occur for massless particles [22].

$$V_{L,s} = \pm\sqrt{1-\frac{2}{r}}\sqrt{\frac{L(L+1)}{r^2}+\frac{2(1-s^2)}{r^3}} \tag{25}$$

The negative root equation is shown graphically in figure 8 compared to a classical gravitational potential energy for a particle of the same angular momentum but non-zero rest mass (equation 26).

$$V = -\frac{1}{r} + \frac{L^2}{2r^2} \tag{26}$$

The event horizon is at r=2 and so, it can be seen that in a classical approach, the gravitational potential is not constrained by this event horizon as it is in the GR approach. The rest masses of photons and gravitons are zero, meaning the classical gravitational potentials are not able to accurately describe their energy curves.

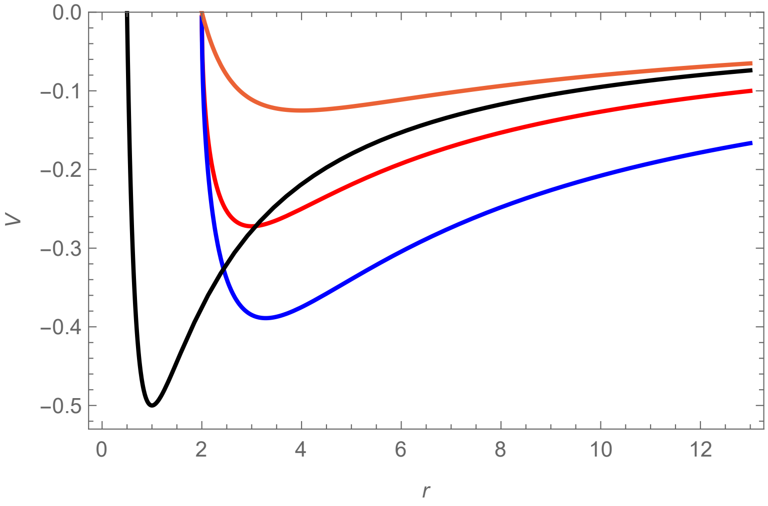

Figure 8: Potential energy wells of photons and gravitons around a Schwarzschild black hole. r is in the standard GR unitless system, and the event horizon is therefore at $r = 2$. The black and orange curves show a classical curve for a particle of non-zero rest mass and non-zero angular momentum shown in equation 26 for $L = 1$ and $L = 2$ particles respectively. The red and blue curves are potential wells based on the negative root of the potential squared equation, shown in equation 25 for $s = 1$, $L = 1$ and $s = 2$, $L = 2$ particles respectively. [22]

The red and blue curves in figure 8 show the curves of interest for photons and gravitons near a black hole. The potential well created by using the negative root creates a possible resonance cavity at the bottom of the well, at $r = 3.000$ for photons of L=1 and $r = 3.281$ for gravitons of L=2.

The Innermost Stable Circular Orbit (ISCO) for a Schwarzschild black hole is located at $r = 6$ which means that these resonance cavities exist closer to the black hole than the last allowed stable circular orbit (the orbit of smallest r, where material circles the black hole without falling into it) [22]. These cavities are not expected to contain stable orbits, but rather to be what is known as a "leaky cavity," which has an imaginary component to the frequency of particles within the cavity relating to a half-life [22]. This half-life means these particles will eventually leave the cavity and either fall toward the black hole or fall out of the orbit and escape. Since the cavity will lose particles, in order to continue influencing the region around the black hole, the cavity must be repopulated.

Kaniadakis and Quarati [24] explain the inclusion principle, a net attractive force between large groups of bosons and individual bosons that causes the individual of proper frequency to change phase and direction to match the group. This inclusion principle is one way the photons and gravitons in the resonance cavities are able to repopulate the cavity in coherent oscillation.

4.1.1 The Tortoise Coordinate System

The tortoise coordinate system [25], which shifts the event horizon to negative infinity using equation 27, gives a way to approximate the cavity as a perturbation from a harmonic oscillator, a commonly studied equation for a cavity [23]. In this equation, r^* is the new coordinate, r is the original coordinate, and C is a shifting constant that allows the equation to be centered to any numerical or graphical location. In this case, the prefered center is for the minimum of the cavity to be at

$r^* = 0$. This numerical value is different for each cavity, but they are both set such that the center of the cavity is at 0.

$$r^* = r + 2\ln\left(\frac{r}{2} - 1\right) + C \tag{27}$$

The tortoise coordinate system is so named for the story of Achilles and the tortoise, where a tortoise agrees to race Achilles so long as it gets a head start. The explanation of why Achilles could not win was that he would have to first traverse the distance the tortoise traveled, but while he did so the tortoise would continue moving. The distance the tortoise moved then would have to also be traversed by Achilles, but again the tortoise would have moved farther during this time. This pattern continues until the tortoise crosses the finish line and so Achilles is never able to fully make up the distance to the tortoise [26]. This relates to the tortoise convincing Achilles he will never be able to reach the tortoise and therefore in a mathematical framework the system creates a value that can never be reached. The tortoise coordinate system is used to shift a point to negative infinity such that numbers in the system can approach that point, but never truly reach it. The point $r = 2$ in equation 27 is chosen as the point shifted to infinity, as that is the location of the event horizon.

In order to use a tortoise coordinate system, the r in the original equation must be replaced with the solution for r in the new coordinate system, given by equation 28 [22]. In this equation, the ProductLog function is required and is the solution to $y = x + \ln(x)$, which cannot be solved analytically. This means the tortoise coordinates must be solved and input numerically.

$$r = 2(1 + \mathrm{ProductLog}(\sqrt{e^{-2-C+r^*}})) \tag{28}$$

Substituting equation 28 into the negative potential equation, equation 25 gives equation 29, which is the potential energy in the tortoise coordinate system.

$$V_{L,s}(r^*) = -\sqrt{1 - \frac{1}{1+\text{ProductLog}(\sqrt{e^{-2-C+r^*}})}} \tag{29}$$
$$\times\sqrt{\frac{L(L+1)}{(2(1+\text{ProductLog}(\sqrt{e^{-2-C+r^*}})))^2} + \frac{(1-s^2)}{4(1+\text{ProductLog}(\sqrt{e^{-2-C+r^*}}))^3}}$$

This new tortoise coordinate system gives a graphical representation shown in figure 9 for graviton particles of $L = 2$, $L = 3$, and $L = 4$. Despite the $L = 4$ state being the deepest well, this is not the preferred state, as the $L = 2$ state has the lowest imaginary part for the wave function, which indicates the longest lifetime (half-life is inversely proportional to the imaginary component) [22]. This means the $L = 2$ state will be the most populated.

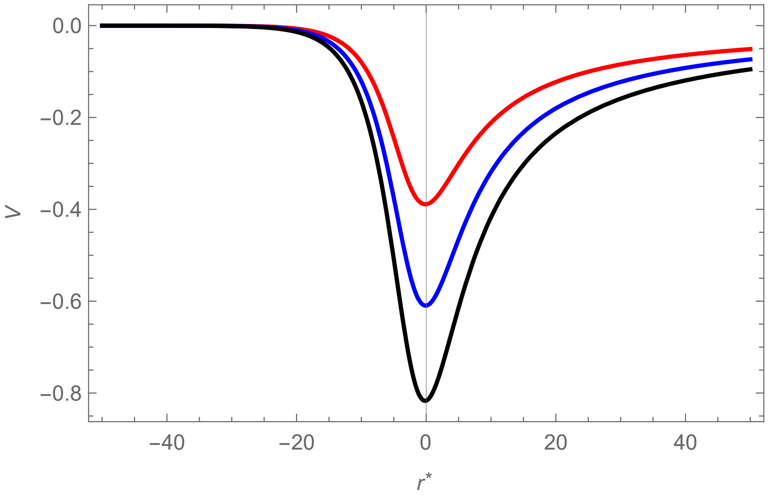

Figure 9: The potential energy curve for gravitons of $L = 2$ (red), $L = 3$ (blue) and $L = 4$ (black) in the tortoise coordinate system. The center of the potential well is placed at $r^* = 0$ and the singularity is pushed to $r^* = -\infty$. This coordinate system creates a graph similar to that of a harmonic oscillator near $r^* = 0$ [22].

4.1.2 Harmonic Oscillator Approximation and Perturbation Theory

Comparing the tortoise coordinate system potential to a harmonic oscillator can be accomplished by finding an equation for a harmonic oscillator (equation 30) where k is defined to have a similar curvature to the potential near $r^* = 0$ [22]. This k value is calculated using the second derivative of r^* since that relates to curvature, as seen in equation 31.

$$V = \frac{1}{2}k(r^*)^2 \tag{30}$$

$$\ddot{r}^*|_{r^*=0} = k \tag{31}$$

This calculation allows for the construction of a wave function based on the calculated k value for this oscillator (equation 32).

$$\psi = \frac{(\frac{k}{2})^{1/4}}{\sqrt{\pi}} \times e^{-(\frac{k}{2})^{1/2}(r^*)^2} \tag{32}$$

To compare the harmonic oscillator with the tortoise coordinate potential, the region containing the largest area of the wave function but be near equal [22]. This region is shown in figure 10, and is defined as the area under the red curve. Notice in this region, the blue and black curves are near equivalent. The difference between these two equations in the region of interest, defined by the wave equation are shown in figure 11, where the wave equaiton is again in red.

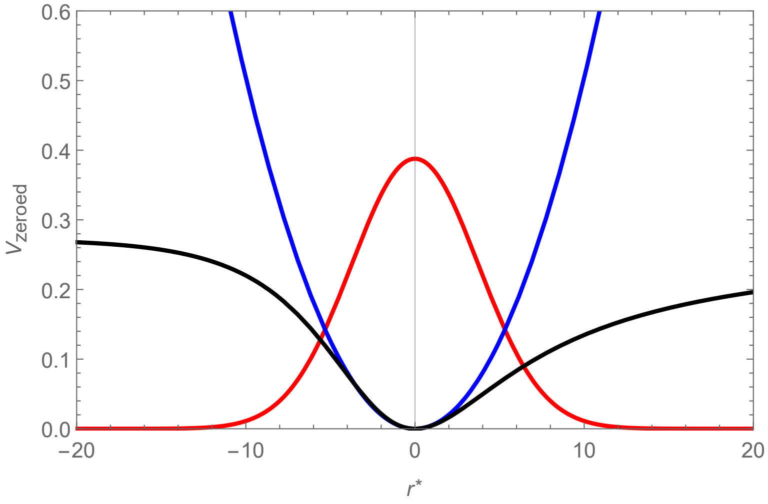

Figure 10: The harmonic oscillator function generated by equations 30 and 31 is shown in blue and is compared to the L=1 state photon potential energy in black. The red curve shows the wave function, which has highest probability near $r^* = 0$ and defines the region of interest. [22]

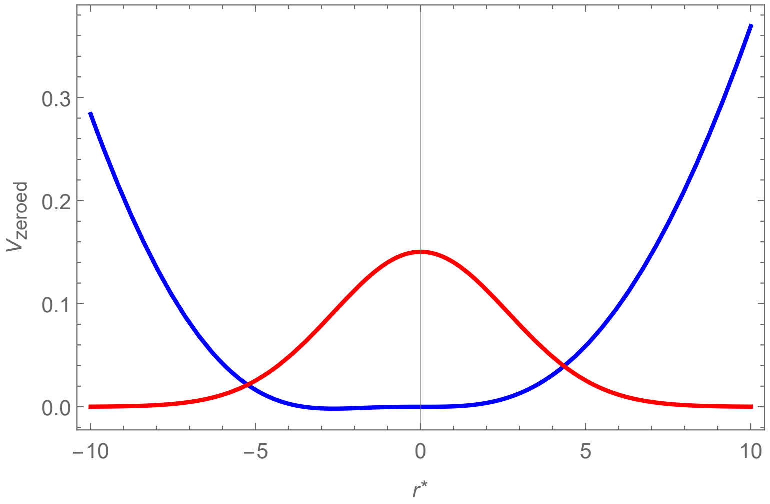

Figure 11: The blue curve represents the difference between the harmonic oscillator defined by equations 30 and 31 from the initial potential energy equation for $L = 1$ photons in the tortoise coordinate system. The region of interest is defined by the wave equation, shown in red. Near the outer limits of this wave function, the difference is no longer near 0, and therefore a perturbation must be introduced. [22]

Using perturbation theory techniques from quantum mechanics, a correction to the harmonic oscillator can be used to find a more accurate solution to the equation for the gravitational potential for a photon near a Schwarzschild black hole [22]. To utilize this perturbation theory correction method, harmonic oscillator energy eigenvalues were calculated using equation 37 and altered as seen in equation 33, where $E_n^{(0)}$ is the basic harmonic oscillator eigenvalue and higher order $E_n^{(x)}$ terms are corrections to that eigenvalue.

$$E_n = E_n^{(0)} + E_n^{(1)} + E_n^{(2)} + E_n^{(3)} + E_n^{(4)} + ... \tag{33}$$

$$E_{nm} = E_n^{(0)} - E_m^{(0)} \tag{34}$$

$$dV = V_{GR} - \frac{1}{2}kr^{*2} \tag{35}$$

$$dV_{nm} =< U_n^{(0)}|dV|U_m^{(0)} > \tag{36}$$

$$E_n^{(0)} =< n|\frac{1}{2}kr^{*2}|n > \tag{37}$$

$$E_n^{(1)} = dV_{nn} \tag{38}$$

$$E_n^{(2)} = \sum_{k_2} \frac{|dV_{nk_2}|^2}{E_{nk_2}} \tag{39}$$

$$E_n^{(3)} = \sum_{k_3,k_2} \frac{dV_{nk_3} dV_{k_2k_3} dV_{k_2n}}{E_{nk_2} E_{nk_3}} - dV_{nn} \sum_{k_3} \frac{dV_{nk_3}}{E_{nk_3}^2} \tag{40}$$

$$\begin{aligned} E_n^{(4)} = &\sum_{k_4,k_3,k_2} \frac{dV_{nk_4} dV_{k_4k_3} dV_{k_3k_2} dV_{k_2n}}{E_{nk_2} E_{nk_3} E_{nk_4}} - E_n^{(2)} \sum_{k_4} \frac{|dV_{nk_4}|^2}{E_{nk_4}^2} \\ &-2dV_{nn} \sum_{k_4,k_3,k_2} \frac{dV_{nk_4} dV_{k_3k_4} dV_{k_2n}}{E_{nk_3}^2 E_{nk_4}} + dV_{nn}^2 \sum_{k_4} \frac{|dV_{nk_4}|^2}{E_{nk_4}^3} \end{aligned} \tag{41}$$

These corrections are given in equations 38 through 41. Correction terms to a fourth perturbation were not calculated and provide a lesser correction to the overall value of the eigenvalue than the previous terms, making them less significant, and are seen to be significantly more difficult to calculate [22]. As the number of perturbation terms approaches infinity, the value of E_n approaches the true value for the energy eigenvalues for the gravitational potential energy well in the tortoise coordinate system. The base harmonic oscillator terms for L=2 gravitons of $n = 0$ to 6 are shown in table 2. These are used when calculating the perturbations for the n wavefunctions. More of these tables, for various particles and L states are given in appendix A.

Table 2: $E_n^{(0)}$ terms, in a basis of two harmonic oscillator wave functions for gravitons in the state L=2. These correction terms are used in the perturbation theory corrections. [22]

Harmonic Oscillator Eigenvalue	Numerical Calculation
$E_0^{(0)}$	0.0392
$E_1^{(0)}$	0.118
$E_2^{(0)}$	0.196
$E_3^{(0)}$	0.275
$E_4^{(0)}$	0.353
$E_5^{(0)}$	0.432
$E_6^{(0)}$	0.510

Table 3 gives values calculated for the perturbation method for the dV_{nm} terms for various combinations of $< U_n|$, $|U_m >$ and dV given by equation 36. Additional tables for these calculations are presented in appendix A.

Table 3: dV_{nm} terms for perturbation theory for various combinations of wave functions and dV, given by Equation 36 for gravitons in the L=2 state. The table is arranged such that the Bra and Ket are each with dV , producing the value for dV_{nm} at the location of the intersection on the table of the Bra and Ket. The intersection values represent the value of dV_{nm} where n is the wavefunction in the Bra and m is the wavefunction in the Ket. This is presented for a basis of seven harmonic oscillator wave functions. [22]

Wave Function	$\|U_0>$	$\|U_1>$	$\|U_2>$	$\|U_3>$	$\|U_4>$	$\|U_5>$	$\|U_6>$
$<U_0\|$	-.00421	-.0289	-.0169	.000893	-.00892	.000764	.00268
$<U_1\|$	-.0288	-.0281	-.0393	-.0471	.00349	-.0134	.000410
$<U_2\|$	-.0168	-.0393	-.0738	-.0480	-.0815	.00569	-.0167
$<U_3\|$	.000893	-.0471	-.0480	-.129	.0461	.117	.00760
$<U_4\|$	-.00892	.00349	-.0815	.0461	.191	-.0471	-.156
$<U_5\|$	.000764	-.0134	.00569	.117	-.0471	-.256	-.0475
$<U_6\|$	.00268	.000410	-.0167	.00760	-.156	-.0475	-.323

Tables 4 and 5 show the correction terms and overall values for the energy at different orders of perturbation theory for L=2 gravitons and L=1 photons respectively [22]. It is important to note that these values are measured from the bottom of the potential well, to the location of the energy level. This means the overall measurement of the energy level outside of this coordinate system will be different from the value shown, as the energy is related to the distance from the 0 potential ($V = 0$) line rather than the bottom of the potential well. The graviton resonances, which have a deeper well, will have a higher energy or lower frequency since the energy is measured from zero rather than from the bottom of the well.

Table 4: The central, Perturbation Value, column displays the correction terms calculated from perturbation theory. The Energy After Inclusion column shows the calculations from Equation 33, in a basis of seven, for perturbation theory corrections to harmonic oscillator energies for gravitons in the state L=2 of different orders of correction. [22]

Perturbation Order	Perturbation Value	Energy After Inclusion
$E_0^{(0)}$	.03927	.03927
$E_0^{(1)}$	-.004209	.03506
$E_0^{(2)}$	-.01270	.02235
$E_0^{(3)}$	-.007726	.01463

Table 5: The central, Perturbation Value, column displays the correction terms calculated from perturbation theory. The Energy After Inclusion column shows the calculations from Equation 33, in a basis of seven, for perturbation theory corrections to harmonic oscillator energies for photons in the state $L = 1$ of different orders of correction. [22]

Perturbation Order	Perturbation Value	Energy After Inclusion
$E_0^{(0)}$	.03542	.03542
$E_0^{(1)}$	-.00829	.02713
$E_0^{(2)}$	-.00419	.02294
$E_0^{(3)}$	-.00344	.01950

4.1.3 Energy States of Photons and Gravitons Near a Schwarzschild Black Hole

Since the tortoise coordinate system with the harmonic oscillator is shifted in the potential by an amount equal to the position of the bottom of the potential well, these energy eigenvalues relate to how high above the bottom of the well these eigenvalues exist [22]. The energy of the resonance is related to how far from the $V = 0$ line these eigenvalues are when related back into the original coordinate system. Figure 12 shows the graviton potential energy curve with a line showing the position of the energy eigenvalue for the potential well. This shows the distance above the bottom of the cavity as calculated by perturbation theory (section 4.1.2) as it applies to a real world case. The energy of this resonance is observably far below the energy required for a particle to leave the cavity and the measurable value of this resonance energy is equal to the negative value of the line rather than the distance from the bottom of the well, as calculated in section 4.1.2. The frequency is given by this negative value for the energy level.

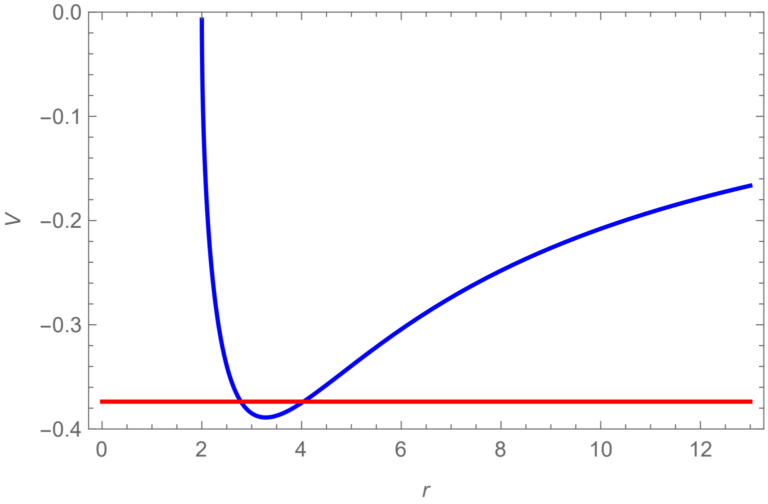

Figure 12: The blue curve displays the effective gravitational potential energy for a $L = 2$ graviton near a Schwarzschild black hole, given by equation 25. The red line is the location of the energy level calculated from perturbation theory corrections to third order given by table 4. [22]

Table 6 shows the calculated values of the square root of the normal modes from Fröman et al. for a scattering potential for varrying values of L and s [27]. These values at $n = 0$ give the same result calculated using the perturbation method, seen in section 4.1.2, when compared to the $V = 0$ line, which are compared in table 7, rather than the bottom of the potential well. The numerical equality of these values shows that either interpretation of the potential, as a scattering potential or potential well, is valid. While both a scattering interpretation and potential well interpretation explain the system, the potential well includes the idea of a leaky cavity based nature of the potential well [22]. This idea of a leaky cavity means the region is able to house photon or graviton resonances within their potential energy curves, which can lead to observational effects from the particles within these cavities interacting with infalling material. This is significantly closer to the black hole than the ISCO, which lies at $r = 6$ for a Schwarzschild black hole, since these wells exist at $r = 3.000$ for photons and $r = 3.281$ for gravitons. Both of these resonances are able to exist within the ISCO due to the standing wave nature of these massless particles. A standing wave introduces a stability that is not present in a short wavelength traveling wave.

Table 6: The square root of the normal modes calculated from the potential squared given by Equation 25 for different values of L and s. The n represents the nth mode for that iteration of L and s. States with $n = 0$ and $n = 1$ were included in this table but only $n = 0$ states were calculated in this thesis. The $n = 1$ states are shown to display the well behavior, shown in this section, of the normal modes. A line has been placed between the $s = 1$ and $s = 2$ values to show the change from photon to graviton modes. These values were calculated by Fröman et al. [27].

s	L	n	Real Part	Imaginary Part
1	1	0	0.2483	-0.09249
		1	0.2145	-0.2937
	2	0	0.4576	-0.09500
		1	0.4365	-0.2907
	3	0	0.6569	-0.09562
		1	0.6417	-0.2897
2	2	0	0.3737	-0.08896
		1	0.3467	-0.2739
	3	0	0.5994	-0.09270
		1	0.5826	-0.2813
	4	0	0.8092	-0.09416
		1	0.7966	-0.2843

Table 7: The real part of the normal modes represent the energy of the state. These values are comparable to the calculated values using the perturbation method when those values are measured from the zero energy line as opposed to the shifted potential used when comparing to the harmonic oscillator. [22]

s	L	Value from Scattering Potential	Value from Perturbation Theory	Percent Error
1	1	0.2483	0.2439	1.77%
2	2	0.3737	0.3731	0.161%

The imaginary component of the normal modes in table 6 introduces the leaky cavity nature of the resonance states, as this imaginary part of the frequency relates to the negative inverse of the half-life for particles of that energy. The most stable energy states, based on this half-life are the $n = 0$ states and the most stable states in L based on this half-life are the lowest L states ($L = 1$ for photons and $L = 2$ for gravitons) [22]. The energy value for the $n = 0$ states is also lower than that for higher values of n, indicating these latter states are less likely to be populated since they are not the lowest energy state.

It is then assumed that these most stable ($n = 0$) lowest energy ($L = 1$ for photons and $L = 2$ for gravitons) states are where the resonances would be most likely to be able to repopulate and would exist in highest quantity, so that these states have the dominant effect on particles within the region when compared to other states.

4.1.4 Effects of the Resonance Cavities Upon Infalling Electrons

As seen in section 2.3, the radiation of electrons near a black hole is based on synchrotron emission and is effected by the emission measure, in which emission is determined by the density squared rather than the density of electrons. These densities are influenced by the resonance phenomena near a black hole. The electrons are formed into bunches of higher density as they fall into the cavity region due to their charge and mass.

Photons exist as an oscillating electromagnetic field and have a dipole moment. This creates an effective dipole where the positive electric field section of the wave acts as a positive charge and the negative electric field section acts as a negative charge [22]. For a wavelength the size of this resonance state ($\lambda \approx 2\pi \times 3 = 2\pi \times 3\frac{GM}{c^2}$, since the wavelength must be nearly equivalent to the circumference of the region to be a standing wave), the electric field regions are significantly separated when compared to the size of an electron. This means the electrons will be attracted toward the positive electric field component of the resonance and will be repelled by the negative electric field component. This causes a bunching of the electrons based on charge.

Gravitons influence matter by the mass of the matter (electrons) in a quadrupole moment shape of the gravitons. The field for a graviton is more complex conceptually than that of a photon, but effectively the principle is the same. The electrons are forced into higher density bunches based on their mass. This bunching will be changed by the quadrupole moment to have two bunches per iteration of the frequency rather than one, as is the case with the photon resonance.

The emission measure model (section 2.3) indicates that this bunching of electrons as they fall into the region of interest will significantly change their synchrotron emissions [22]. The emission will be coherent and of higher intensity in the bunch regions when compared to the void regions. This will produce an oscillation in intensity of signal when observing the black hole. Since the synchrotron emission near a supermassive black hole will be in the Near-Infrared (NIR) spectrum, that spectrum should be studied for fluctuations in intensity with a periodic nature based on these resonances states. Similarly, the x-ray spectrum should be studied for stellar mass black holes, since the frequency is proportional to the inverse mass, and the wavelength is proportional to the mass.

4.2 Orbital Structure Surrounding Schwarzschild Black Holes

A major comparison for resonance state phenomena is the atomic model. The resonances for photons and gravitons surrounding a black hole were calculated using techniques that are often applied to the atomic model [22]. This shows that mathematically these two systems are not fundamentally different and should exhibit some of the same behaviors. An orbital nature to the resonances is one of these potential natures and is a consequence of looking at the potential energy as a negative potential as opposed to a scattering potential. The model itself is not far conceptually from an atomic model either. The black hole acts as an attractive center which creates a potential energy curve, similar to the nucleus of an atom [22].

Electrons in the atomic model exist in discreet energy levels, which is also seen to be true for these resonances, given the harmonic oscillator calculation method shown in section 4.1.2. A major difference from the atomic model is that photons and gravitons are both bosons, unlike electrons which are fermions, and so they are able to occupy the same state within the resonance and are not forced into higher order states by an exclusion principle [5]. This difference is emphasized by the inclusion principle, presented in section 4.1, which forces bosons into the same state. The existence of multiple bosons in the same state does not hinder the model, it just makes the ground state (the most stable, least energy state) to be more prominently populated than any other state and therefore have the more impact on nearby material.

In the atomic model, electrons are organized into orbitals based on their angular momentum. The organization of orbitals should not differ significantly for photons and gravitons around a black hole. The dipole moment and preferred $L = 1$ state for photons indicates they exist in a P-orbital shape, while the quadrupole moment and preferred $L = 2$ state for gravitons indicates they will exist in D-orbital shapes [22]. These orbital shapes for black holes with zero spin should be similar to those of the atomic model, presented in figures 13 and 14 for P-orbitals and D-orbitals respectively.

These orbitals are altered in size by the mass of the non-spinning black hole as compared to the reduced circumference to the resonance and by the difference in potential of the resonances from the potential in the atomic model, but these orbitals will at least serve as a base for understanding the orbital nature of these resonance states [22]. Notice how the D-orbital has two iterations of a positive and negative lobe per circumference in their own plane. This indicates that the graviton resonance will create two bunches per circumference when compared to the photon's one. The graviton resonance therefore, will create a more rapid intensity change when compared to the photon resonance for similar values of r for the resonance.

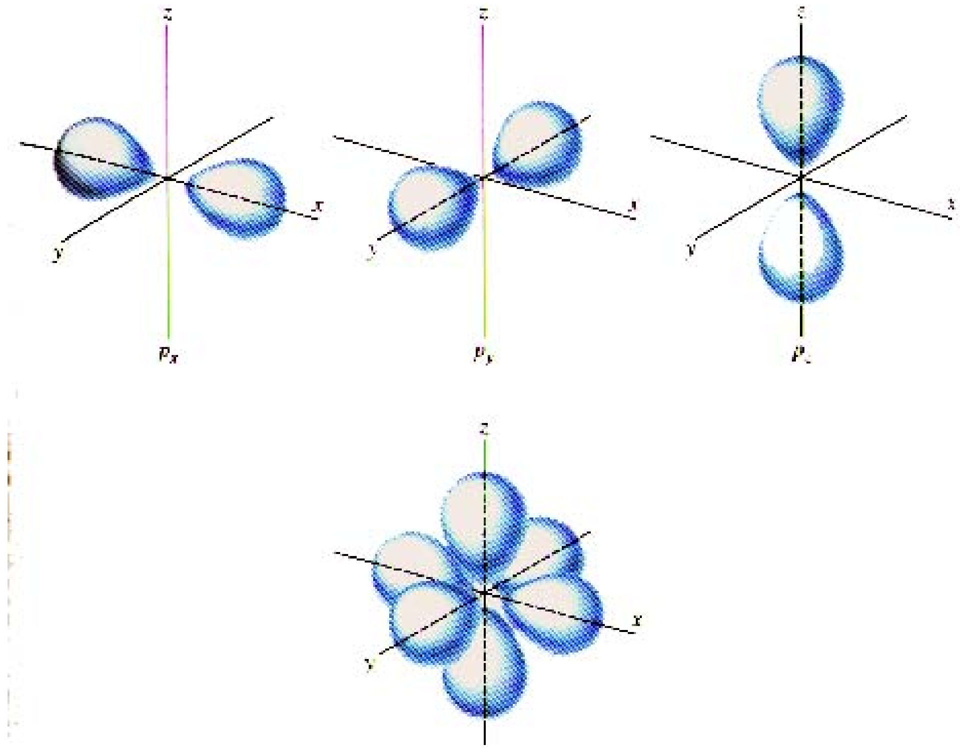

Figure 13: This shows the basic shape of a P-orbital from quantum mechanics. The Z-direction of the orbitals for a non-spinning black hole is defined by the magnetic field of the accretion disk. P-orbitals are the shape associated with L=1 angular momentum states, the shape of the orbital photons in the lowest energy state. (This image was taken from http://nanotech.sc.mahidol.ac.th/genchem/atom1/p-orb.jpg)

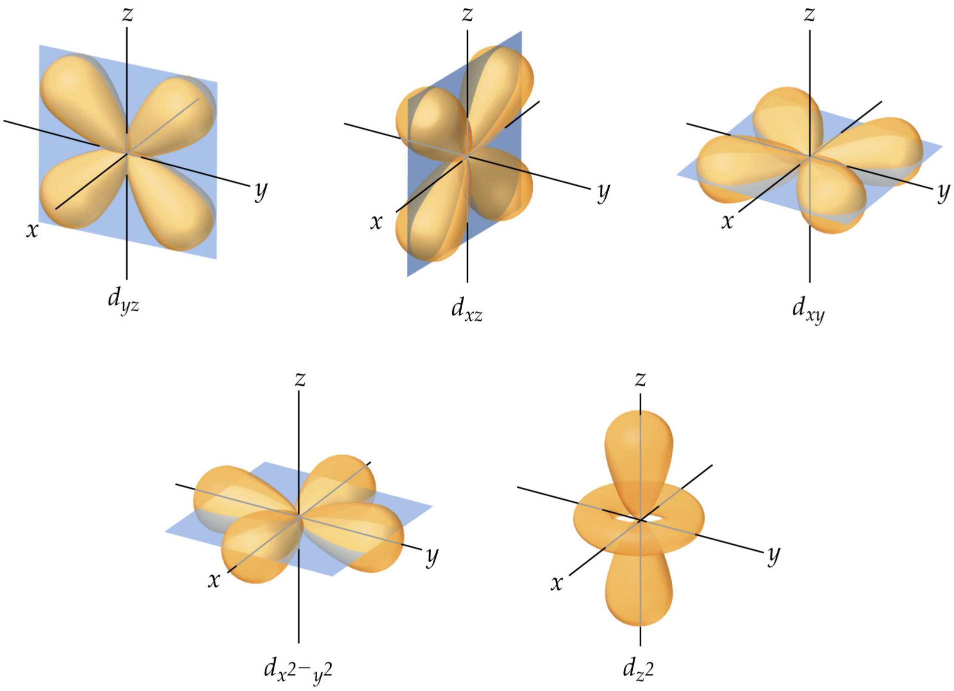

Figure 14: D-orbital shapes are typically the shape of L=2 states in quantum mechanics. The Z-direction is defined by the magnetic field of the accretion disk for a non-spinning black hole. This is the shape of the orbital containing the most stable graviton state. (This image was taken from http://chemistry.stackexchange.com/questions/2547/why-are-some-salt-solutions-coloured.)

5 Resonance Cavities Surrounding a Kerr Black Hole

Adding spin to the potential changes the effective potential curve of the particles in the region. This is due to the additional terms added into the Kerr metric. This changes the geometry of the space around the black hole and can pull the resonance states closer to (prograde spin) or farther from (retrograde spin) the singularity as is seen by the lowest point on the curves shown on the left in figure 15, for $a^* = 0.95$. Notice that the event horizon is closer to the singularity (r near 1) than in the Schwarzschild (non-spinning) case ($r = 2$). The bottom of the well is also deeper in figure15, which has prograde spin, than in the Schwarzschild case.

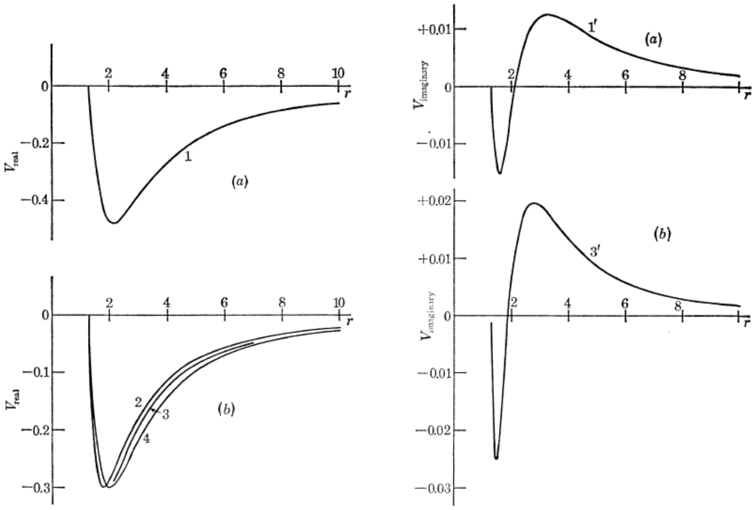

Figure 15: Potential energy curves for the L=-m=2 state for graviton particles around a Kerr black hole of spin parameter, $a^* = +0.95$. The real part of the potential is shown on the left side while the imaginary part is shown on the right. Notice the lowest part of the well is at the most stable location (imaginary part is 0). The real part of the well is also deeper, relating to a higher frequency when compared to the Schwarzschild (non-spinning) case. [23]

The deeper well indicates a larger separation of the real part of the eigenvalue from zero, meaning a higher frequency. A retrograde spin will have a shallower real part of the well, which indicates a lower frequency. The well in this case is farther from the singularity, requiring a larger wavelength to create a standing wave determined by the circumference of the black hole.

The singularity in figure 15 is located at $r = 0$. $V = 0$, similar to the Schwarzschild case (figure 8), is the event horizon. The major differences between the Kerr potential and the Schwarzschild potential are that the Kerr potential includes an imaginary component, which is not seen in the representation of the Schwarzschild potential given in equation 25 in section 4.1, though there is an imaginary component to the potential in the Schwarzschild metric, as is seen by the resonance states calculated by Fröman et al. [27] shown in table 6. The most stable position in the potential curve (where the imaginary component is 0, which relates to infinite half-life since half-life is inversely proportional to the imaginary component) shows the location of the deepest part of the potential well.

The position of the potential well is significantly pulled inward when compared to the Schwarzschild case, where $r = 3.281$ is the location of the deepest part of the potential well for gravitons. In the Kerr case (non-zero spin), with large spin ($a^* = 0.95$), the deepest part of the potential well is near $r = 2$, as seen in figure 15.Therefore the resonance circumference is smaller and the frequency is higher.

These resonance cavities will be altered by the spin of the black hole and will produce changes to the resonance states when compared to the Schwarzschild (non-spinning) case. The new resonance states will be calculated using solutions to the Teukolsky equation (equation 22) in section 3.3.2 for photon and graviton particles.

Solutions to the Teukolsky equation are presented in section 6, which provide the solutions to the energy levels of the states of photons and gravitons in the potential energy wells of a Kerr black hole.

5.1 Spin Changes Orbital Structure

Due to the effects of frame dragging in a Kerr black hole, it is believed that the orbital structure of photons and gravitons will be altered. The orbitals are likely to be dragged with the space-time as it curves around the black hole and therefore will be pulled into a spiral shape. This effect on the orbitals should not significantly alter the way electrons interact with the orbitals, as they will also be influenced by the frame dragging in the region.

The space which the orbitals occupy in the Schwarzschild case is shifted to spiral around the black hole to an outside observer, being rotated and condensed in the case of a prograde spinning black hole. This changes the effective distance the orbitals appear to occupy and brings them closer to the singularity, as it does with the space in the region of interest.

The bunches, as explained in the Schwarzschild case (section 4.1.4) should still be formed, but the periods of intensity fluctuation should decrease or increase as the spin increases in the prograde or retrograde direction respectively, as the potential well locations are pulled closer to or farther from the singularity.

6 Solutions to the Teukolsky Equation

There are several numerical solution methods to the Teukolsky equation (equation 22 on page 32), with varying complexity and convergences. The solutions to the Teukolsky equation give the Quasi-Normal-Modes (QNMs) for a Kerr black hole and are the solutions to the potential energy equation for the resonance states of particles in the Kerr metric in the near event horizon environment. The QNMs are similar to the normal modes calculated for a Schwarzschild black hole, though they include the spin of the black hole as a factor.

The two methods first considered for this work were (1) the solution method presented by Cook and Zalutskiy [19] which uses spin-weighted spheroidal harmonic functions which are spherical harmonic functions combined with angular spheroidal functions to create a spinning oblate spheroid geometry to satisfy the angular part of the Teukolsky equation and a confluent Heun function for the radial part, and (2) the continued fraction method used by Leaver [28], which uses a continued fraction method to solve the angular and radial parts of the Teukolsky equation then relate them to one another and to reasonable values of the angular separation constant to find an approximation for the proper solution.

The Cook and Zalutskiy method [19] requires a self consistent solution between the radial and angular parts through an iterative method after completing solution for the radial Heun function and a large pentadiagonal matrix solution method for the angular part. This pentadiagonal method is presented in equations 42 and 43. Equation 42 gives the matrix elements $M_{ll'}$ which are defined by equation 43 (c in this equation is a constant, not the speed of light).

$$M_{ll'} = \begin{cases} \text{if } l' = l-2\text{:} & -c^2 A_{sl'm}, \\ \text{if } l' = l-1\text{:} & -c^2 D_{sl'm} + 2csF_{sl'm}, \\ \text{if } l' = l\text{:} & {}_sA_{l'm}(0) - c^2 B_{sl'm} + 2csH_{sl'm}, \\ \text{if } l' = l+1\text{:} & -c^2 E_{sl'm} + 2csG_{sl'm}, \\ \text{if } l' = l+2\text{:} & -c^2 C_{sl'm}, \\ \text{otherwise:} & 0 \end{cases} \tag{42}$$

$$\begin{aligned} A_{slm} &= F_{slm}F_{s(l+1)m} \\ C_{slm} &= G_{slm}G_{s(l-1)m} \\ D_{slm} &= F_{slm}(H_{s(l+1)m} + H_{slm}) \\ B_{slm} &= F_{slm}G_{s(l+1)m} + G_{slm}F_{s(l-1)m} + H_{slm}^2 \\ E_{slm} &= G_{slm}(H_{s(l-1)m} + H_{slm}) \\ F_{slm} &= \sqrt{\frac{(l+1)^2 - m^2}{(2l+3)(2l+1)}}\sqrt{\frac{(l+1)^2 - s^2}{(l+1)^2}} \\ G_{slm} &= \begin{cases} \text{if } l \neq 0\text{:} & \sqrt{\frac{l^2-m^2}{4l^2-1}}\sqrt{\frac{l^2-s^2}{l^2}}, \\ \text{if } l = 0\text{:} & 0 \end{cases} \\ H_{slm} &= \begin{cases} \text{if } l \neq 0 \text{ and } s \neq 0\text{:} & \frac{ms}{l(l+1)}, \\ \text{if } l = 0 \text{ or } s = 0\text{:} & 0 \end{cases} \end{aligned} \tag{43}$$

While the Cook and Zalutskiy solution method is a valid solution to the Teukolsky equaiton and is important to present as it represents other solution methods for the Teukolsky equation, the continued fraction method is more rapidly converging and with fewer iterations, high levels of significance can be calculated.

The continued fraction method, due to its relative simplicity and rapid convergence, is the prefered method for calculating the QNM solutions to the Teukolsky equation for this work and is presented in section 6.1. [28]

6.1 Continued Fraction Solution to the Teukolsky Equation [28]

In the unit system preferred by Leaver, $c = G = 2M = 1$, which differs from the standard GR unit system in that this unit system places the event horizon at $r = 1$ rather than $r = 2$. Having the singularity at $r = 1$ scales the geometry but allows for certain mathematical techniques that would be more difficult if the location of the event horizon were at $r = 2$. This must be considered when interpreting the results from this solution method as compared to other solution methods which use $c = G = M = 1$ as a unit system.

Leaver, in his solution method [28], uses the field quantity equations given by Teukolsky [29] for ψ in the Teukolsky equation, equation 44 (u is a substitution for $\cos(\theta)$).

$$\psi(t, r, \theta, \phi) = \frac{1}{2\pi} \int e^{-i\omega t} \sum_{l=|s|}^{\infty} \sum_{m=-l}^{l} e^{im\phi} S_{lm}(u) R_{lm}(r) d\omega \tag{44}$$

Teukolsky gives the equations for $S_{lm}(u)$ and $R_{lm}(r)$ as shown in equations 45 and 46 respectively. The $V(r)$ in equation 46 is defined by equation 47 and Δ is defined by equation 48. These are the separated differential equations for the Teukolsky wave equation.

$$[(1-u^2)S_{lm,u}]_u + \left[a^2\omega^2u^2 - 2a\omega su + s + A_{lm} - \frac{(m+2u)^2}{1-u^2}\right]S_{lm} = 0 \tag{45}$$

$$\Delta R_{lm,rr} + (s+1)(2r-1)R_{lm,r} + V(r)R_{lm} = 0 \tag{46}$$

$$\begin{aligned} V(r) = \{[(r^2+a^2)^2\omega^2 - 2am\omega r + a^2m^2 + is(am(2r-1) - \omega(r^2-a^2))]\Delta^{-1} \\ +[2is\omega r - a^2\omega^2 - A_{lm}]\} \end{aligned} \tag{47}$$

$$\Delta = r^2 - r + a^2 \tag{48}$$

In the unit system used by Leaver [28] (Leaver unit system), the a is a spin parameter (the angular momentum per unit mass) as presented in section 3.3 but this value is restricted to $-\frac{1}{2} \leq a \leq \frac{1}{2}$ due to the differing unit for the mass component. This relates to a percent of the total mass that is due to spin, the maximum of which is 50%. This is compared to the unit system where $c = G = M = 1$, where a ranges from -1 to 1, as it relates to a maximum spin value of the speed of light, c. In the Leaver unit system, the mass scaling of the angular momentum introduces a factor of $\frac{1}{2}$ into the spin parameter, changing the numerical limits of the spin parameter and their meaning, but not the overall effect when scaled between the two systems. Recall in a unit system where a is scaled by mass, $a = a^*$.

The s in equations 45 through 47 is the spin-weight field parameter, equivalent to the s presented in section 3.3 ($s = 0, \pm 1, \pm 2$ for scalar, electromagnetic, and gravitational fields respectively). The value u in the angular system is $\cos\theta$ and represents substitution for the value of θ. A_{lm} is the angular separation constant, which in the Schwarzschild case reduces to $l(l+1) - s(s+1)$, where convention dictates that s=-1, and -2 for electromagnetic and gravitational fields respectively. In the Kerr case, this value must be calculated in the method by a system of continued fraction equations when calculating ω and gives a selection method for choosing the proper solution from the list generated by this method.

6.1.1 Solutions to the Angular Part of the Teukolsky Equation

The boundary conditions set on S_{lm} are such that it is finite at the singular points $u = \pm 1$, where the indices are $\pm\frac{1}{2}(m+s)$ and $\pm\frac{1}{2}(m-s)$ for the positive and negative bounds respectively. This gives a solution, as shown by Baber and Hassé [30], to the angular component of the Teukolsky equation to be given by equation 49, where $k_1 = \frac{1}{2}|m-s|$ and $k_2 = \frac{1}{2}|m+s|$.

$$S_{lm}(u) = e^{a\omega u}(1+u)^{k_1}(1-u)^{k_2}\sum_{n=0}^{\infty} a_n(1+u)^n \tag{49}$$

A set of expansion coefficients are related by a three-term recursion relation for the continued fraction for the angular equation (indicated by the superscript θ), given in equation 50, where the boundary condition $u = 1$ is only satisfied for minimum solution sequences.

$$\begin{aligned} &\alpha_0^\theta a_1 + \beta_0^\theta a_0 = 0 \\ &\alpha_n^\theta a_{n+1} + \beta_n^\theta a_n + \gamma_n^\theta a_{n-1} = 0 \text{ where } n = 1, 2... \end{aligned} \tag{50}$$

This recursion relation gives solutions for the angular part of the Teukolsky equation with the coefficients presented in equation 51.

$$\begin{aligned} \alpha_n^\theta =& -2(n+1)(n+2k_1+1) \\ \beta_n^\theta =& n(n-1) + 2n(k_1+k_2+1-2a\omega) \\ & - [2a\omega(2k_1+s+1) - (k_1+k_2)(k_1+k_2+1)] - [a^2\omega^2 + s(s+1) + A_{lm}] \\ \gamma_n^\theta =& 2a\omega(n+k_1+k_2+s) \end{aligned} \tag{51}$$

These coefficients give a continued fraction equation which will satisfy the minimal solution requirement, imposed by the $u = 1$ boundary condition when the A_{lm} is a root of the continued fraction given in equation 52.

$$0 = \beta_0^\theta - \frac{\alpha_0^\theta \gamma_1^\theta}{\beta_1^\theta -} \frac{\alpha_1^\theta \gamma_2^\theta}{\beta_2^\theta -} \frac{\alpha_2^\theta \gamma_3^\theta}{\beta_3^\theta -} ... \tag{52}$$

Equation 52 represents a solution continued fraction to the angular part of the Teukolsky equation, but with three unknown variables, ω, a and A_{lm}. This solution will need to be combined with another solution to solve for these variables. The radial part of the Teukolsky equation has the same unknown variables, and so with a constraint on the A_{lm} terms, a solution for ω or a as a function of the other can be obtained.

As the spin parameter a approaches 0, the angular separation constant, A_{lm} approaches the Schwarzschild value, $A_{lm} \to n(n+1) - s(s+1) \to l(l+1) - s(s+1)$ since $\beta_n^\theta = 0$ for $n = l$ values in this case. This shows the behavior of this solution gives the proper value as the Schwarzschild limit is approached, which is necessary for agreement between the Kerr and Schwarzschild metrics when spin is 0.

6.1.2 Solutions to the Radial Part of the Teukolsky Equation

The solution to the radial equation is similar to the solution to the angular part. Both equations are spheroidal wave equations and have similar boundary conditions. This means that the process for finding the continued fraction solution will be relatively similar, as explained by Leaver. [28]

The regular singular points in the radial equation exist such that the roots of Δ are given by equation 53. These singular points are required to define boundary conditions on the radial equation.

$$\Delta = r^2 - r + a^2 \equiv (r - r_-)(r - r_+) \tag{53}$$

Leaver defines a rotational parameter, b, with equaiton 54 to create a simple expression for the $r_\pm$ terms and to simplify the mathematics for the boundary conditions. This b rotational parameter is easily related back to the spin parameter, a, when it is necessary to calculate the spin parameter.

$$b = \sqrt{1 - 4a^2} \tag{54}$$

This rotational parameter ranges from 0 to 1, as $|a|$ goes from 0 to $\frac{1}{2}$. This gives

$r_\pm$ in the Δ constraint (equation 53) as defined by equation 55.

$$r_\pm = \frac{1}{2}(1 \pm b) \tag{55}$$

Notice that for the Schwarzschild case, $(a = 0)$, the rotation parameter, b (equation 54), is 1, making the event horizon at location $r_+ = 1$ (equaiton 55) as is expected in the Schwarzschild case in the $c = G = 2M = 1$ unit system. Similarly, the r_- value for a Schwarzschild black hole can be calculated to be $r_- = 0$ which gives the location of the singularity within the black hole. This shows that the location of r_- is somewhere within the event horizon and represents a ring singularity rather than a point singularity. The r_- will be ignored as a boundary in this solution, as r_- exists inside the event horizon. The primary boundary for infalling material is at the outer event horizon, r_+. The boundary condition at r_+ gives indices $i\sigma_+$ and $-s - i\sigma_+$, where σ_+ is defined by equation 56.

$$\sigma_+ = \frac{\omega r_+ - am}{b} \tag{56}$$

Teukolsky [29] gives two asymptotic solutions for the radial equation, one related to the outgoing material and one related to infalling material. These are presented in equaion 57.

$$\begin{aligned} \lim_{r\to\infty} R_{lm} &\sim r^{-1-i\omega r} e^{-i\omega r} \\ \lim_{r\to\infty} R_{lm} &\sim r^{-1-2s+i\omega} e^{+i\omega r} \end{aligned} \tag{57}$$

This gives two solutions including boundary conditions, one as $r \to r_+$ as material falls in and one as $r \to \infty$ as material falls away. These are given in equation 58.

$$\begin{aligned} R_{lm} &\xrightarrow{r \to r_+} (r - r_+)^{-s-i\sigma_+} \\ R_{lm} &\xrightarrow{r \to \infty} r^{-1-2s+i\omega} e^{i\omega r} \end{aligned} \tag{58}$$

These two equations can be combined to form an expression for R_{lm} given in equation 59.

$$R_{lm} = e^{i\omega r}(r - r_-)^{-1-s+i\omega+i\sigma_+}(r - r_+)^{-s-i\sigma_+} \sum_{n=0}^{\infty} d_n \left(\frac{r - r_+}{r - r_-} \right)^n \tag{59}$$

Similar to the angular recursion relation equation (equation 50), this radial equation has expansion coefficients defined by a three-term resursion relation, given in equaiton 60, where the superscript r identifies these as the radial recursion terms.

$$\begin{gathered} \alpha_0^r d_1 + \beta_0^r d_0 = 0 \\ \alpha_n^r d_{n+1} + \beta_n^r d_n + \gamma_n^r d_{n-1} = 0 \text{ where } n = 1, 2... \end{gathered} \tag{60}$$

These relations are similar to those in the angular equation, though the coefficients will differ. This similarity is due to the similar form of the summation terms in the two equations (equations 50 and 60) and does create the same form of continued fraction as the angular solution (equation 52) for the radial equation (equation 61).

$$0 = \beta_0^r - \frac{\alpha_0^r \gamma_1^r}{\beta_1^r -} \frac{\alpha_1^r \gamma_2^r}{\beta_2^r -} \frac{\alpha_2^r \gamma_3^r}{\beta_3^r -} ... \tag{61}$$

The coefficients for the radial equation are given in equation 62, with terms defined in equation 63.

$$
\begin{aligned}
\alpha_n^r &= b[n^2 + (c_0 + 1) + c_0] \\
\beta_n^r &= b[-2n^2 + (c_1 + 2)n + c_3] \\
\gamma_n^r &= b[n^2 + (c_2 - 3)n + c_4 - c_2 + 2]
\end{aligned}
\tag{62}
$$

$$
\begin{aligned}
c_0 &= 1 - s - i\omega - \frac{2i}{b}\left(\frac{\omega}{2} - am\right) \\
c_1 &= -4 + 2i\omega(2 + b) + \frac{4i}{b}\left(\frac{\omega}{2} - am\right) \\
c_2 &= s + 3 - 3i\omega - \frac{2i}{b}\left(\frac{\omega}{2} - am\right) \\
c_3 &= \omega^2(4 + 2b - a^2) - 2am\omega - s - 1 + (2 + b)i\omega - A_{lm} + \frac{4\omega + 2i}{b}\left(\frac{\omega}{2} - am\right) \\
c_4 &= s + 1 - 2\omega^2 - (2s + 3)i\omega - \frac{4\omega + 2i}{b}\left(\frac{\omega}{2} - am\right)
\end{aligned}
\tag{63}
$$

The roots of the continued fraction, equation 61, give the ω value for a given a, m, A_{lm} and s. Notice that in the necessary limit of $a \to 0$ the A_{lm} term approaches the necessary value of $l(l+1) - s(s+1)$ for agreement between the Schwarzschild and Kerr metrics at their common value of spin ($a = 0$).

6.2 Creating a Solution for Black Hole Spin

The two solutions for the separable terms in the Teukolsky equation, as solved by Leaver, give a set of two equations with three unknowns. This can be used to relate two of the variables through a common one. In this case, the relation desired is between the spin parameter, a (a=a^*), and the QNM angular frequency, ω.

These solutions must be obtained through a numerical iterative solution method using a system of two continued fractions.

Mathematica's [31] ContinuedFractionK function was the preferred method for the input of these continued fractions which allowed for a solution to be calculated using the NSolve function. The Mathematica coding used is provided in appendix B and shows the definitions for these continued fractions in the Mathematica syntax, as well as the definition coding for the solution terms for these equations.

Using guidlines set by Leaver for number selection for the proper solutions, the numerical values for a given spin parameter were defined by the most stable (imaginary value nearest 0) angular separation constant (A_{lm}) values and angular frequency (ω) for A_{lm} value less than $l(l+1) - s(s+1)$ for prograde spin and greater than $l(l+1) - s(s+1)$ for retrograde spin. This selection criteria is set due to the most probable state being the most stable (least imaginary component) and the nature of the change in angular particle separation (angular separation constant A_{lm}) as spin increases in the prograde or retrograde direction to define prograde or retrograde. Table 8 gives the calculated values for a black hole of spin $a = 0.05$ and a particle of $s = m = -2$. The state $m = -2$ is the preferred state for gravitons (most stable, imaginary part closest to zero), and the convention for $s = -2$ is preferred in literature for gravitons.

The critical value to determine prograde and retrograde spin is based on whether the separation constant is greater than or less than the separation constant for a Schwarzschild black hole. The angular separation constant for a Schwarzschild black hole is given by $A_{lm} = l(l+1) - s(s+1)$ which gives a Schwarzschild value (Kerr critical value) to be $A_{lm} = 4$ and $A_{lm} = 2$ for lowest energy (highest frequency) gravitons and photons respectively.

Table 8: Solutions given to the Teukolsky equation from the continued fraction method for an $l = -s = -m = 2$ graviton around a prograde spinning black hole ($\text{Re}[A_{lm}] < l(l+1) - s(s+1) = 4$). For retrograde spin (not shown here), $\text{Re}[A_{lm}] > l(l+1) - s(s+1) = 4$.

$\text{Re}[A_{lm}]$	$\text{Im}[A_{lm}]$	$\text{Re}[\omega]$	$\text{Im}[\omega]$
3.9746	-0.136204	0.40785	-2.02908
3.9644	-0.099968	0.54652	-1.48666
3.9578	-0.066858	0.63433	-0.99263
3.9525	-0.037723	0.70950	-0.55933
3.9490	-0.012081	0.75952	-0.17899

In Table 8 the proper values to be selected are $A_{lm} = 3.9490 - 0.012081i$ and $\omega = 0.75952 - 0.17899i$ as these meet the criteria of being the most stable (smallest value of $\text{IM}[A_{lm}]$ and $\text{IM}[\omega]$). This ω can be related back to a real world value by using the conversion factor for frequency from section 2.1 ($\omega_{Hz} = \omega\frac{c^3}{GM}$). Recall ω is an angular frequency, and it must be divided by 2π when comparing to frequency.

The value for various spin parameters ($0 \leq a < 0.5$) are given in table 9 and 10 for gravitons and photons respectively near a prograde spinning black hole and table 11 and 12 for gravitons and photons respectively near a retrograde spinning black hole. These values were calculated at $n = 4$ in the Mathematica code, as this was the minimum value required to get three significant figure accuracy. The limitation on n significantly reduced the required time to process the code and, due to the quick convergence of the continued fraction method, had little impact on the accuracy of the solution.

Table 9: The solutions for $l = -m = 2$ gravitons around a prograde spinning black hole for various spin parameters ($0 \leq a < 0.5$).

Spin Parameter (a)	Re[ω]	Im[ω]
0	0.7467	-0.17914
0.025	0.759522	-0.17899
0.05	0.773405	-0.178583
0.075	0.788065	-0.177676
0.1	0.803831	-0.177625
0.125	0.820635	-0.177035
0.15	0.83871	-0.176331
0.175	0.858211	-0.175536
0.2	0.879416	-0.174593
0.225	0.902543	-0.173424
0.25	0.927992	-0.172037
0.275	0.956266	-0.17029
0.3	0.9878	-0.1681
0.325	1.02375	-0.165545
0.35	1.065	-0.162188
0.375	1.11341	-0.157778
0.4	1.17179	-0.151923
0.425	1.24494	-0.143445
0.45	1.342266	-0.130424
0.475	1.49082	-0.1072214
0.4999	1.91283	-0.00752466

Table 10: The solutions for $l = -m = 1$ photons around a prograde spinning black hole for various spin parameters ($0 \leq a < 0.5$).

Spin Parameter (a)	Re[ω]	Im[ω]
0	0.498103	-0.185097
0.025	0.504587	-0.184918
0.05	0.51165	-0.184407
0.075	0.519157	-0.183804
0.1	0.52722	-0.182958
0.125	0.535741	-0.182144
0.15	0.544862	-0.181202
0.175	0.554665	-0.1801
0.2	0.565244	-0.178804
0.225	0.576704	-0.177313
0.25	0.589054	-0.175701
0.275	0.60294	-0.173431
0.3	0.618137	-0.170918
0.325	0.635137	-0.167872
0.35	0.654404	-0.164115
0.375	0.676616	-0.159395
0.4	0.702838	-0.153246
0.425	0.734858	-0.144922
0.45	0.775848	-0.132011
0.475	0.835966	-0.110559
0.4999	0.964367	-0.00666179

Table 11: The solutions for $l = -m = 2$ gravitons around a retrograde spinning black hole for various spin parameters ($0 \leq a < 0.5$).

Spin Parameter (a)	Re[ω]	Im[ω]
0	0.7467	-0.17914
0.025	0.734156	-0.179576
0.05	0.72232	-0.179896
0.075	0.711119	-0.180128
0.1	0.700562	-0.180264
0.125	0.690184	-0.180525
0.15	0.680265	-0.180743
0.175	0.670823	-0.180902
0.2	0.661543	-0.181112
0.225	0.652311	-0.181383
0.25	0.643229	-0.18165
0.275	0.634176	-0.181951
0.3	0.624929	-0.182318
0.325	0.615312	-0.182758
0.35	0.60481	-0.183346
0.375	0.592865	-0.184182
0.4	0.578144	-0.185549
0.425	0.557768	-0.188129
0.45	0.525857	-0.194322
0.475	0.461797	-0.215211
0.4999	0.0716654	-0.466235

Table 12: The solutions for $l = -m = 1$ photons around a retrograde spinning black hole for various spin parameters ($0 \leq a < 0.5$).

Spin Parameter (a)	Re[ω]	Im[ω]
0	0.498103	-0.185097
0.025	0.491602	-0.185786
0.05	0.485604	-0.186146
0.075	0.479912	-0.186467
0.1	0.474608	-0.186642
0.125	0.469439	-0.186946
0.15	0.46453	-0.187224
0.175	0.459835	-0.187515
0.2	0.455358	-0.187822
0.225	0.45101	-0.188211
0.25	0.446826	-0.188666
0.275	0.442751	-0.18924
0.3	0.438748	-0.18998
0.325	0.43471	-0.190976
0.35	0.430532	-0.192331
0.375	0.425989	-0.194231
0.4	0.420635	-0.196694
0.425	0.413494	-0.201251
0.45	0.401719	-0.208552
0.475	0.374743	-0.224841
0.4999	0.00817686	-0.444966

Using the data in tables 9 through 12, the graphs in figures 16 through 19 were made and the best linear fit was found using a least squares linear regression of polynomial terms, as is seen in the coding in appendix B. The regression equations are given by equations 64 and 65 for gravitons and photons around a prograde black hole and equations 66 and 67 for gravitons and photons around a retrograde spinning black hole. The values, standard errors, t-statistics, and P-values for the coefficients of these regression equations are given in appendix C. All are shown to be significant. The statistical R^2 values for these equations are 0.99865, 0.999542, 0.996823, and 0.991043 for equations 64, 65, 66 and 67 respectively. P-values for these equations are presented in Appendix C. The accuracy of the fit was needed to ensure that the limiting factor on the method was the numerical data, which is presented later in this work. The accuracy of the theoretical work can, if need be for future study, be improved by increasing the number of iterations in the continued fraction calculation, by increasing the accuracy in the parameters of the fit, or by including additional polynomial orders in the fit.

$$\omega^{pro}_{s=-2} = 0.753992 + 161.815a^3 - 1704.27a^4 + 7231.43a^5 - 13803.4a^6 + 9873.49a^7 \quad (64)$$

$$\omega^{pro}_{s=-1} = 0.503623 + 62.3338a^3 - 602.75a^4 + 2407.49a^5 - 4391.5a^6 + 3036.52a^7 \quad (65)$$

$$\omega_{s=-2}^{retro} = 0.750033 - 42.104a^2 + 922.524a^3 - 8925.12a^4 + 45012.1a^5 \\ -123042.a^6 + 172750a^7 - 97625.9a^8 \tag{66}$$

$$\omega_{s=-1}^{retro} = 0.503433 - 37.407a^2 + 899.149a^3 - 9063.91a^4 + 46748.8a^5 \\ -129507a^6 + 183312a^7 - 104067.a^8 \tag{67}$$

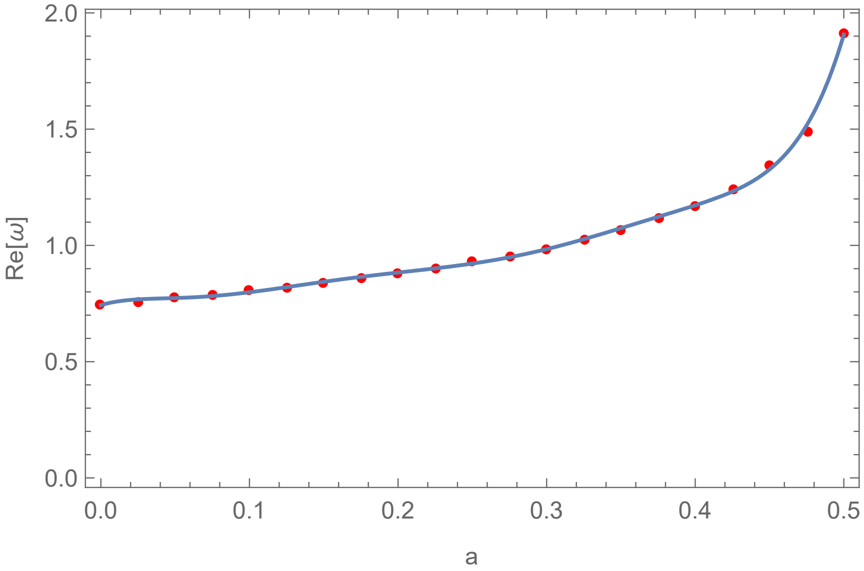

Figure 16: Data and linear regression for gravitons of $l = -m = 2$ around a prograde spinning black hole. The data for the points is calculated to be correct to four significant figures, as is determined by the number of iterations in the continued fraction used, and so the associated error is less than the size of the point on the graph.

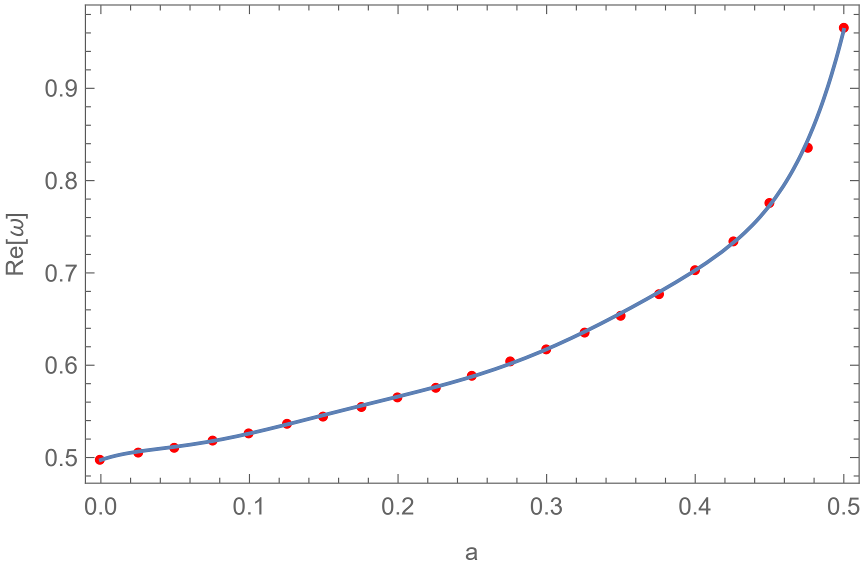

Figure 17: Data and linear regression for photons of $l = -m = 1$ around a prograde spinning black hole. The data for the points is calculated to be correct to four significant figures, as is determined by the number of iterations in the continued fraction used, and so the associated error is less than the size of the point on the graph

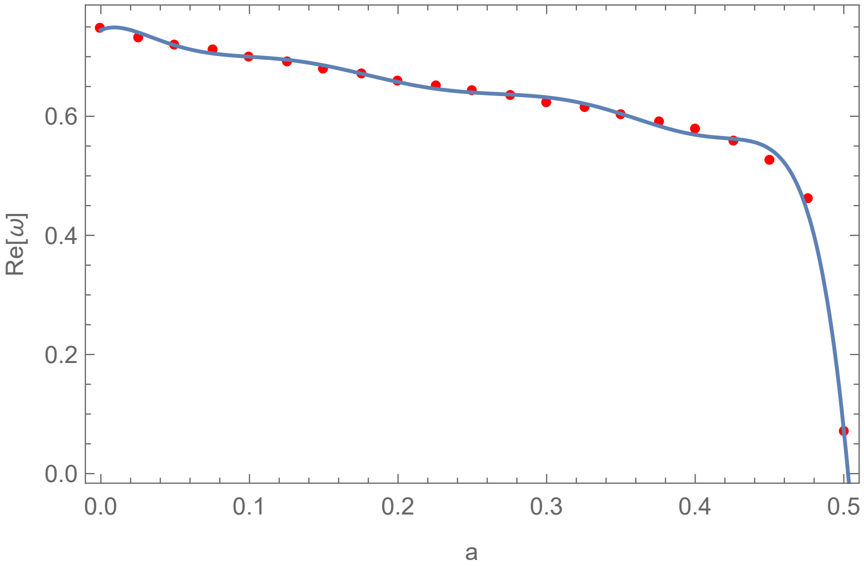

Figure 18: Data and linear regression for gravitons of $l = -m = 2$ around a retrograde spinning black hole. The data for the points is calculated to be correct to four significant figures, as is determined by the number of iterations in the continued fraction used, and so the associated error is less than the size of the point on the graph

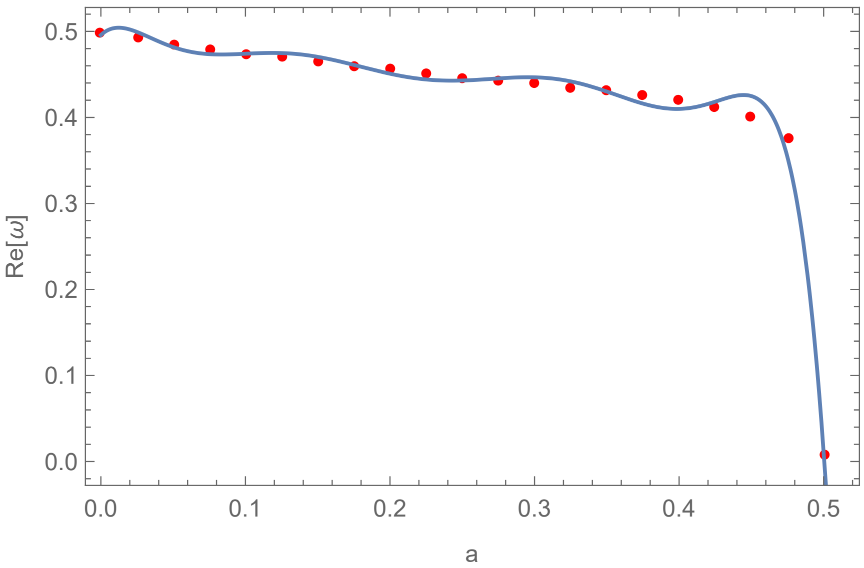

Figure 19: Data and linear regression for photons of $l = -m = 1$ around a retrograde spinning black hole. The data for the points is calculated to be correct to four significant figures, as is determined by the number of iterations in the continued fraction used, and so the associated error is less than the size of the point on the graph

Solving these linear regression equations (equations 64 through 67) for the spin as a function of ω gives a function for spin which can be calculated from a known angular frequency of the QNM resonance state, as shown in the coding in appendix B for the ProPeriodSolve, RetroPeriodSolve, ProFreqSolve, and RetroFreqSolve functions. The spin parameter, a^*, must be real and when using the prograde equations, the spin must be positive. Likewise for the retrograde case, the spin must be positive and real, understanding that the solution equation gives a positive value for a which relates to a negative a^* since the equation is valid only for retrograde spinning black holes, which by convention have a negative a^*. These constraints give only one solution for a^* when using a numerical solve method. If a solution is not possible for a set of given frequencies for a prograde solution, it is likely the black hole is instead in retrograde, and the retrograde equations must be used.

The graviton and photon states must give consistent values for the spin of the black hole to within a reasonable amount of error based on the regression equations. This self consistency requirement forces a constraint on the possible values for the spin, though the solutions are heavily dependent on mass when converted back into real world measurable units. This is discussed further in section 8.

7 NIR and X-Ray Observation of Black Holes

The QNMs for a Kerr black hole can be related to observational phenomena, similar to the effect in the Schwarzschild case presented in section 4.1.4. The NIR or x-ray emission from accelerated electrons falling through the cavity region is used as an effective measurement tool to probe the region. Falling electrons interact with the photon cavity due to their charge and the graviton cavity due to their mass, causing a bunching of electrons which results in an increased emission due to the emission measure. The bunching of electrons causes a fluctuation in the intensity of radiation based on the cycle of the standing waves in the resonance cavity.

7.1 Sgr A*

Analyzing emissions from Sgr A* is difficult due to the amount of dust in the space between earth and the galactic center. This dust is not the typical definition of dust humans think of, but rather small particulates that exist within seemingly empty space. Over large distances these dust particles can effectively block photons which are traveling through it. For light to pass beyond the dust, the wavelength must be longer than the size of the particle, as anything smaller will reflect off of or be adsorbed by the particle. NIR radiation is typically able to penetrate the dust that exists between the Earth and Sgr A*. This makes NIR the preferred wavelength range to study when studying Sgr A* or other far objects in our galaxy.

X-ray emissions are also often studied for astronomical bodies due to their small wavelength, as this small wavelength relates to a small physical size, which makes it possible for an x-ray to statistically avoid dust. This means the overall x-ray signal will be significantly diminished, since many x-ray photons will interact with dust, but some x-ray emissions will be able to be observed as they are the ones that were able to avoid the dust entirely before reaching Earth. For closer objects, x-ray may be a preferred frequency range, but the amount of dust lowers the probability of x-rays reaching the Earth from Sgr A* and therefore NIR is still preferred.

Genzel et al. [32] analyzed data from the supermassive black hole Sgr A* in 2003, to study the pattern on subflares duing a flare event of the black hole. Their data is presented in figure 20. While this analysis was not directly related to this work, the NIR data they collected provides the necessary data to see the QNMs of Sgr A* which can be related through the solutions for the Teukolsky equation to a value for the spin.

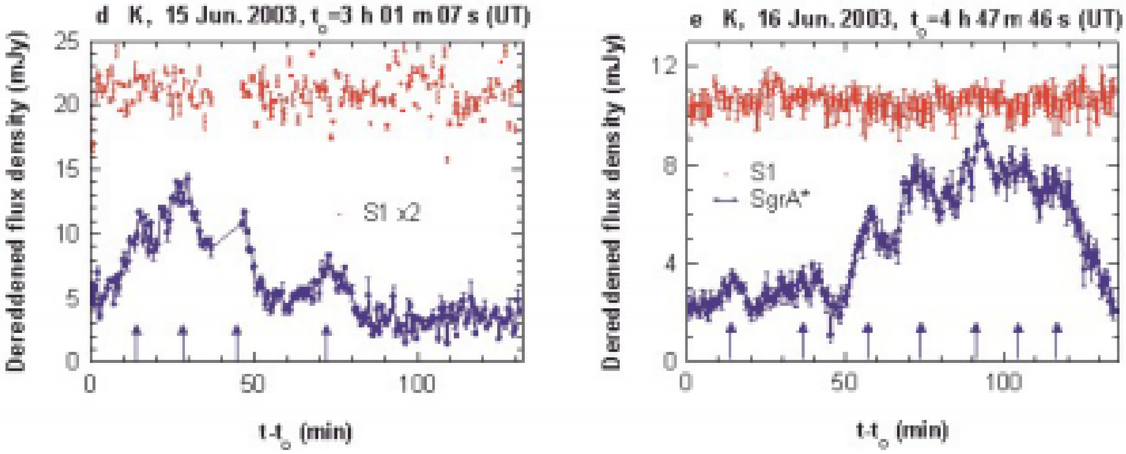

Figure 20: NIR data of Sgr A* when it is flaring. The quiescent oscillations show two frquencies which can be calculated to be around 4.8 ± 0.1min and 7.35 ± 0.1min. This is roughly a 3:2 ratio of the frequencies. The arrows indicate locations of subflares, which occur near every 2 and 3 iterations of the desired periods [32]. This image is used with expressed permission. See appendix D for documentation.

The Genzel et al. data [32] show a quiescent oscillation signal that disappears and reappears within the small intensity fluctuations that exist above the Nyquist frequency. This did not, however, appear on their Fourier analysis due to the inability for a Fourier transform to pick up a constantly appearing and disappearing signal. If the signal is not onmipresent it is significantly reduced in amplitude when compared to other frequencies in a Fourier analysis. These frequencies of 4.8 ± 0.1 min and 7.35 ± 0.1 min were calculated by hand and through observation of the numerical data presented by Genzel et al. By observing the peaks in their numerical data, the periods were determined by comparing distances between peaks over long time periods. The periods were assumed to be stable and continue in phase. The periods occasionally disappeared for several cycles but would reappear in perfect phase with the previous peak. This reappearance after a random number of cycles allowed for a determination of the number of oscillations for which the signal was suppressed and value of the periods. Even when comparing between the two days, these peaks remained in phase between the two completely different sets of data.

These periods represent a fluctuation in electron emission on a millihertz scale and correspond to the QNMs for a black hole the size of Sgr A*, as is discussed further in section 8.

It is expected that the appearance and disappearance of these periods is due to the infrequency of material falling into Sgr A*. The signal is only produced as electrons fall into the near black hole environment (below the ISCO), which is time dependent. For a black hole that is not actively accreting material, the rate of electrons falling into this region will not be steady and therefore the signal from these electrons will also not be consistent.

7.2 Stellar Mass Black Hole Binaries

Stellar mass black holes in a binary system are constantly fed by their companion star and therefore are actively accreting material. This active accretion allows them to have a relatively constant inflow of material, making a Fourier analysis viable for these black holes. The time dependence of the signal heavily impacts a Fourier analysis, and for these black holes, the constant infall of material means there is little time dependence for an actively accreting black hole.

Remillard and McClintock [4] show a Fourier analysis for several stellar mass black hole binaries (figure 21), the most commonly studied of which is GRS1915+105. GRS1915+105 is a rapidly spinning black hole binary that is relatively nearby and provides a strong signal. It is also considered one of the heaviest stellar mass black holes, with a mass between 10 and 18 $M_\odot$. Remillard and McClintock make note that all of these black holes display a phenomenon known as the 3:2 ratio, where there is a roughly 3:2 ratio present in primary peaks of the changes in electron emission intensity. The primary explanation, though it is discredited by Remillard and McClintock, is that there is an Abramowicz hotspot around the black hole [4]. This is discredited because a hotspot would provide a fundamental frequency which would dominate over the harmonics, which provide the 3:2 ratio. This fundamental frequency has never been observed with this phenomenon. A hotspot is also a randomly generated bunch of material. It is unlikely that a hotspot would exist in every stellar mass black hole binary with enough density variation to produce the observed effects, especially given that hotspots deteriorate over time as they fall toward the black hole and become absorbed.

This 3:2 ratio is a calculated phenomenon, which is a result of the spacing between the most stable photon and graviton resonance states, and can be explained by the QNM oscillations, as is discussed in section 8.

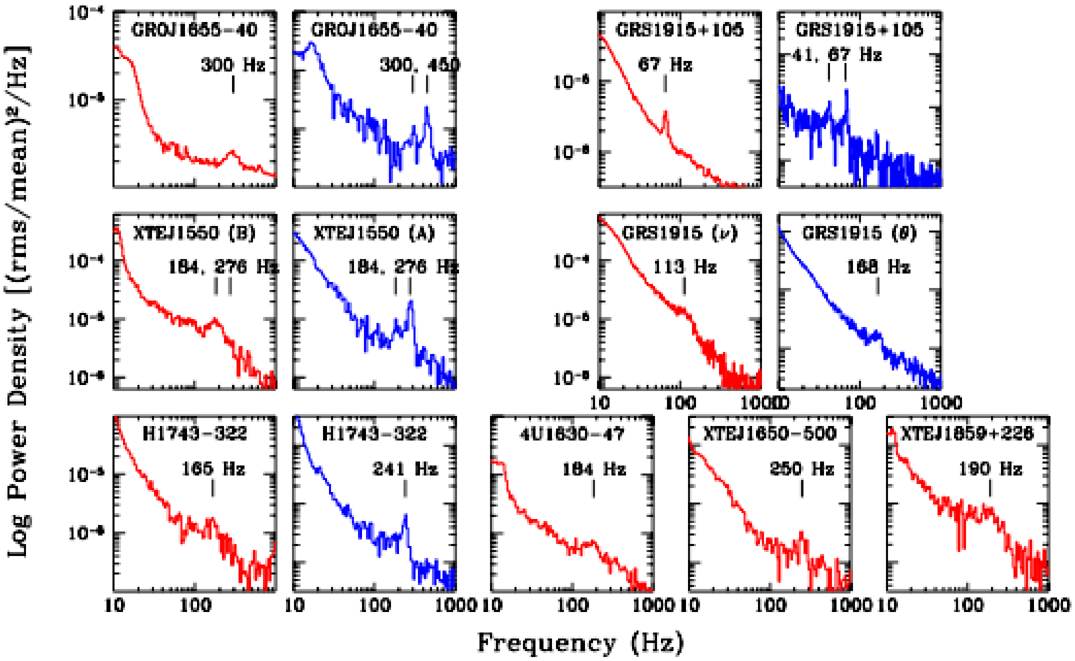

Figure 21: Fourier transforms of QPOs of stellar mass black holes in binaries. There is a near 3:2 ratio in peak frequency for the black hole of interest, GRS1915+105 of 113 and 168 Hz. This is well documented, though it has yet to be explained [4].

These Quasi-Periodic Oscillations (QPOs) are readily and easily observed for stellar mass black hole binaries. It is said that understanding these QPO oscillations will give an understanding for the spin of a black hole. [1]

Given that mathematically all Kerr black holes are the same and are only scaled by mass and spin, if a stellar mass black hole in a binary exhibits this behavior, it is reasonable for a supermassive black hole such as Sgr A* to exhibit the same behavior. This lends credibility to the calculations of the periods of the supermassive black hole Sgr A*.

Remillard and McClintock mention that this behavior is only observed in the three most studied stellar mass black hole binaries [4]. It is currently unknown why only these three black holes exhibit this behavior, but Bakala et al. [33] give a reasoning for this which agrees with our theory. The reasoning given by Bakala et al. is that the certain high spin black holes create a sufficiently high frequency QPO that current technology is unable to measure. This concurs with our theory, as the QPO frequencies for near maximally spinning prograde stellar mass black holes are higher than the frequencies currently observable. This indicates that the three main studied black holes, including GRS1915+105, have retrograde spin which makes their QPOs visible.

8 Results and Discussion

8.1 Supermassive Black Hole Sgr A* Results

In order to obtain self consistent solutions for the spin parameter for Sgr A*, the values of the bounds of the spin are determined by the lowest period for the graviton state and the highest period for the photon state which give the extremes of the spin values. These bounds are given from the periods of oscillation determined in section 7.1 to be 4.8 ± 0.1 min and 7.35 ± 0.1 min for graviton and photon resonances respectively. These bounds are then set when the graviton period is 4.70min and the photon period is set at 7.45 min. This is because the range of spin values the graviton resonance can give above 4.70 min contains all possible values up to the value of spin when the graviton resonance is at period 7.45 min. Similarly the photon resonance lower bound of 7.25 min exceeds the minimum value of spin given by the graviton resonance and therefore the constraining term on the lower bound is the graviton resonance term.

These terms set the bounds on a black hole of mass 4.02 $\times 10^6$ $M_\odot$ (as calculated by Bohele et al. [10] and shown in section 2.4.2) to be $a^* = 0.404 \pm 0.029$ in the $c = G = M = 1$ unit system, which is the standard convention for the spin parameter.

When considering the mass constraints given by Bohele et al. [10] of $\pm 0.2 \times 10^6$ $M_\odot$, the results for spin vary more greatly to $a^* = 0.371 \pm .147$. This radical increase in the error of the value is due to the strong mass dependency of the method. By decreasing the error in the mass estimate, the error in the spin estimate rapidly decreases.

Using the lower bound of Genzel et al. [32] given in section 2.4.2, the lower bound of the mass can be set at 3.97×10^6 $\mathrm{M}_\odot$. This instead gives a value for the spin to be $a^* = 0.431 \pm 0.075$. Using both of these constraints gives a better estimate for the overall mass of the black hole and narrows the range of possible spin values.

This gives a close resemblance to the previous calculation done by Kato et al. [16] which calculated a black hole spin of $a^* \approx 0.44$. The calculation method provided in this work is then validated by this other spin calculation method for the supermassive black hole Sgr A*.

Due to the strong dependence on the mass, as constraints on the mass become harsher, the constraints on the spin will be greatly reduced, giving a more accurate spin estimate. Likewise, if the periods of the QPOs are studied more closely for Sgr A*, the constraints on the angular frequency will become harsher and the limits on the spin will as well.

8.2 Stellar Mass Binary Black Hole GRS1915+105 Results

For GRS1915+105, with mass 10.1 ± 0.6 $\mathrm{M}_\odot$ as shown by Steeghs et al. [34], the values of the x-Ray shown in figure 21, show a prominent peak at 168 Hz and 113 Hz, which are understood to be the signals from the graviton and photon resonances respectively as the graviton resonance should provide a higher frequency oscillation. There is a notaible lower frequency oscillation for GRS1915+105 in figure 21 (at 67 and 41 Hz), but these frequencies are known to vary with luminosity [35] while the 168 and 113 Hz frequencies are not. This variation in frequency with luminosity indicates these frequencies are caused by another phenomenon, as the frequencies of the graviton and photon resonance states are not dependent on the luminosity. This gives a selection criterion for the proper QPO frequencies.

The variance on the mass (10.1 ± 0.6 $\mathrm{M}_{\odot}$ [34]) gives the spin of GRS1915+105 to be $a^{*} = -0.9888 \pm 0.0064$ which indicates a near maximum retrograde spin. The spin for GRS1915+105 is often calculated to be $a^{*} > 0.98$ [4] but direction is not indicated. This rapid spin is often seen by the enormous jet that GRS1915+105 produces, as it is considered a micro-quasar. This jet does not indicate direction of spin, only that it is actively accreting while rapidly spinning.

Considering the requirement for self consistency of the spin as estimated by the two resonant frequencies, the mass of GRS1915+105 can be calculated by setting the spin parameter, a^{*}, equal between the two resonance cavity equations and solving for the mass. This gives a mass estimate of $M = 10.09 \pm 0.005$ $\mathrm{M}_{\odot}$ for GRS1915+105, which is within the expected value of (10.1 ± 0.6) $\mathrm{M}_{\odot}$ given by Steeghs et al. [34]. This shows that for a well known QPO frequency, the solution method can provide both an estimate for the mass, and an estimate for the spin of the black hole. If the frequencies of the QPOs given by Remillard and McClintock [4]are accurate to three significant figures, there is no other solution using this method that gives consistency for the photon and graviton resonance frequencies other than $M = 10.09 \pm 0.005$ and $a^{*} = -0.9875 \pm 0.0005$.

9 Conclusions

The spin solutions produced in this work provide an accurate and easy to calculate method for determining the spin of a black hole. Since the base graphs have been generated already and trendlines created, the solution method for determining the black hole spin only requires the simple numerical solution of a polynomial function when the QPOs of the black hole are known. These black holes can be seen in the NIR and x-ray observations of the black hole, giving a solution for the spin based on the physical measurements from the black hole, which separates it from other black holes of its type.

The QPOs of a black hole's NIR and x-ray signal are created by the QNMs of standing wave gravitons and photons surrounding the black hole, below the ISCO. These standing wave resonances influence the bunching of electrons and create higher density regions around the black hole, which, due to the emission measure, produce a significantly increased signal. This change in electron emission is then seen as a fluctuating intensity, or QPO.

These QPOs are related to the QNMs as a unitless angular frequency and are then used to calculate the spin parameter, a^*. The supermassive black hole Sgr A* has QPOs with periods of 4.8 ± 0.1 min and 7.35 ± 0.1 min for the graviton and photon resonances respectively and this relates to a spin parameter, based on its mass, of $a^* = 0.431 \pm 0.077$. The error on this number can be significantly reduced by incorporating better estimates for the mass and QPO periods.

In the stellar mass case, GRS1915+105 was chosen to be observed due to its well known values for mass and spin. The spin was calculated using its mass of 10.1 ± 0.6 $M_{\odot}$, and QPO frequencies of 168 Hz and 113 Hz for the graviton and photon resonances respectively to be $a^* = -0.9888 \pm 0.0064$. If the self consistency of the photon and graviton resonances is considered and the QPO frequencies are taken to be accurate without error, the mass for GRS1915+105 can be calculated using this method to be $M = 10.09\text{M}_\odot$ which is within the error for the latest calculation of the mass, 10.1 ± 0.6 $\text{M}_\odot$ [34]. This shows that with accurate measurements of the QPO frequencies, the spin and mass can be calculated for black holes.

The continued fraction solution method for the QPOs of a black hole is a powerful and rapidly converging approximation method, which may apply to various other numerical solutions. In the case of black hole QPOs, this work provides the necessary solutions and linear regressions to not require the calculation of the continued fracitons for additional uses of this method when calculating spin. Since all black holes are equivalent when scaled by mass and spin, and mass is included in the calculation of the unitless angular frequency, these solution equations are valid for all Kerr black holes.

References

[1] C. Chan, “Oscillations of the inner regions of viscous accretion disks,” *Astrophysical Journal*, vol. 704, no. 1, pp. 68–79, 2009.

[2] R. Hulse and J. Taylor, “Discovery of pulsar in a binary system,” *Astrophysical Journal*, vol. 195, pp. L51–L53, 1975.

[3] B. Abbot, T. L. S. Collaboration, and V. Collaboration, “Observation of gravitational waves from binary black hole merger,” *Physical Review Letters*, vol. 116, no. 061 102, pp. 1–16, 2016.

[4] R. Remillard and J. McClintock, “X-ray properties of black hole binaries.,” *Annual Review of Astronomy and Astrophysics*, vol. 44, no. 1, pp. 49–92, 2006.

[5] B. Carroll and D. Ostilie, *Introduction to Modern Astrophysics (2nd Edition)*. Pearson Publishing, 2006.

[6] E. Taylor and J. Wheeler, *Exploring Black Holes.* Addison Wesley Longman, Inc., 2000.

[7] R. Narayan and I. Yi, “Advection-dominated accretion: Underfed black holes and neutron stars.,” *Astrophysical Journal*, vol. 452, pp. 710–735, 1995.

[8] C. Michel, “Intense coherent submillimeter radiation in electron storage rings,” *Physical Review Letters*, vol. 48, no. 9, pp. 580–583, 1982.

[9] F. Melia, *The Galactic Supermassive Black Hole.* Princeton University Press, 2007.

[10] A. Bohele, A. Ghez, R. Shödel, I. Meyer, S. Yelda, S. Albers, G. Martinez, E. Becklin, T. Do, J. Lu, K. Matthews, M. Morris, B. Sitarski, and G. Witzel, "An improved distance and mass estimate for Sgr A* from a multistar orbit analysis," *Astrophysical Journal*, vol. 830, no. 1, p. 17, 2016.

[11] S. Gillissen, P. Plewa, F. Eisenhauer, R. Sari, I. Waisberg, M. Habibi, O. Phuhl, E. George, J. Dexterm, S. von FellenBerg, T. Ott, and R. Genzel, "An update on monitoring stellar orbits in the galactic center," *Astrophysical Journal*, vol. 837, no. 1, p. 30, 2016.

[12] J. McClintock, R. Shafee, R. Narayan, R. Remillard, S. Davis, and L. Li., "The spin of the near-extreme Kerr black hole GRS1915," *Astrophysical Journal*, vol. 652, pp. 518–539, 2006.

[13] M. Abramowicz and W. Kluźniak, "A precise determination of black hole spin in GRO J1655-40," *Astronomy and Astrophysics*, vol. 374, no. 3, pp. L19–L20, 2001.

[14] V. Dokuchaev, "Spin and mass of the nearest supermassive black hole," *General Relativity and Gravitation*, vol. 46, no. 1832, 2014.

[15] Y. Iwata, T. Oka, and M. Miyoshi, "Possible detection of quasi-periodic oscillations from Sgr A* at 43GHz," *Preceedings of the International Astronomical Union*, vol. 11, no. S322, pp. 50–51, 2016.

[16] Y. Kato, M. Miyoshi, R. Takahashi, H. Negoro, and R. Matsumoto, "Measuring spin of a supermassive black hole at the galactic center - implications for a unique

spin," *Monthly Notices of the Royal Astronomical Society Letters*, vol. 403, no. 1, pp. L74–L78, 2010.

[17] C. Olds, *Continued Fractions.* New Mathematical Library Number 9, Mathematical Association of America, A 1992.

[18] R. Wald, *General Relativity.* The University of Chicago Press, 1984.

[19] G. Cook and M. Zalutskiy, "Gravitational perturbations of the Kerr geometry: high accuracy study," *Physical Review D: Particles and Fields*, vol. 90, no. 12, 2014.

[20] R. Boyer and R. Lindquist, "Maximal analytic extension of the Kerr metric," *Journal of Mathematical Physics*, vol. 8, pp. 265–281, 1967.

[21] S. Teukolsky, "Perturbations of a rotating black hole I. fundamental equations for gravitational, electromagnetic, and neutrino-field perturbations," *Astrophysical Journal*, vol. 185, pp. 635–647, 1973.

[22] S. Culbreth, "Graviton and photon orbitals surrounding a black hole. application to the supermassive black hole at the milky galactic center, with NIR observational confirmation.," Master's thesis, East Carolina University, 2013.

[23] S. Chandrasekhar and S. Detweiler, "On the equations governing the gravitational perturbations of the Kerr black hole," *Proceedings of the Royal Society of London, Series A, Mathematical and Physical Sciences*, vol. 350, no. 1661, pp. 165–174, 1976.

[24] G. Kaniadakis and P. Quarati, “Classical model of bosons and fermions,” *Physical Review E: Statistical Physics, Plasmas, Fluids, and Related Interdisciplinary Topics*, vol. 49, no. 6, pp. 5103–5110, 1994.

[25] S. Crothers, “On the Regge-Wheeler tortoise and the Kruskal-Szekeres coordinates.,” *Reports on Progress in Physics*, no. 3, pp. 30–34, 2006.

[26] W. Salmon, ed., *Zeno's Paradoxes.* Hackett Publishing Company, Inc., 2001.

[27] N. Fröman, P. Fröman, N. Andersson, and A. Höback, “Black hole normal modes: Phase-integral treatment,” *The American Physical Journal Physical Review D*, vol. 45, pp. 2609–2616, 1992.

[28] E. Leaver, *Solutions to a generalized spheroidal wave equation in molecular physics and general relativity: and an analysis of the Quasi-normal modes of Kerr black holes.* PhD thesis, University of Utah, 1985.

[29] S. Teukolsky, “Rotating black holes: Separable wave equations for gravitational and electromagnetic perturbations,” *Physical Review Letters*, vol. 29, no. 16, p. 1114, 1972.

[30] W. Baber and H. Hassé, “The two center problem in wave mechanics,” *Mathematical Proceedings of the Cambridge Philosophical Society*, vol. 25, no. 31, pp. 564–581, 1935.

[31] W. R. Inc., *Mathematica, Version 10.4.* Champaign, IL, 2017.

[32] R. Genzel, R. Shödel, T. Ott, A. Eckart, T. Alexander, F. Lacombe, D. Rouan, and B. Aschenbach, "Near-infrared flares from accreting gas around the supermassive black hole at the galactic centre," *Nature*, vol. 425, pp. 934–937, 2003.

[33] P. Bakala, K. Goluchová, G. Török, E. Šrámková, M. Abramowicz, F. Vincent, and G. Mazur, "Twin peak HF QPOs as a spectral imprint of dual oscillation modes of accretion tori," *Astronomy and Astrophysics*, vol. 581, 2015. id. A35,12.

[34] D. Steeghs, J. McClintock, S. Parsons, M. Reid, S. Littlefair, and V. Dhillion, "The not-so-massive black hole in the microquasar GRS1915+105," *Astrophysical Journal*, vol. 768, no. 185, p. 7pp, 2013.

[35] W. Lewin and M. van der Klis, eds., *Compact Stellar X-Ray Sources*. Cambridge University Press, 2006.

Appendices

A Additional Perturbation Calculation Tables

The following tables are intended to further the understanding of the perturbation method used by S. Culbreth [22] when calculating the energy levels of the various states of the photon and graviton resonances.

Table 13: $E_n^{(0)}$ terms for perturbation theory corrections for harmonic oscillator wave functions in the harmonic oscillator potential for gravitons in the state L=3.

Harmonic Oscillator Eigenvalue	Numerical Calculation
$E_0^{(0)}$	.0531
$E_1^{(0)}$	.159
$E_2^{(0)}$	.266
$E_3^{(0)}$	.372
$E_4^{(0)}$	.478
$E_5^{(0)}$	.585
$E_6^{(0)}$	.691

Table 14: $E_n^{(0)}$ terms for perturbation theory corrections for harmonic oscillator wave functions in the harmonic oscillator potential for gravitons in the state L=4.

Harmonic Oscillator Eigenvalue	Numerical Calculation
$E_0^{(0)}$	.0591
$E_1^{(0)}$	.177
$E_2^{(0)}$	.295
$E_3^{(0)}$	.414
$E_4^{(0)}$	.532
$E_5^{(0)}$	.651
$E_6^{(0)}$	.769

Table 15: $E_n^{(0)}$ terms for perturbation theory corrections for harmonic oscillator wave functions in the harmonic oscillator potential for photons in the state L=1.

Harmonic Oscillator Eigenvalue	Numerical Calculation
$E_0^{(0)}$	.0355
$E_1^{(0)}$	.106
$E_2^{(0)}$	.177
$E_3^{(0)}$	.248
$E_4^{(0)}$	.319
$E_5^{(0)}$	.390
$E_6^{(0)}$	.461

Table 16: $E_n^{(0)}$ terms for perturbation theory corrections for harmonic oscillator wave functions in the harmonic oscillator potential for photons in the state L=2.

Harmonic Oscillator Eigenvalue	Numerical Calculation
$E_0^{(0)}$	.0467
$E_1^{(0)}$	.140
$E_2^{(0)}$	.234
$E_3^{(0)}$	.366
$E_4^{(0)}$	.420
$E_5^{(0)}$	.513
$E_6^{(0)}$	.607

Table 17: $E_n^{(0)}$ terms for perturbation theory corrections for harmonic oscillator wave functions in the harmonic oscillator potential for photons in the state L=3.

Harmonic Oscillator Eigenvalue	Numerical Calculation
$E_0^{(0)}$	.0555
$E_1^{(0)}$	.167
$E_2^{(0)}$	.278
$E_3^{(0)}$	.389
$E_4^{(0)}$	.500
$E_5^{(0)}$	.611
$E_6^{(0)}$	.722

Table 18: dV_{nm} terms for perturbation theory for various combinations of wave functions and difference between the harmonic oscillator and our calculated potential for gravitons in the L=3 state.

Wave Function	$\|U_0>$	$\|U_1>$	$\|U_2>$	$\|U_3>$	$\|U_4>$	$\|U_5>$	$\|U_6>$
$<U_0\|$	-.00967	-.0238	-.0242	-.00321	-.00941	.00204	.00223
$<U_1\|$	-.0238	-.0439	-.0392	-.0607	-.00186	-.0156	.00261
$<U_2\|$	-.0242	-.0392	-.101	-.0484	-.104	.000126	-.0207
$<U_3\|$	-.00321	-.0607	-.0484	-.171	.0542	-.151	.00225
$<U_4\|$	-.00941	-.00186	-.104	.0542	.250	-.0580	-.200
$<U_5\|$	.00204	-.0156	.000126	-.151	-.0580	-.334	-.0604
$<U_6\|$	.00223	.00261	-.0207	.00225	-.200	-.0604	-.421

Table 19: dV_{nm} terms for perturbation theory for various combinations of wave functions and difference between the harmonic oscillator and our calculated potential for gravitons in the L=4 state.

Wave Function	$\|U_0>$	$\|U_1>$	$\|U_2>$	$\|U_3>$	$\|U_4>$	$\|U_5>$	$\|U_6>$
$<U_0\|$	-.00836	-.00896	-.0219	-.00889	-.00965	.00361	.00181
$<U_1\|$	-.00896	-.0393	-.0281	-.0574	-.0103	-.0169	.00553
$<U_2\|$	-.0219	-.0281	-.0948	-.0400	-.101	-.0938	-.0236
$<U_3\|$	-.00889	-.0574	-.0400	-.165	-.0498	-.150	.00760
$<U_4\|$	-.00965	-.0103	-.101	-.0498	-.245	-.0569	-.202
$<U_5\|$	.00361	-.0169	-.0938	-.150	-.0569	-.332	-.0621
$<U_6\|$	.00181	.00553	-.0236	-.00760	-.202	-.0621	-.424

Table 20: dV_{nm} terms for perturbation theory for various combinations of wave functions and difference between the harmonic oscillator and our calculated potential for photons in the L=1 state.

Wave Function	$\|U_0>$	$\|U_1>$	$\|U_2>$	$\|U_3>$	$\|U_4>$	$\|U_5>$	$\|U_6>$
$<U_0\|$	-.00836	-.00896	-.0219	-.00889	-.00965	.00361	.00181
$<U_1\|$	-.00896	-.0393	-.0281	-.0574	-.0103	-.0169	.00553
$<U_2\|$	-.0219	-.0281	-.0948	-.0400	-.101	-.0938	-.0236
$<U_3\|$	-.00889	-.0574	-.0400	-.165	-.0498	-.150	.00760
$<U_4\|$	-.00965	-.0103	-.101	-.0498	-.245	-.0569	-.202
$<U_5\|$	.00361	-.0169	-.0938	-.150	-.0569	-.332	-.0621
$<U_6\|$	.00181	.00553	-.0236	-.00760	-.202	-.0621	-.424

Table 21: dV_{nm} terms for perturbation theory for various combinations of wave functions and difference between the harmonic oscillator and our calculated potential for photons in the L=2 state.

Wave Function	$\|U_0>$	$\|U_1>$	$\|U_2>$	$\|U_3>$	$\|U_4>$	$\|U_5>$	$\|U_6>$
$<U_0\|$	-.00836	-.00896	-.0219	-.00889	-.00965	.00361	.00181
$<U_1\|$	-.00896	-.0393	-.0281	-.0574	-.0103	-.0169	.00553
$<U_2\|$	-.0219	-.0281	-.0948	-.0400	-.101	-.0938	-.0236
$<U_3\|$	-.00889	-.0574	-.0400	-.165	-.0498	-.150	.00760
$<U_4\|$	-.00965	-.0103	-.101	-.0498	-.245	-.0569	-.202
$<U_5\|$	.00361	-.0169	-.0938	-.150	-.0569	-.332	-.0621
$<U_6\|$	.00181	.00553	-.0236	-.00760	-.202	-.0621	-.424

Table 22: dV_{nm} terms for perturbation theory for various combinations of wave functions and difference between the harmonic oscillator and our calculated potential for photons in the L=3 state.

Wave Function	$\|U_0>$	$\|U_1>$	$\|U_2>$	$\|U_3>$	$\|U_4>$	$\|U_5>$	$\|U_6>$
$<U_0\|$	-.00836	-.00896	-.0219	-.00889	-.00965	.00361	.00181
$<U_1\|$	-.00896	-.0393	-.0281	-.0574	-.0103	-.0169	.00553
$<U_2\|$	-.0219	-.0281	-.0948	-.0400	-.101	-.0938	-.0236
$<U_3\|$	-.00889	-.0574	-.0400	-.165	-.0498	-.150	.00760
$<U_4\|$	-.00965	-.0103	-.101	-.0498	-.245	-.0569	-.202
$<U_5\|$	.00361	-.0169	-.0938	-.150	-.0569	-.332	-.0621
$<U_6\|$	.00181	.00553	-.0236	-.00760	-.202	-.0621	-.424

B Mathematica Code for the Solution of a System of Continued Fractions

The following Mathematica [31] coding was used to caluclate the solutions for the Teukolsky equation using the Continued Fraction method, regression equations based on those solutions, and values for the spin and mass of both supermassive and stellar mass black holes based on observational data from Sgr A* and GRS1915+105.

```
ClearAll[k1, k2, αθ, βθ, γθ, Contθ]

k1[m_, s_] := 1/2 * Abs[m - s];
k2[m_, s_] := 1/2 * Abs[m + s];
αθ[m_, s_, n_] := -2 (n + 1) (n + 2 * k1[m, s] + 1);
βθ[m_, s_, n_] := n (n - 1) + 2 * n (k1[m, s] + k2[m, s] + 1 - 2 * a * ω) -
    (2 * a * ω (2 * k1[m, s] + s + 1) - (k1[m, s] + k2[m, s]) (k1[m, s] + k2[m, s] + 1)) -
    (a^2 * ω^2 + s (s + 1) + Alm);
γθ[m_, s_, n_] := 2 * a * ω (n + k1[m, s] + k2[m, s] + s);
Contθ[m_, s_, nmax_] := βθ[m, s, 0] +
  ContinuedFractionK[-αθ[m, s, n] * γθ[m, s, n + 1], βθ[m, s, n + 1], {n, 0, nmax}]

ClearAll[b, c1, c2, c3, c4, αr, βr, γr, Contr]

b[a_] := Sqrt[1 - 4 a^2]
c0[m_, s_] := 1 - s - ⅈ * ω - (2 ⅈ)/(b[a]) (ω/2 - a * m)
c1[m_, s_] := -4 + 2 ⅈ * ω (2 + b[a]) + (4 ⅈ)/(b[a]) (ω/2 - a * m)
c2[m_, s_] := s + 3 - 3 ⅈ * ω - (2 ⅈ)/(b[a]) (ω/2 - a * m)
c3[m_, s_] :=
 ω^2 (4 + 2 b[a] - a^2) - 2 a * m * ω - s - 1 + (2 + b[a]) * ⅈ * ω - Alm + (4 ω + 2 ⅈ)/(b[a]) (ω/2 - a * m)
c4[m_, s_] := s + 1 - 2 ω^2 - (2 s + 3) * ⅈ * ω - (4 ω + 2 ⅈ)/(b[a]) (ω/2 - a * m)
αr[m_, s_, n_] := b[a] * (n^2 + (c0[m, s] + 1) n + c0[m, s]);
βr[m_, s_, n_] := b[a] * (-2 n^2 + (c1[m, s] + 2) n + c3[m, s]);
γr[m_, s_, n_] := b[a] * (n^2 + (c2[m, s] - 3) n + c4[m, s] - c2[m, s] + 2);
Contr[m_, s_, nmax_] := βr[m, s, 0] +
  ContinuedFractionK[-αr[m, s, n] * γr[m, s, n + 1], βr[m, s, n + 1], {n, 0, nmax}]

OmegaSolve[m_, s_, nmax_, A_] := NSolve[{Contr[m, s, nmax] == 0 /. a → A,
   Contθ[m, s, nmax] == 0 /. a → A, 0 <= Re[Alm] ≤ (-2 * s)}, {ω, Alm}]

OmegaSolveRetro[m_, s_, nmax_, A_] := NSolve[{Contr[m, s, nmax] == 0 /. a → A,
   Contθ[m, s, nmax] == 0 /. a → A, (-3 * s) >= Re[Alm] >= (-2 * s)}, {ω, Alm}]

OmegaFrequency[f_, Mass_] := ((4 * Pi * f * 6.674 * 10^(-11) * Mass * 1.989 * 10^30)/((2.997 * 10^8)^3))

OmegaPeriod[t_, Mass_] :=
 ((4 * Pi * (1/(60 t)) * 6.674 * 10^(-11) * Mass * 1.99 * 10^30) / (2.99 * 10^8)^3)
```

```
ProgradeGravData =
  {{0, 0.7467}, {0.025, 0.759522}, {0.05, 0.773405}, {0.075, 0.788065},
   {0.1, 0.803831}, {0.125, 0.820635}, {0.15, 0.83871}, {0.175, 0.858211},
   {0.2, 0.879416}, {0.225, 0.902543}, {0.25, 0.927992}, {0.275, 0.956266},
   {0.3, 0.9878}, {0.325, 1.02375}, {0.35, 1.065}, {0.375, 1.11341}, {0.4, 1.17179},
   {0.425, 1.24494}, {0.45, 1.342266}, {0.475, 1.49082}, {0.4999, 1.91283}};
```

```
ProgradeGravFit = Fit[ProgradeGravData, {1, a^3, a^4, a^5, a^6, a^7}, a]
```

$$0.753992 + 161.815\,a^{3} - 1704.27\,a^{4} + 7231.43\,a^{5} - 13\,803.4\,a^{6} + 9873.49\,a^{7}$$

```
ProLeaverGravSolve[w_] := NSolve[{w == ProgradeGravFit, Im[a] == 0, a > 0}, a];
ProNormalGravSolve[w_] :=
  NSolve[{w == 0.7539916586895395` + 161.81507772877058` (0.5 a)^3 -
      1704.268782577845` (0.5 a)^4 + 7231.434859887723` (0.5 a)^5 -
      13803.44707011829` (0.5 a)^6 + 9873.487259870546` (0.5 a)^7, Im[a] == 0, a > 0}, a];
```

```
ProgradePhotData = {{0, 0.498103}, {0.025, 0.504587},
   {0.05, 0.51165}, {0.075, 0.519157}, {0.1, 0.52722}, {0.125, 0.535741},
   {0.15, 0.544862}, {0.175, 0.554665}, {0.2, 0.565244}, {0.225, 0.576704},
   {0.25, 0.589054}, {0.275, 0.60294}, {0.3, 0.618137}, {0.325, 0.635137},
   {0.35, 0.654404}, {0.375, 0.676616}, {0.4, 0.702838}, {0.425, 0.734858},
   {0.45, 0.775848}, {0.475, 0.835966}, {0.4999, 0.964367}};
```

```
ProgradePhotFit = Fit[ProgradePhotData, {1, a^3, a^4, a^5, a^6, a^7}, a]
```

$$0.503623 + 62.3338\,a^{3} - 602.75\,a^{4} + 2407.49\,a^{5} - 4391.5\,a^{6} + 3036.52\,a^{7}$$

```
ProLeaverPhotSolve[w_] := NSolve[{w == ProgradePhotFit, Im[a] == 0, a > 0}, a];
ProNormalPhotSolve[w_] :=
  NSolve[{w == 0.503622771939244` + 62.333813287027915` (0.5 a)^3 -
      602.75001383744` (0.5 a)^4 + 2407.490737456206` (0.5 a)^5 -
      4391.497982187425` (0.5 a)^6 + 3036.524360721154` (0.5 a)^7, Im[a] == 0, a > 0}, a];
```

```
retrogradeData = {{0, 0.7467}, {0.025, 0.734156},
   {0.05, 0.72232}, {0.075, 0.711119}, {0.1, 0.700562}, {0.125, 0.6901823},
   {0.15, 0.680265}, {0.175, 0.670823}, {0.2, 0.661543}, {0.225, 0.652311},
   {0.25, 0.643229}, {0.275, 0.634176}, {0.3, 0.624929}, {0.325, 0.615312},
   {0.35, 0.60481}, {0.375, 0.592865}, {0.4, 0.578144}, {0.425, 0.557768},
   {0.45, 0.525857}, {0.475, 0.461797}, {0.4999, 0.0716654}};
```

```
RetroGravFit = Fit[retrogradeData, {1, a^2, a^3, a^4, a^5, a^6, a^7, a^8}, a]
```

$$0.750033 - 42.104\,a^{2} + 922.524\,a^{3} - 8925.12\,a^{4} + 45\,012.1\,a^{5} - 123\,042.\,a^{6} + 172\,750.\,a^{7} - 97\,625.9\,a^{8}$$

```
RetroLeaverGravSolve[w_] := NSolve[{w == RetroGravFit, Im[a] == 0, a > 0}, a];
RetroNormalGravSolve[w_] :=
  NSolve[{w == 0.7500326375139046` - 42.10398448915728` (0.5 a)^2 +
      922.5236396406078` (0.5 a)^3 - 8925.117673339491` (0.5 a)^4 +
      45012.09101799327` (0.5 a)^5 - 123041.83720358968` (0.5 a)^6 +
      172749.6352801519` (0.5 a)^7 - 97625.85927214101` (0.5 a)^8, Im[a] == 0, a > 0}, a];
```

```
retrogradePhotData = {{0, 0.498103}, {0.025, 0.491602},
   {0.05, 0.485604}, {0.075, 0.479912}, {0.1, 0.474608}, {0.125, 0.469439},
   {0.15, 0.46453}, {0.175, 0.459835}, {0.2, 0.455358}, {0.225, 0.45101},
   {0.25, 0.446826}, {0.275, 0.442751}, {0.3, 0.438748}, {0.325, 0.43471},
   {0.35, 0.430532}, {0.375, 0.425989}, {0.4, 0.420635}, {0.425, 0.413494},
   {0.45, 0.401719}, {0.475, 0.374743}, {0.4999, 0.00817686}};
```

```
photretrofit = Fit[retrogradePhotData, {1, a^2, a^3, a^4, a^5, a^6, a^7, a^8}, a]
0.503433 - 37.407 a^2 + 899.149 a^3 - 9063.91 a^4 +
 46748.8 a^5 - 129507. a^6 + 183312. a^7 - 104067. a^8
```

```
RetroLeaverPhotSolve[w_] := NSolve[{w == photretrofit, Im[a] == 0, a > 0}, a];
RetroNormalPhotSolve[w_] :=
  NSolve[{w == 0.5034326322131738` - 37.40696615833125` (0.5 a)^2 +
      899.1494051721885` (0.5 a)^3 - 9063.913725004471` (0.5 a)^4 +
      46748.798593545456` (0.5 a)^5 - 129507.42211401962` (0.5 a)^6 +
      183312.3608807261` (0.5 a)^7 - 104067.3866033424` (0.5 a)^8, Im[a] == 0, a > 0}, a];
```

```
ProPeriodSolve[g_, p_, m_] :=
 {ProNormalGravSolve[OmegaPeriod[g, m]], ProNormalPhotSolve[OmegaPeriod[p, m]]}
```

```
ProFreqSolve[g_, p_, m_] := {ProNormalGravSolve[OmegaFrequency[g, m]],
  ProNormalPhotSolve[OmegaFrequency[p, m]]}
```

```
RetroPeriodSolve[g_, p_, m_] :=
 {RetroNormalGravSolve[OmegaPeriod[g, m]], RetroNormalPhotSolve[OmegaPeriod[p, m]]}
```

```
RetroFreqSolve[g_, p_, m_] := {RetroNormalGravSolve[OmegaFrequency[g, m]],
  RetroNormalPhotSolve[OmegaFrequency[p, m]]}
```

```
MassSolve[g_, p_] :=
 NSolve[{OmegaFrequency[p, 2 m] == 0.5034326322131738` - 37.40696615833125` (0.5 a)^2 +
     899.1494051721885` (0.5 a)^3 - 9063.913725004471` (0.5 a)^4 +
     46748.798593545456` (0.5 a)^5 - 129507.42211401962` (0.5 a)^6 +
     183312.3608807261` (0.5 a)^7 - 104067.3866033424` (0.5 a)^8,
   OmegaFrequency[g, 2 m] == 0.7500326375139046` - 42.10398448915728` (0.5 a)^2 +
     922.5236396406078` (0.5 a)^3 - 8925.117673339491` (0.5 a)^4 +
     45012.09101799327` (0.5 a)^5 - 123041.83720358968` (0.5 a)^6 + 172749.6352801519`
      (0.5 a)^7 - 97625.85927214101` (0.5 a)^8, Im[a] == 0, a > 0}, {a, m}]
```

C Linear Regression Significance Tables

Table 23: Statistics for the linear regression coefficient terms for a graviton ($l = -m = 2$) near a prograde spinning black hole. $R^2 = 0.99865$

	Estimate	Standard Error	t-Statistic	P-Value
1	0.753992	0.00667147	113.017	$2.12 \times 10^{-}23$
a^3	1610815	23.4112	6.91187	$4.96 \times 10^{-}6$
a^4	-1704.27	263.134	-6.4768	$1.04 \times 10^{-}5$
a^5	7231.43	1101.63	6.56433	$8.97 \times 10^{-}6$
a^6	-13803.4	2017.71	-6.84114	$5.59 \times 10^{-}6$
a^7	9873.49	1361.13	7.2539	$2.81 \times 10^{-}6$

Table 24: Statistics for the linear regression coefficient terms for a graviton ($l = -m = 1$) near a prograde spinning black hole. $R^2 = 0.999542$.

	Estimate	Standard Error	t-Statistic	P-Value
1	0.503626	0.00164049	306.996	$6.60 \times 10^{-}30$
a^3	62.3338	5.75672	10.828	$1.74 \times 10^{-}8$
a^4	-602.75	64.7036	-9.31555	$1.26 \times 10^{-}7$
a^5	2407.49	270.885	8.88749	$2.30 \times 10^{-}7$
a^6	-4391.5	496.147	-8.8512	$2.43 \times 10^{-}7$
a^7	3036.52	334.696	9.07249	$1.77 \times 10^{-}7$

Table 25: Statistics for the linear regression coefficient terms for a graviton ($l = -m = 2$) near a retrograde spinning black hole. $R^2 = 0.996823$.

	Estimate	Standard Error	t-Statistic	P-Value
1	0.750033	0.00815877	91.9296	$1.12 \times 10^{-}19$
a^2	-42.104	12.1885	-3.4544	0.00427
a^3	922.524	267.403	3.44993	0.00431
a^4	-8925.12	267.403	-3.70868	0.00263
a^5	45012.1	11140.7	4.04031	0.00140
a^6	-123042	27919.3	-4.40706	0.000708
a^7	172750	35997.3	4.479896	0.000347491
a^8	-97625.9	18718.9	-5.21535	0.000167

Table 26: Statistics for the linear regression coefficient terms for a graviton ($l = -m = 1$) near a retrograde spinning black hole. $R^2 = 0.991043$.

	Estimate	Standard Error	t-Statistic	P-Value
1	0.503433	0.00965439	52.1455	$1.74 \times 10^{-}16$
a^2	-37.407	14.4228	-2.59359	0.0223
a^3	899.149	316.422	2.84161	0.0138
a^4	-9063.91	2847.71	-3.18288	0.00720
a^5	46748.8	13183	3.54614	0.00358
a^6	-129507	33037.3	-3.92004	0.00176
a^7	183312	42596.2	4.30349	0.000858
a^8	-104067	22150.4	-4.69822	0.00041

D Rights and Permissions

All images in this work were created for this work, exist in a public domain setting with credits for images given if able, contain a clause stating use of material in a thesis/dissertation is allowed without permission, or have the expressed permission of those holding the copyright. The following documents show legal permission for images not in the public domain.

Copyright Clearance Center

Note: Copyright.com supplies permissions but not the copyrighted content itself.

1 PAYMENT 2 REVIEW 3 CONFIRMATION

Step 3: Order Confirmation

Thank you for your order! A confirmation for your order will be sent to your account email address. If you have questions about your order, you can call us 24 hrs/day, M-F at +1.855.239.3415 Toll Free, or write to us at info@copyright.com. This is not an invoice.

Confirmation Number: 11682340
Order Date: 11/20/2017

If you paid by credit card, your order will be finalized and your card will be charged within 24 hours. If you choose to be invoiced, you can change or cancel your order until the invoice is generated.

Payment Information

Shawn Culbreth
culbreths11@students.ecu.edu
+1 (267) 221-9300
Payment Method: CC ending in 2017

Order Details

Proceedings of the Royal Society of London. Series A, Containing papers of a mathematical and physical character

Order detail ID:	70799444
Order License Id:	4233190586582
ISSN:	0080-4630
Publication Type:	Journal
Volume:	
Issue:	
Start page:	
Publisher:	HARRISON AND SON,
Author/Editor:	ROYAL SOCIETY (GREAT BRITAIN)

Permission Status: ✓ **Granted**

Permission type: Republish or display content
Type of use: Republish in a thesis/dissertation

Requestor type	Academic institution
Format	Print, Electronic
Portion	image/photo
Number of images/photos requested	1
The requesting person/organization	Shawn Culbreth
Title or numeric reference of the portion(s)	Figure 1
Title of the article or chapter the portion is from	On the Equations Governing the Gravitational Perturbations of the Kerr Black Hole

Editor of portion(s)	N/A
Author of portion(s)	S. Chandrasekhar and S. Detweiler
Volume of serial or monograph	350
Issue, if republishing an article from a serial	1661
Page range of portion	170
Publication date of portion	Aug. 20, 1976
Rights for	Main product
Duration of use	Life of current edition
Creation of copies for the disabled	no
With minor editing privileges	no
For distribution to	United States
In the following language(s)	Original language of publication
With incidental promotional use	no
Lifetime unit quantity of new product	Up to 499
Title	A solution method determining the effect of spin upon gravitational effects in the surroundings of a black hole.
Instructor name	Orville Day
Institution name	East Carolina University
Expected presentation date	Dec 2017

Note: This item will be invoiced or charged separately through CCC's **RightsLink** service. More info **$ 48.50**

This is not an invoice.

Total order items: 1

Order Total: 48.50 USD

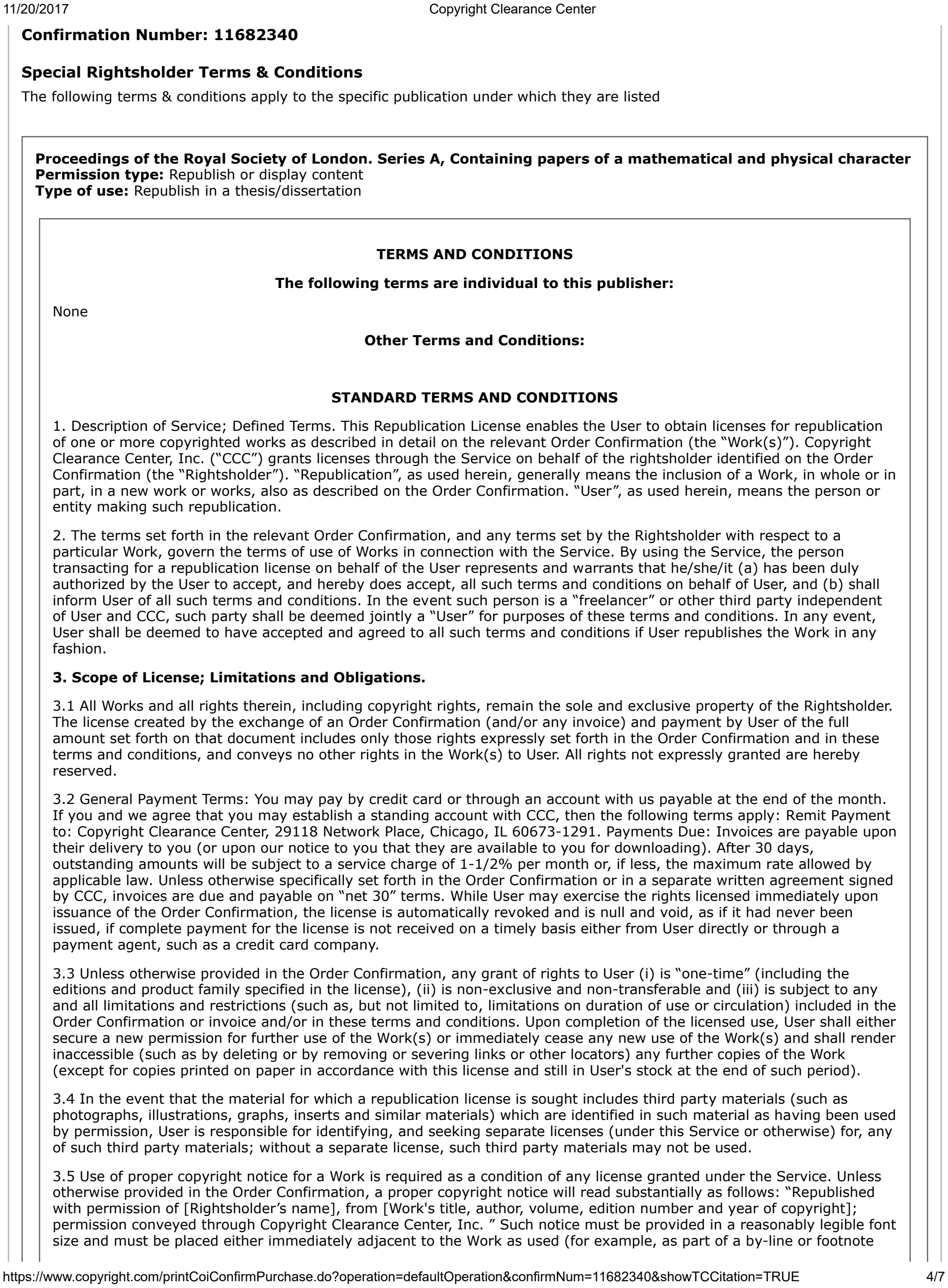

Confirmation Number: 11682340

Special Rightsholder Terms & Conditions

The following terms & conditions apply to the specific publication under which they are listed

Proceedings of the Royal Society of London. Series A, Containing papers of a mathematical and physical character
Permission type: Republish or display content
Type of use: Republish in a thesis/dissertation

TERMS AND CONDITIONS

The following terms are individual to this publisher:

None

Other Terms and Conditions:

STANDARD TERMS AND CONDITIONS

1. Description of Service; Defined Terms. This Republication License enables the User to obtain licenses for republication of one or more copyrighted works as described in detail on the relevant Order Confirmation (the "Work(s)"). Copyright Clearance Center, Inc. ("CCC") grants licenses through the Service on behalf of the rightsholder identified on the Order Confirmation (the "Rightsholder"). "Republication", as used herein, generally means the inclusion of a Work, in whole or in part, in a new work or works, also as described on the Order Confirmation. "User", as used herein, means the person or entity making such republication.

2. The terms set forth in the relevant Order Confirmation, and any terms set by the Rightsholder with respect to a particular Work, govern the terms of use of Works in connection with the Service. By using the Service, the person transacting for a republication license on behalf of the User represents and warrants that he/she/it (a) has been duly authorized by the User to accept, and hereby does accept, all such terms and conditions on behalf of User, and (b) shall inform User of all such terms and conditions. In the event such person is a "freelancer" or other third party independent of User and CCC, such party shall be deemed jointly a "User" for purposes of these terms and conditions. In any event, User shall be deemed to have accepted and agreed to all such terms and conditions if User republishes the Work in any fashion.

3. Scope of License; Limitations and Obligations.

3.1 All Works and all rights therein, including copyright rights, remain the sole and exclusive property of the Rightsholder. The license created by the exchange of an Order Confirmation (and/or any invoice) and payment by User of the full amount set forth on that document includes only those rights expressly set forth in the Order Confirmation and in these terms and conditions, and conveys no other rights in the Work(s) to User. All rights not expressly granted are hereby reserved.

3.2 General Payment Terms: You may pay by credit card or through an account with us payable at the end of the month. If you and we agree that you may establish a standing account with CCC, then the following terms apply: Remit Payment to: Copyright Clearance Center, 29118 Network Place, Chicago, IL 60673-1291. Payments Due: Invoices are payable upon their delivery to you (or upon our notice to you that they are available to you for downloading). After 30 days, outstanding amounts will be subject to a service charge of 1-1/2% per month or, if less, the maximum rate allowed by applicable law. Unless otherwise specifically set forth in the Order Confirmation or in a separate written agreement signed by CCC, invoices are due and payable on "net 30" terms. While User may exercise the rights licensed immediately upon issuance of the Order Confirmation, the license is automatically revoked and is null and void, as if it had never been issued, if complete payment for the license is not received on a timely basis either from User directly or through a payment agent, such as a credit card company.

3.3 Unless otherwise provided in the Order Confirmation, any grant of rights to User (i) is "one-time" (including the editions and product family specified in the license), (ii) is non-exclusive and non-transferable and (iii) is subject to any and all limitations and restrictions (such as, but not limited to, limitations on duration of use or circulation) included in the Order Confirmation or invoice and/or in these terms and conditions. Upon completion of the licensed use, User shall either secure a new permission for further use of the Work(s) or immediately cease any new use of the Work(s) and shall render inaccessible (such as by deleting or by removing or severing links or other locators) any further copies of the Work (except for copies printed on paper in accordance with this license and still in User's stock at the end of such period).

3.4 In the event that the material for which a republication license is sought includes third party materials (such as photographs, illustrations, graphs, inserts and similar materials) which are identified in such material as having been used by permission, User is responsible for identifying, and seeking separate licenses (under this Service or otherwise) for, any of such third party materials; without a separate license, such third party materials may not be used.

3.5 Use of proper copyright notice for a Work is required as a condition of any license granted under the Service. Unless otherwise provided in the Order Confirmation, a proper copyright notice will read substantially as follows: "Republished with permission of [Rightsholder's name], from [Work's title, author, volume, edition number and year of copyright]; permission conveyed through Copyright Clearance Center, Inc. " Such notice must be provided in a reasonably legible font size and must be placed either immediately adjacent to the Work as used (for example, as part of a by-line or footnote

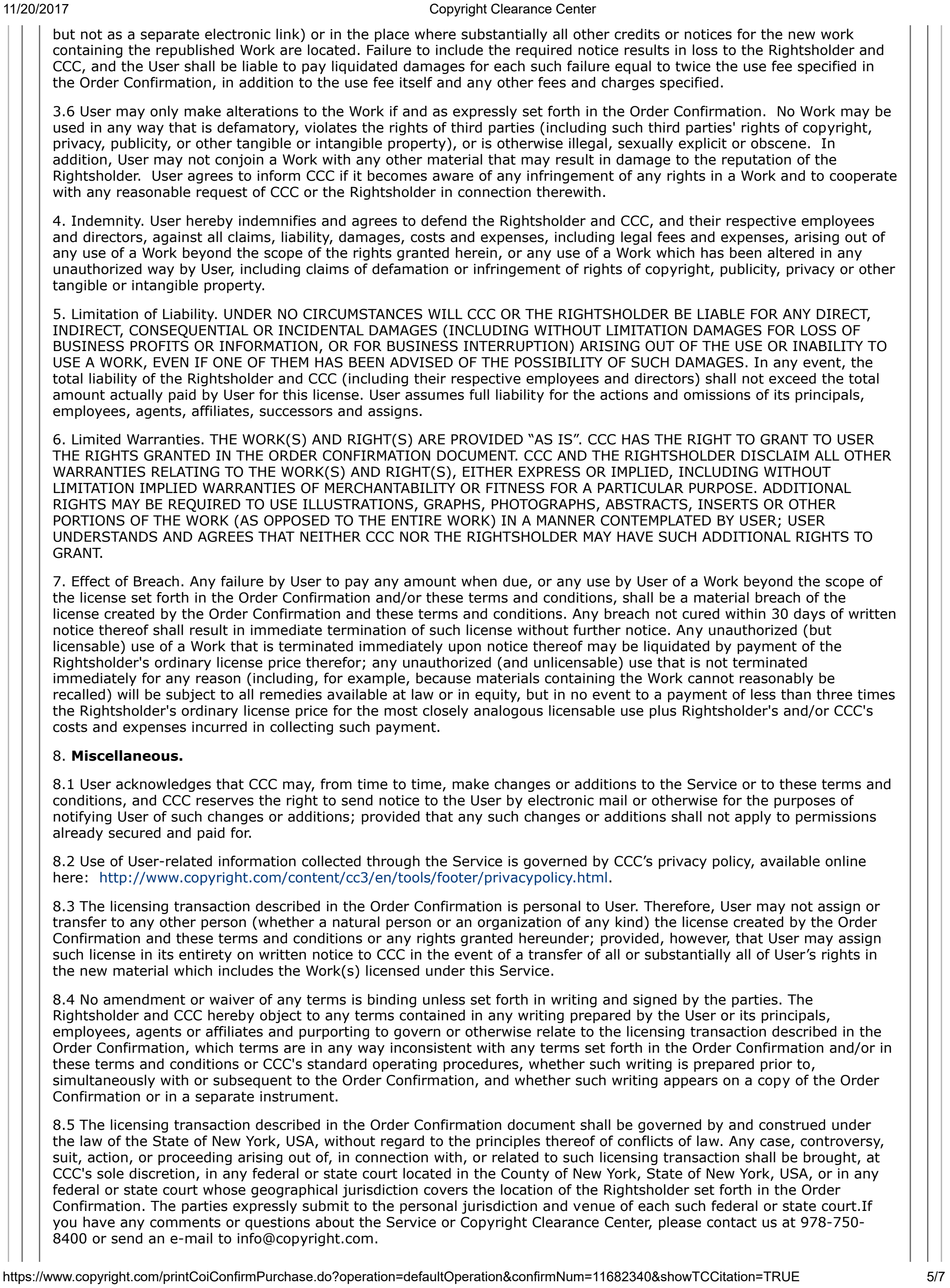

but not as a separate electronic link) or in the place where substantially all other credits or notices for the new work containing the republished Work are located. Failure to include the required notice results in loss to the Rightsholder and CCC, and the User shall be liable to pay liquidated damages for each such failure equal to twice the use fee specified in the Order Confirmation, in addition to the use fee itself and any other fees and charges specified.

3.6 User may only make alterations to the Work if and as expressly set forth in the Order Confirmation. No Work may be used in any way that is defamatory, violates the rights of third parties (including such third parties' rights of copyright, privacy, publicity, or other tangible or intangible property), or is otherwise illegal, sexually explicit or obscene. In addition, User may not conjoin a Work with any other material that may result in damage to the reputation of the Rightsholder. User agrees to inform CCC if it becomes aware of any infringement of any rights in a Work and to cooperate with any reasonable request of CCC or the Rightsholder in connection therewith.

4. Indemnity. User hereby indemnifies and agrees to defend the Rightsholder and CCC, and their respective employees and directors, against all claims, liability, damages, costs and expenses, including legal fees and expenses, arising out of any use of a Work beyond the scope of the rights granted herein, or any use of a Work which has been altered in any unauthorized way by User, including claims of defamation or infringement of rights of copyright, publicity, privacy or other tangible or intangible property.

5. Limitation of Liability. UNDER NO CIRCUMSTANCES WILL CCC OR THE RIGHTSHOLDER BE LIABLE FOR ANY DIRECT, INDIRECT, CONSEQUENTIAL OR INCIDENTAL DAMAGES (INCLUDING WITHOUT LIMITATION DAMAGES FOR LOSS OF BUSINESS PROFITS OR INFORMATION, OR FOR BUSINESS INTERRUPTION) ARISING OUT OF THE USE OR INABILITY TO USE A WORK, EVEN IF ONE OF THEM HAS BEEN ADVISED OF THE POSSIBILITY OF SUCH DAMAGES. In any event, the total liability of the Rightsholder and CCC (including their respective employees and directors) shall not exceed the total amount actually paid by User for this license. User assumes full liability for the actions and omissions of its principals, employees, agents, affiliates, successors and assigns.

6. Limited Warranties. THE WORK(S) AND RIGHT(S) ARE PROVIDED “AS IS”. CCC HAS THE RIGHT TO GRANT TO USER THE RIGHTS GRANTED IN THE ORDER CONFIRMATION DOCUMENT. CCC AND THE RIGHTSHOLDER DISCLAIM ALL OTHER WARRANTIES RELATING TO THE WORK(S) AND RIGHT(S), EITHER EXPRESS OR IMPLIED, INCLUDING WITHOUT LIMITATION IMPLIED WARRANTIES OF MERCHANTABILITY OR FITNESS FOR A PARTICULAR PURPOSE. ADDITIONAL RIGHTS MAY BE REQUIRED TO USE ILLUSTRATIONS, GRAPHS, PHOTOGRAPHS, ABSTRACTS, INSERTS OR OTHER PORTIONS OF THE WORK (AS OPPOSED TO THE ENTIRE WORK) IN A MANNER CONTEMPLATED BY USER; USER UNDERSTANDS AND AGREES THAT NEITHER CCC NOR THE RIGHTSHOLDER MAY HAVE SUCH ADDITIONAL RIGHTS TO GRANT.

7. Effect of Breach. Any failure by User to pay any amount when due, or any use by User of a Work beyond the scope of the license set forth in the Order Confirmation and/or these terms and conditions, shall be a material breach of the license created by the Order Confirmation and these terms and conditions. Any breach not cured within 30 days of written notice thereof shall result in immediate termination of such license without further notice. Any unauthorized (but licensable) use of a Work that is terminated immediately upon notice thereof may be liquidated by payment of the Rightsholder's ordinary license price therefor; any unauthorized (and unlicensable) use that is not terminated immediately for any reason (including, for example, because materials containing the Work cannot reasonably be recalled) will be subject to all remedies available at law or in equity, but in no event to a payment of less than three times the Rightsholder's ordinary license price for the most closely analogous licensable use plus Rightsholder's and/or CCC's costs and expenses incurred in collecting such payment.

8. **Miscellaneous.**

8.1 User acknowledges that CCC may, from time to time, make changes or additions to the Service or to these terms and conditions, and CCC reserves the right to send notice to the User by electronic mail or otherwise for the purposes of notifying User of such changes or additions; provided that any such changes or additions shall not apply to permissions already secured and paid for.

8.2 Use of User-related information collected through the Service is governed by CCC’s privacy policy, available online here: http://www.copyright.com/content/cc3/en/tools/footer/privacypolicy.html.

8.3 The licensing transaction described in the Order Confirmation is personal to User. Therefore, User may not assign or transfer to any other person (whether a natural person or an organization of any kind) the license created by the Order Confirmation and these terms and conditions or any rights granted hereunder; provided, however, that User may assign such license in its entirety on written notice to CCC in the event of a transfer of all or substantially all of User’s rights in the new material which includes the Work(s) licensed under this Service.

8.4 No amendment or waiver of any terms is binding unless set forth in writing and signed by the parties. The Rightsholder and CCC hereby object to any terms contained in any writing prepared by the User or its principals, employees, agents or affiliates and purporting to govern or otherwise relate to the licensing transaction described in the Order Confirmation, which terms are in any way inconsistent with any terms set forth in the Order Confirmation and/or in these terms and conditions or CCC's standard operating procedures, whether such writing is prepared prior to, simultaneously with or subsequent to the Order Confirmation, and whether such writing appears on a copy of the Order Confirmation or in a separate instrument.

8.5 The licensing transaction described in the Order Confirmation document shall be governed by and construed under the law of the State of New York, USA, without regard to the principles thereof of conflicts of law. Any case, controversy, suit, action, or proceeding arising out of, in connection with, or related to such licensing transaction shall be brought, at CCC's sole discretion, in any federal or state court located in the County of New York, State of New York, USA, or in any federal or state court whose geographical jurisdiction covers the location of the Rightsholder set forth in the Order Confirmation. The parties expressly submit to the personal jurisdiction and venue of each such federal or state court.If you have any comments or questions about the Service or Copyright Clearance Center, please contact us at 978-750-8400 or send an e-mail to info@copyright.com.

v 1.1

Close

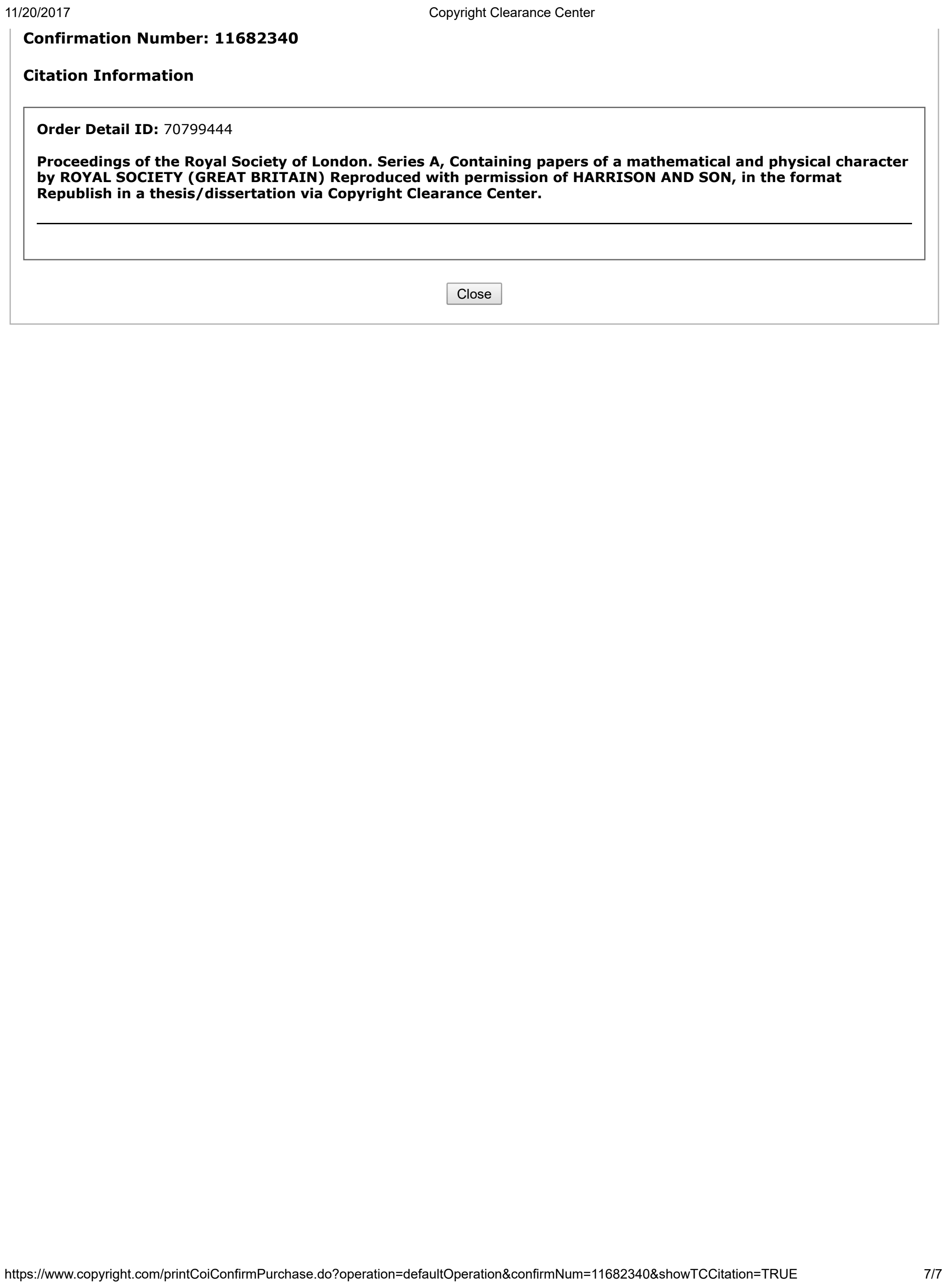

11/20/2017 Copyright Clearance Center

Confirmation Number: 11682340

Citation Information

Order Detail ID: 70799444

Proceedings of the Royal Society of London. Series A, Containing papers of a mathematical and physical character by ROYAL SOCIETY (GREAT BRITAIN) Reproduced with permission of HARRISON AND SON, in the format Republish in a thesis/dissertation via Copyright Clearance Center.

https://www.copyright.com/printCoiConfirmPurchase.do?operation=defaultOperation&confirmNum=11682340&showTCCitation=TRUE 7/7

NATURE PUBLISHING GROUP LICENSE TERMS AND CONDITIONS

Nov 20, 2017

This Agreement between Shawn Culbreth ("You") and Nature Publishing Group ("Nature Publishing Group") consists of your license details and the terms and conditions provided by Nature Publishing Group and Copyright Clearance Center.

License Number	4233170404828
License date	Nov 20, 2017
Licensed Content Publisher	Nature Publishing Group
Licensed Content Publication	Nature
Licensed Content Title	Near-infrared flares from accreting gas around the supermassive black hole at the Galactic Centre
Licensed Content Author	R. Genzel, R. Schödel, T. Ott, A. Eckart, T. Alexander et al.
Licensed Content Date	Oct 30, 2003
Licensed Content Volume	425
Licensed Content Issue	6961
Type of Use	reuse in a dissertation / thesis
Requestor type	academic/educational
Format	print and electronic
Portion	figures/tables/illustrations
Number of figures/tables/illustrations	1
High-res required	no
Figures	Figure 2: Light curves of the SgrA* infrared flares and quiescent emission in 2002–03.
Author of this NPG article	no
Your reference number	
Title of your thesis / dissertation	A solution method determining the effect of spin upon gravitational effects in the surroundings of a black hole.
Expected completion date	Dec 2017
Estimated size (number of pages)	120
Requestor Location	Shawn Culbreth 114 N. Harding St GREENVILLE, NC 27858 United States Attn: Shawn Culbreth
Billing Type	Invoice
Billing Address	Shawn Culbreth 114 N. Harding St GREENVILLE, NC 27858

United States
Attn: Shawn Culbreth

Total	0.00 USD

Terms and Conditions

Terms and Conditions for Permissions

Nature Publishing Group hereby grants you a non-exclusive license to reproduce this material for this purpose, and for no other use,subject to the conditions below:

1. NPG warrants that it has, to the best of its knowledge, the rights to license reuse of this material. However, you should ensure that the material you are requesting is original to Nature Publishing Group and does not carry the copyright of another entity (as credited in the published version). If the credit line on any part of the material you have requested indicates that it was reprinted or adapted by NPG with permission from another source, then you should also seek permission from that source to reuse the material.

2. Permission granted free of charge for material in print is also usually granted for any electronic version of that work, provided that the material is incidental to the work as a whole and that the electronic version is essentially equivalent to, or substitutes for, the print version.Where print permission has been granted for a fee, separate permission must be obtained for any additional, electronic re-use (unless, as in the case of a full paper, this has already been accounted for during your initial request in the calculation of a print run).NB: In all cases, web-based use of full-text articles must be authorized separately through the 'Use on a Web Site' option when requesting permission.

3. Permission granted for a first edition does not apply to second and subsequent editions and for editions in other languages (except for signatories to the STM Permissions Guidelines, or where the first edition permission was granted for free).

4. Nature Publishing Group's permission must be acknowledged next to the figure, table or abstract in print. In electronic form, this acknowledgement must be visible at the same time as the figure/table/abstract, and must be hyperlinked to the journal's homepage.

5. The credit line should read:
   Reprinted by permission from Macmillan Publishers Ltd: [JOURNAL NAME] (reference citation), copyright (year of publication)
   For AOP papers, the credit line should read:
   Reprinted by permission from Macmillan Publishers Ltd: [JOURNAL NAME], advance online publication, day month year (doi: 10.1038/sj.[JOURNAL ACRONYM].XXXXX)

   Note: For republication from the *British Journal of Cancer,* the following credit lines apply.
   Reprinted by permission from Macmillan Publishers Ltd on behalf of Cancer Research UK: [JOURNAL NAME] (reference citation), copyright (year of publication)For AOP papers, the credit line should read:
   Reprinted by permission from Macmillan Publishers Ltd on behalf of Cancer Research UK: [JOURNAL NAME], advance online publication, day month year (doi: 10.1038/sj.[JOURNAL ACRONYM].XXXXX)

6. Adaptations of single figures do not require NPG approval. However, the adaptation should be credited as follows:

   Adapted by permission from Macmillan Publishers Ltd: [JOURNAL NAME] (reference citation), copyright (year of publication)

   Note: For adaptation from the *British Journal of Cancer,* the following credit line applies.
   Adapted by permission from Macmillan Publishers Ltd on behalf of Cancer Research UK: [JOURNAL NAME] (reference citation), copyright (year of publication)

7. Translations of 401 words up to a whole article require NPG approval. Please visit http://www.macmillanmedicalcommunications.com for more information.Translations of up

to a 400 words do not require NPG approval. The translation should be credited as follows:

Translated by permission from Macmillan Publishers Ltd: [JOURNAL NAME] (reference citation), copyright (year of publication).

Note: For translation from the *British Journal of Cancer,* the following credit line applies.
Translated by permission from Macmillan Publishers Ltd on behalf of Cancer Research UK: [JOURNAL NAME] (reference citation), copyright (year of publication)

We are certain that all parties will benefit from this agreement and wish you the best in the use of this material. Thank you.
Special Terms:
v1.1

Questions? customercare@copyright.com or +1-855-239-3415 (toll free in the US) or +1-978-646-2777.

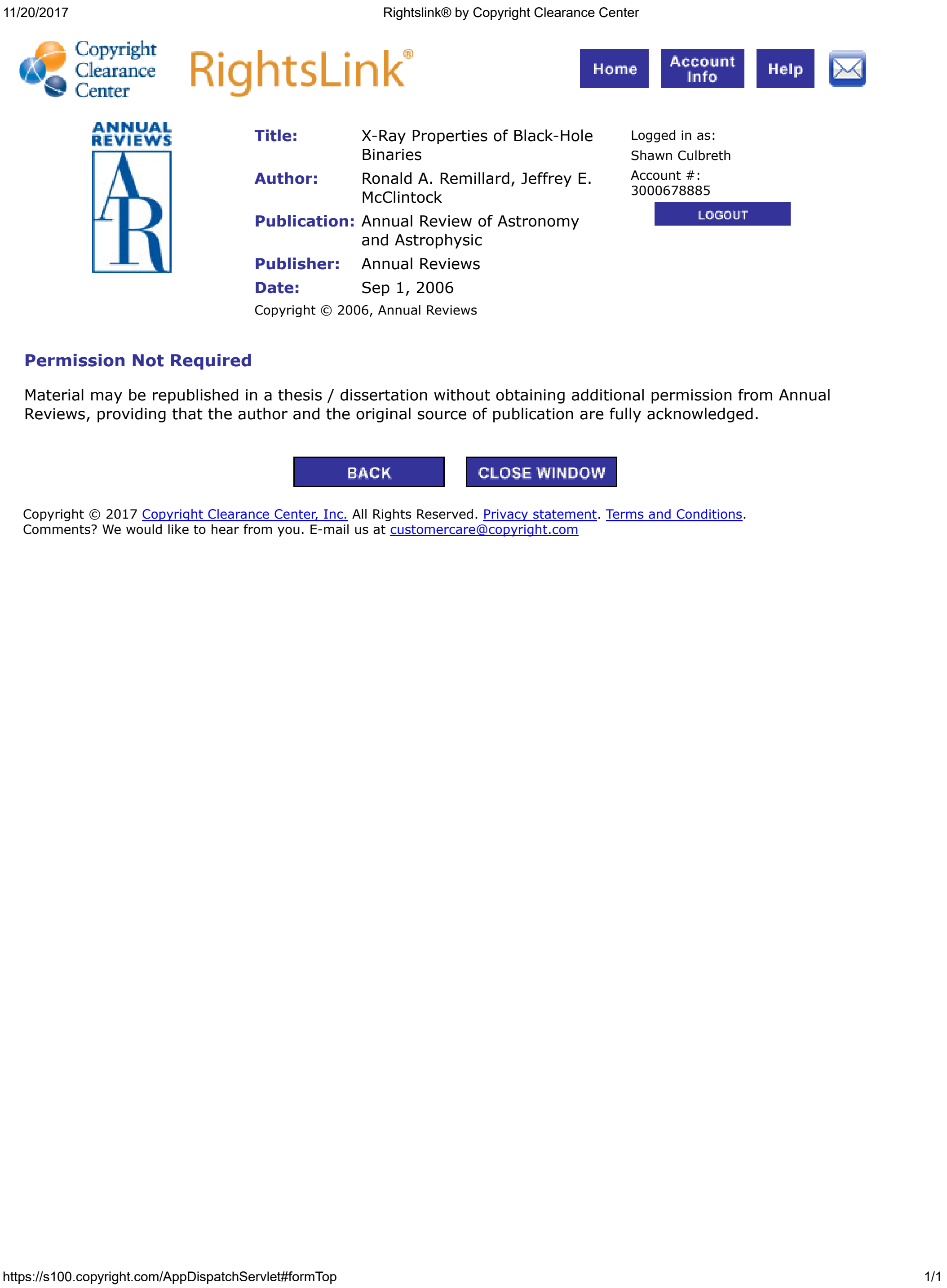

11/20/2017 Rightslink® by Copyright Clearance Center

Title:	X-Ray Properties of Black-Hole Binaries
Author:	Ronald A. Remillard, Jeffrey E. McClintock
Publication:	Annual Review of Astronomy and Astrophysic
Publisher:	Annual Reviews
Date:	Sep 1, 2006

Copyright © 2006, Annual Reviews

Logged in as:
Shawn Culbreth
Account #:
3000678885

Permission Not Required

Material may be republished in a thesis / dissertation without obtaining additional permission from Annual Reviews, providing that the author and the original source of publication are fully acknowledged.

https://s100.copyright.com/AppDispatchServlet#formTop 1/1